

# NAVAL POSTGRADUATE SCHOOL

## Monterey, California



## Dissertation

**APPLICATION OF HIGDON NON-REFLECTING  
BOUNDARY CONDITIONS TO  
SHALLOW WATER MODELS**

by

Vincent J. van Joolen

June 2003

Dissertation Supervisors:

Beny Neta  
Dan Givoli

**Approved for public release; distribution is unlimited**

THIS PAGE INTENTIONALLY LEFT BLANK

REPORT DOCUMENTATION PAGE			Form Approved OMB No. 0704-0188	
<p>Public reporting burden for this collection of information is estimated to average 1 hour per response, including the time for reviewing instructions, searching existing data sources, gathering and maintaining the data needed, and completing and reviewing the collection of information. Send comments regarding this burden estimate or any other aspect of this collection of information, including suggestions for reducing this burden, to Washington Headquarters Services, Directorate for Information Operations and Reports, 1215 Jefferson Davis Highway, Suite 1204, Arlington, Va. 22202-4302, and to the Office of Management and Budget, Paperwork Reduction Project (0704-0188) Washington DC 20503.</p>				
1. AGENCY USE ONLY (Leave blank)		2. REPORT DATE June 2003	3. REPORT TYPE AND DATES COVERED Dissertation	
4. TITLE AND SUBTITLE Application of Higdon Non-reflecting Boundary Conditions to Shallow Water Models			5. FUNDING NUMBERS	
6. AUTHORS van Joolen, Vincentius J				
7. PERFORMING ORGANIZATION NAME(S) AND ADDRESS(ES) Naval Postgraduate School Monterey CA 93943-5000			8. PERFORMING ORGANIZATION REPORT NUMBER	
9. SPONSORING/MONITORING AGENCY NAME(S) AND ADDRESS(ES)			10. SPONSORING/MONITORING AGENCY REPORT NUMBER	
11. SUPPLEMENTARY NOTES The views expressed in this thesis are those of the author and do not reflect the official policy or position of the Department of Defense or the U.S. Government.				
12a. DISTRIBUTION/AVAILABILITY STATEMENT Approved for public release; distribution is unlimited.			12b. DISTRIBUTION CODE	
<p>13. ABSTRACT(maximum 200 words)</p> <p>In many applications involving wave propagation, problem domains are often very large or unbounded. A common numerical method used to solve such problems is to truncate the domain via artificial boundaries to form a finite computational domain. To accomplish this, Non-Reflecting Boundary Conditions (NRBC's) which minimize spurious wave reflections are imposed. The quality of the solution strongly depends on the properties of both the NRBC and the wave behavior.</p> <p>This dissertation explores the use of Higdon NRBC's to solve shallow water equations (SWE's) in a dispersive environment. A linearized SWE model is developed that includes stratification and advection effects. Initially a single NRBC is used to truncate a semi-infinite channel. Later four NRBC's are used to restrict an infinite plane. In both cases finite rectangular domains are formed. A scheme developed by Neta and Givoli is used to rapidly discretize high-order Higdon NRBC's. Finite difference methods and are used in all numerical schemes, which are solved explicitly when possible. Results will show that Higdon NRBC's can be used effectively to restrict large rectangular domains when solving SWE's that include the before mentioned effects.</p>				
14. SUBJECT TERMS Waves, High-order, Artificial Boundary, Non-Reflecting Boundary Condition, Higdon, Finite Difference, Shallow Water Equation, Stratification.			15. NUMBER OF PAGES 156	
			16. PRICE CODE	
17. SECURITY CLASSIFICATION OF REPORT Unclassified	18. SECURITY CLASSIFICATION OF THIS PAGE Unclassified	19. SECURITY CLASSIFICATION OF ABSTRACT Unclassified	20. LIMITATION OF ABSTRACT UL	

THIS PAGE INTENTIONALLY LEFT BLANK

**Approved for public release; distribution is unlimited**

**APPLICATION OF HIGDON NON-REFLECTING BOUNDARY  
CONDITIONS TO SHALLOW WATER MODELS**

Vincent J. van Joolen

Commander, United States Navy

B.S. Chemical Engineering, University of California, San Diego, 1983

M.S. Applied Mathematics, Naval Postgraduate School, Monterey, CA, 1991

M.S. Strategic Thought, Army War College, Carlisle, PA, 2000

Submitted in partial fulfillment of the  
requirements for the degree of

**DOCTOR OF PHILOSOPHY IN APPLIED MATHEMATICS**

from the

**NAVAL POSTGRADUATE SCHOOL**

**June 2003**

Author:

Vincent J. van Joolen

Approved by:

Beny Neta

Professor of Appl. Math.

Dissertation Supervisor

Dan Givoli

Professor of Aerospace Eng.

Dissertation Supervisor

Arthur Schoenstadt

Professor of Appl. Math.

Clyde Scandrett

Professor of Appl. Math.

Robert Haney

Professor of Meteorology

Approved by:

Clyde Scandrett, Chair, Department of Applied Mathematics

Approved by:

Carson K. Eoyang, Associate Provost for Academic Affairs

THIS PAGE INTENTIONALLY LEFT BLANK

# ABSTRACT

In many applications involving wave propagation, problem domains are often very large or unbounded. A common numerical method used to solve such problems is to truncate the domain via artificial boundaries to form a finite computational domain. To accomplish this, Non-Reflecting Boundary Conditions (NRBC's) which minimize spurious wave reflections are imposed. The quality of the solution strongly depends on the properties of both the NRBC and the wave behavior.

This dissertation explores the use of Higdon NRBC's to solve shallow water equations (SWE's) in a dispersive environment. A linearized SWE model is developed that includes stratification and advection effects. Initially a single NRBC is used to truncate a semi-infinite channel. Later four NRBC's are used to restrict an infinite plane. In both cases finite rectangular domains are formed. A scheme developed by Neta and Givoli is used to rapidly discretize high-order Higdon NRBC's. Finite difference methods are used in all numerical schemes, which are solved explicitly when possible. Results will show that Higdon NRBC's can be used effectively to restrict large rectangular domains when solving SWE's that include the before mentioned effects.

THIS PAGE INTENTIONALLY LEFT BLANK



# TABLE OF CONTENTS

I.	INTRODUCTION . . . . .	1
II.	MODELING GEOPHYSICAL FLUID FLOW . . . . .	3
A.	CONSERVATION OF MASS EQUATIONS FOR FLUIDS IN A CONTROL VOLUME . . . . .	4
B.	THE MOMENTUM EQUATIONS FOR FLUIDS IN A CON- TROL VOLUME . . . . .	5
1.	Acceleration Components for a Fluid in a Cartesian In- ertial Frame . . . . .	5
2.	Acceleration Components in a Two-Dimension Cartesian Rotating Frame . . . . .	6
3.	Acceleration Components in the Earth Model . . . . .	10
4.	Forces Acting on a Fluid Control Volume . . . . .	14
5.	The Momentum Equation for Geophysical Fluid Flow . . . . .	17
6.	Governing Equations for the Shallow Water Model . . . . .	18
7.	Linearizing the Shallow Water Model . . . . .	21
8.	Deriving the Klein-Gordon Equation . . . . .	25
9.	Analytic Considerations of the Klein-Gordon Equation . . . . .	26
III.	HIGDON NON-REFLECTING BOUNDARY CONDITIONS . . . . .	29
A.	THE SEMI-INFINITE WAVE GUIDE PROBLEM . . . . .	29
B.	THE HIGDON NON-REFLECTING BOUNDARY CONDITION . . . . .	31
C.	DETERMINING OPTIMAL VALUES FOR THE HIGDON PARAMETERS . . . . .	34
1.	Experiment One: $C_j = C_0$ . . . . .	36

2.	Experiment Two: $C_j$ Determined from Wave Numbers Distributed Evenly over $[k_{min}, k_{max}]$ . . . . .	38
3.	Experiment Three: Estimating $C_j$ 's from Wave Numbers Obtained using the Minimax Formula . . . . .	39
4.	Experiment Four: A Procedure for Optimizing $C_j$ 's . . .	41
<b>IV.</b>	<b>DISCRETIZING THE SEMI-INFINITE WAVE GUIDE PROBLEM WITH ARTIFICIAL BOUNDARIES . . . . .</b>	<b>47</b>
A.	DISCRETIZING THE KLEIN-GORDON EQUATION . . . . .	47
B.	DISCRETIZING THE NORTH AND SOUTH BOUNDARIES . . . . .	48
C.	THE DISCRETE FORM OF THE HIGDON NRBC . . . . .	49
D.	IMPROVED FORM FOR THE DISCRETE HIGDON NRBC .	53
E.	NUMERICAL EXAMPLE: EMPLOYING HIGDON NRBC'S FOR A SINGLE WAVE PULSE AT $\Gamma_w$ IN A SEMI-INFINITE WAVE GUIDE . . . . .	55
F.	NUMERICAL EXAMPLE: SEMI-INFINITE WAVE GUIDE WITH A CONTINUOUS WAVE INTRODUCED AT $\Gamma_w$ . . . . .	62
<b>V.</b>	<b>A N-LAYER STRATIFIED DISPERSIVE WAVE MODEL . .</b>	<b>67</b>
A.	REDUCING THE STRATIFIED $N$ -LAYER MODEL TO THE KLEIN-GORDON FORM . . . . .	70
B.	DISCRETIZING THE KLEIN-GORDON FORM OF THE STRAT- IFIED $N$ -LAYER MODEL . . . . .	72
C.	NUMERICAL EXAMPLE: THE STRATIFIED $N$ -LAYER MODEL	73
D.	ADDITIONAL OBSERVATIONS FOR THE STRATIFIED $N$ -LAYER MODEL . . . . .	78
<b>VI.</b>	<b>APPLYING HIGDON NRBC'S TO TWO OR MORE SIDES OF A TWO-DIMENSIONAL RECTANGULAR DOMAIN . . . .</b>	<b>83</b>

A.	EXAMPLE ONE: A TWO-DIMENSIONAL SINGLE-LAYER SCHEME WITH HIGDON NRBC'S ON TWO SIDES . . . . .	83
B.	INSTABILITIES IN THE 2-D, 2-SIDED HIGDON NRBC SCHEME	89
C.	EXAMPLE TWO: A TWO-DIMENSIONAL MULTI-LAYER STRATIFIED SCHEME WITH HIGDON NRBC'S ON TWO SIDES . . . . .	92
D.	EXAMPLE FOUR: A TWO-DIMENSIONAL MULTI-LAYER STRATIFIED SCHEME WITH HIGDON NRBC'S ON FOUR SIDES . . . . .	95
VII.	<b>LINEARIZED SHALLOW WATER EQUATIONS WITH NON- ZERO ADVECTION . . . . .</b>	<b>99</b>
A.	DISCRETIZING THE LINEARIZED SWE WITH CONSTANT NON-ZERO ADVECTION TERMS . . . . .	101
B.	NUMERICAL EXAMPLE: TWO-DIMENSIONAL SINGLE-LAYER SCHEME WITH HIGDON NRBC'S ON FOUR SIDES WITH NON-ZERO ADVECTION . . . . .	103
C.	LINEARIZED SWE WITH CONSTANT NON-ZERO ADVEC- TION TERMS EXTENDED TO THE $N$ -LAYER MODEL . . .	113
D.	DISCRETIZING THE LINEARIZED SWE $N$ -LAYER STRAT- IFIED MODEL WITH CONSTANT NON-ZERO ADVECTION TERMS . . . . .	115
E.	NUMERICAL EXAMPLE: A TWO-LAYER SCHEME INCOR- PORATING ADVECTION . . . . .	117
F.	VARYING PARAMETERS FOR THE TWO-LAYER SCHEME WITH ADVECTION . . . . .	120
1.	Varying $C_j$ 's, $\Delta x$ , and $\Delta y$ . . . . .	121
2.	Varying $U$ and $V$ . . . . .	122
3.	Varying Layer Thicknesses in a 2-Layer Problem . . . . .	124

4.	Varying Density Distribution in a 2-Layer Problem . . .	125
5.	Varying $\Delta t$ in a 2-Layer Problem . . . . .	126
G.	THE "HIGDON MATRIX" . . . . .	127
VIII. CONCLUSION AND RECOMMENDATIONS FOR FURTHER		
	RESEARCH . . . . .	129
LIST OF REFERENCES . . . . .		131
INITIAL DISTRIBUTION LIST . . . . .		135

# LIST OF FIGURES

1.	Cartesian Two-Dimensional Rotating Frame . . . . .	7
2.	The Earth Model . . . . .	11
3.	Pressure Effects on a Rectangular Fluid Volume . . . . .	15
4.	$x$ -Components of Viscous Stress Tensor on a Rectangular Fluid Volume	16
5.	The Shallow Water Model . . . . .	19
6.	Flow Along the Bottom Contour in the $x$ -Direction . . . . .	20
7.	Shallow Water Model Cross Section with $h = H + h_B$ . . . . .	22
8.	Shallow Water Model Cross Section with $h = H_0 + \eta + h_B$ . . . . .	23
9.	Semi-Infinite Wave Guide . . . . .	29
10.	Left: Experiment 1a, $\eta_R$ at $t=100$ : $C_j = C_0$ with $C_0=2$ and $f=1$ (Solid Line Depicts $H_1$ . Dotted Line Depicts $H_2$ Plot). Right: $\ \eta_R\ $ at $t=100$ for $H_1$ through $H_9$ . . . . .	37
11.	$\ \eta_R\ $ at $t=100$ : $C_j = \frac{\sqrt{C_0^2 k_{min}^2 + f^2}}{k_{min}} = \sqrt{5}$ ( $C_0=2, f=1$ ) . . . . .	38
12.	Experiment 2, $\ \eta_R\ $ at $t=100$ : $C_j$ from $k$ Evenly Distributed on $[k_{min}, k_{max}]$ ( $C_0=2, f=1$ ) . . . . .	40
13.	Left: Experiment 3a, $\ \eta_R\ $ at $t=100$ and $C_j = C_0$ . Right: Experiment 3b, $\ \eta_R\ $ at $t=100$ and $C_j = \frac{\sqrt{C_0^2 k_{min}^2 + f^2}}{k_{min}}$ . In both Cases, $C_j$ is Computed from Wave Numbers Determined using the Minimax Formula Based on the Chebyshev Polynomial . . . . .	42
14.	Experiment 4, $\ \eta_R\ $ at $t=100$ : $C_j$ Optimized using Oscilloscope Procedure	45
15.	HNRBC-2DR-1S-1L-U0-V0-T01 with Simple Pulse Boundary Condition	57
16.	HNRBC-2DR-1S-1L-U0-V0-T04 with Simple Pulse Boundary Condition	58
17.	HNRBC-2DR-1S-1L-U0-V0-T05 with Simple Pulse Boundary Condition	59
18.	HNRBC-2DR-1S-1L-U0-V0-T08 with Simple Pulse Boundary Condition	60
19.	HNRBC-2DR-1S-1L-U0-V0-T10 with Simple Pulse Boundary Condition	60

20.	$\ e(t)\ _n$ Plots for 2-Point vs. 3-Point Higdon NRBC Approximations . .	61
21.	$\ e(t)\ _n$ Plots for $C_j = \{C_0, C_0, C_0, C_0\}$ vs. $C_j$ Selected using a the Symmetric Minimax Formula with 3-Point Higdon NRBC Approximations	61
22.	HNRBC-2DR-1S-1L-U0-V0-T10 with Continuous Wave Boundary Con- dition . . . . .	63
23.	$\ e(t)\ _n$ for $C_j = \{1, 1, 1, 1, 1\}$ vs. $C_j$ Auto-Selected Using Minimax Formula Based on Chebyshev Polynomials. . . . .	64
24.	$\ e(t)\ _n$ for $C_j = \{1, 1, 1, 1, 1\}$ vs. $C_j$ Distributed Evenly from $C_0$ to $\sqrt{C_0^2 + f^2}$ . . . . .	65
25.	$\ e(t)\ _n$ for $C_j = \{1, 1, 1, 1, 1\}$ vs. $C_j$ Distributed Evenly from $C_0$ to $k_{max} = \frac{\pi}{5\Delta x}$ . . . . .	65
26.	$\ e(t)\ _n$ for $C_j = \{1, 1, 1, 1, 1\}$ Using a Two-Point HNRBC Approxima- tion vs. $C_j = \{1, 1, 1, 1\}$ Using a Three-Point Higdon Approximation .	66
27.	$N$ -Layer Shallow Water Model . . . . .	68
28.	HNRBC-2DR-1S-6L-U0-V0-T07 . . . . .	76
29.	HNRBC-2DR-1S-6L-U0-V0-T15 . . . . .	77
30.	HNRBC-2DR-1S-6L-U0-V0-T07 Layer Perturbation Comparison . . . .	78
31.	HNRBC-2DR-1S-6L-U0-V0-T15 Layer Perturbation Comparison . . . .	79
32.	HNRBC-2DR-1S-6L-U0-V0-T07 Layer Interface Perturbation Comparison	80
33.	HNRBC-2DR-1S-6L-U0-V0-T15 Layer Interface Perturbation Comparison	81
34.	Model Comparison: HNRBC-2DR-1S-6L-U0-V0-T15 vs. HNRBC-2DR- 1S-2L-U0-V0-T15 vs. HNRBC-2DR-1S-1L-U0-V0-T15 . . . . .	82
35.	The Semi-Infinite Quarter-Plane . . . . .	83
36.	HNRBC-2DR-2S-1L-U0-V0-T03: Wave Pulse Passes through $\Gamma_N$ . . . .	85
37.	HNRBC-2DR-2S-1L-U0-V0-T05: Wave Pulse Passes through $\Gamma_E$ . . . .	86
38.	HNRBC-2DR-2S-1L-U0-V0-T15: Wave Pulse Passes through Corner .	87
39.	Corner Point Check: Two Approaches to Evaluating HNRBC Grid Points	88
40.	HNRBC-2DR-2S-1L-U0-V0-T03: $\Gamma_N$ Instability with $C_j = \{1, 1, 1, 1, 1\}$	89

41.	HNRBC-2DR-2S-1L-U0-V0-T10: $\Gamma_N$ Instability with $C_j = \{1, 1, 1, 1, 1\}$	90
42.	HNRBC-2DR-2S-1L-U0-V0-T10: Mitigation of Instability using Sommerfeld Condition ( $J = 1$ and $C_j = \{1\}$ ) . . . . .	91
43.	HNRBC-2DR-2S-6L-U0-V0-T06 with $J = 5$ and $C_j = \{1, 1, 1, 1, 1\}$ for each Layer . . . . .	93
44.	HNRBC-2DR-2S-6L-U0-V0-T15 with $J = 5$ and $C_j = \{1, 1, 1, 1, 1\}$ for each Layer . . . . .	94
45.	HNRBC-2DR-4S-6L-U0-V0-T01: Surface Disturbance Initiated. . . . .	96
46.	HNRBC-2DR-4S-6L-U0-V0-T06: Surface Disturbance has Left $\Omega$ . Bottom Disturbance Initiated. . . . .	97
47.	HNRBC-2DR-4S-6L-U0-V0-T13: All Events have Passed through HNRBC's. . . . .	98
48.	HNRBC-2DR-4S-6L-U0-V0-T15: Spurious Reflection Predominates in $\Omega$ . . . . .	98
49.	Plot A: $J = 5$ with $C_j = \{1, 1, 1, 1, 1\}$ adjusted for advection compared to $J = 5$ with $C_j = \{1, 1, 1, 1, 1\}$ unadjusted for advection. Plot B: $J = 3$ with $C_j = \{1, 1, 1\}$ compared to $J = 5$ with $C_j = \{1, 1, 1, 1, 1\}$ , both cases adjusted for advection. Plot C: $J = 3$ with $C_j = \{.8, .9, 1\}$ compared to $J = 3$ with $C_j = \{1, 1, 1\}$ , both cases adjusted for advection. Plot D: Corner check for $J = 3$ with $C_j = \{.8, .9, 1\}$ adjusted for advection . . . . .	105
50.	HNRBC-2DR-4S-1L-U.5-Vm.25-T01: Event 1 Initiated. . . . .	107
51.	HNRBC-2DR-4S-1L-U.5-Vm.25-T02: Event 1 Crosses $\Gamma_S$ and $\Gamma_E$ . . . . .	108
52.	HNRBC-2DR-4S-1L-U.5-Vm.25-T03: Event 1 Crosses $\Gamma_N$ and $\Gamma_W$ . . . . .	109
53.	HNRBC-2DR-4S-1L-U.5-Vm.25-T05: Event 1 Leaves $\Omega$ with Visible Spurious Reflection at $\Gamma_W$ . . . . .	110
54.	HNRBC-2DR-4S-1L-U.5-Vm.25-T06: Event 2 Initiated. . . . .	110
55.	HNRBC-2DR-4S-1L-U.5-Vm.25-T10: The Noise of Spurious Reflection Evident at the Bottom Left Plot. . . . .	111

56.	HNRBC-2DR-4S-1L-U.4-Vm.15-T10: End of Run . . . . .	111
57.	HNRBC-2D-4S-1L-U.6-Vm.35-T10: End of Run . . . . .	112
58.	HNRBC-2DR-4S-2L-Up025-Vmp025-T01: Disturbance Initiated. . . . .	118
59.	HNRBC-2DR-4S-2L-Up025-Vmp025-T05: End of Run, Some Noise at Boundaries of Bottom Left Plot. . . . .	119
60.	Higdon Matrix Image for $\Omega$ ( $20 \times 20$ ) with Higdon NRBC's with Order $J = 9$ Applied to Four Sides . . . . .	127



# LIST OF TABLES

I.	Variables Used to Derive Rotational Components of Momentum Equation	7
II.	$H_2$ Values for $A_{m_{(3)}}$ and $P_{m_{(3)}}$ . . . . .	51
III.	Constructing $P_m$ and $A_m$ from the Base Three Index 0221 <sub>(3)</sub> . . . . .	52
IV.	Varying $C_j$ -s with $\Delta x = \Delta y = .5$ . . . . .	121
V.	Varying $C_j$ -s with $\Delta x = \Delta y = .25$ . . . . .	122
VI.	Varying $U$ and $V$ with $\Delta x = \Delta y = .5$ ( $U, V$ Equal in each Layer) . . .	123
VII.	Varying $U$ and $V$ with $\Delta x = \Delta y = .25$ ( $U, V$ Equal in each Layer) . . .	123
VIII.	Varying $U$ and $V$ with $\Delta x = \Delta y = .25$ for Event Initiated in $L_1$ ( $U, V$ not Necessarily Equal in each Layer) . . . . .	124
IX.	Varying $U$ and $V$ with $\Delta x = \Delta y = .25$ for Event Initiated in $L_2$ ( $U, V$ not Necessarily Equal in each Layer) . . . . .	124
X.	Varying Layer Thickness in a 2-Layer Problem with an $L_1$ Initiated Event (left) and $L_2$ Initiated Event (right) . . . . .	125
XI.	Varying Layer Thickness in a 2-Layer Problem with a $L_1$ Initiated Event (left) and $L_2$ Initiated Event (right) . . . . .	126
XII.	Varying $\Delta t$ in a 2-Layer Problem with a $L_1$ Initiated Event . . . . .	126

THIS PAGE INTENTIONALLY LEFT BLANK

## ACKNOWLEDGMENTS

Thank you to all who made this dissertation possible. Dr. Beny Neta, my dissertation supervisor, from whom I “learned the ropes” with regards to publication, successfully producing several papers as a result of this research. As my “editor and chief” he patiently reviewed several iterations of work. His previous research with Dr. Dan Givoli, my dissertation co-supervisor, provided the necessary background for my investigations. Dr. Robert Haney provided a “real-world reality check” and ensured that my work was relevant to the oceanography and meteorology communities. Dr. Clyde Scandrett and Dr. Arthur Schoenstadt, the remaining members of my committee, guided me in courses that provided valuable insights in the pursuit of my research. Lieutenant Colonel Archie Wilmer, my “comrade in arms”, was my sounding board who patiently tolerated my many concerns and “off the wall” ideas. He also was a superb study partner both during our course work and in preparation for our doctoral examinations. Finally, to the United State Navy, for generously allowing me to take three years from my career to complete this program.

On the home front, I express my deepest gratitude to my wife Beverly, my son Skylar and my daughter Bronwyn, who exhibited infinite patience and understanding throughout the long hours that were required to complete my doctorate. Finally, I salute my father, Theodorus Johannes, who died in 1989. He brought the family to the United States from the Netherlands in 1961 primarily to ensure that his children would have access to higher education.

THIS PAGE INTENTIONALLY LEFT BLANK

# I. INTRODUCTION

Phenomena involving the propagation of waves in unbounded (or very large) domains are applicable to many fields including acoustics, electromagnetics, meteorology, and geophysics. However, it is infeasible to compute numerical solutions for regions of this scope. Therefore, it is necessary to define artificial boundaries that reduce the size of the domain. To accurately model the wave action in the truncated region, artificial boundary conditions must be imposed that allow waves propagating inside the region to pass freely without spurious reflections, which would pollute the computational domain. Such a boundary condition is known as the Non-Reflecting Boundary Condition (NRBC) and is the main subject of this dissertation.

In general, it is not possible to construct a boundary condition that will accomplish the criteria perfectly, but during the last 25 years research has been conducted to develop NRBC's that after discretization lead to stable, accurate, efficient and easily-implemented schemes [Ref. 1, 2, 3, 4]. Investigations in the late 70's to early 80's produced a number of low-order local NRBC's, e.g. the Engquist-Majda [Ref. 5] and Bayliss-Turkel [Ref. 6] boundary conditions. The exact non-local Dirichlet-to-Neumann (DtN) NRBC [Ref. 7, 8] and the Perfectly Matched Layer [Ref. 9] boundary conditions were developed in the late 80's and early 90's. Subsequently, higher order NRBC's were introduced, but were difficult to employ beyond the 2<sup>nd</sup> or 3<sup>rd</sup> order.

Only since the mid 90's have practical higher order schemes been developed. Collino [Ref. 10] proposed such a scheme for two-dimensional time-dependent wave in a rectangular domain. Grote and Keller [Ref. 11] extended the domain to three dimensions in a scheme based on spherical harmonic transformations. They extended their work to include elastic waves [Ref. 12]. These findings were independently published by Sofronov [Ref. 13] in Russian literature. Hagstrom and Hariharan [Ref. 14] constructed high-order NRBC's for two- and three-dimensional domains based on the analytic series representation for the outgoing solutions of these equations. Guddati

and Tassoulas [Ref. 15] devised a high-order NRBC scheme for time-dependent waves in a 2-dimensional wave guide using rational approximation and recursive continued fractions. Givoli [Ref. 16] derived high-order NRBC's for a general class of wave problems leading to a symmetric finite element formulation. These early investigations utilized either time-harmonic waves or non-dispersive time-dependent waves.

Wave dispersion, however, is an ever present phenomenon. In the late 80's and early 90's, Higdon developed NRBC's for non-dispersive waves [Ref. 17, 18, 19, 20], but later showed that his schemes could be applied to the dispersive (Klein-Gordon) wave equation [Ref. 21]. Higdon's work involves low order formulation of his scheme. Givoli and Neta [Ref. 22, 23, 24] present an algorithm for implementing the Higdon NRBC to any order using high-order FD discretization. They further developed methods to rewrite the Higdon NRBC without using high order derivatives and to generate Higdon parameters that maximize the non-reflection property of the NRBC in a dispersive wave environment.

In the present work I will develop high order Higdon NRBC schemes for use with linearized shallow water equations (SWE's) in Cartesian coordinates. The SWE model is further enhanced to include the effects of stratification and advection. A single Higdon NRBC is initially applied as an artificial boundary on one side of a semi-infinite channel. Later four Higdon NRBC's are applied to the sides of a rectangular domain to restrict an infinite plane. Finite-difference schemes are used to numerically solve the problems. Discrete forms of the Higdon NRBC, based on the work of Givoli and Neta, are then employed on the artificial boundary. The results of several numerical examples are reported to validate the SWE models as well as the use of the Higdon NRBC as an effective means of restricting a very large domain.

## II. MODELING GEOPHYSICAL FLUID FLOW

In this chapter we develop a model that describes large scale geophysical flow. Many of the details of this derivation are developed by Pedlosky [Ref. 25]. We start by considering the dynamics of a shallow rotating fluid layer. The fundamental condition that characterizes a shallow layer is:

$$\frac{D}{L} \ll 1,$$

where  $D$  and  $L$  characterize the scale of vertical and horizontal motions. This characterization is applicable to large scale atmospheric and oceanic flows where the vertical scale of the fluid layer is of the order of miles, while the horizontal scale is of the order of hundreds or thousands of miles. Work by Rossby [Ref. 30] and Stommel [Ref. 31] show that such a working geophysical model can be developed by assuming that the fluid is:

- Incompressible (density independent of pressure),
- Inviscid (no internal frictional forces),
- Homogeneous (not stratified with regards to density).

Later in this paper, the “homogenous” assumption is relaxed. The following physical laws are applied in deriving a geophysical model:

- Conservation of Mass,
- Conservation of Momentum (Newton’s 2<sup>nd</sup> Law),
- Conservation of Energy,
- Second Law of Thermodynamics.

Since the fluid is incompressible, the energy equations are uncoupled from the model. Hence, we consider only the conservation of mass and momentum. The basic form

of these laws apply to fixed quantities of matter. In the analysis of fluid flow, we are concerned with fixed volumes (e.g. the properties of a fluid within a control volume rather than properties of individual particles in motion). What follows is a derivation of the conservation of mass and momentum equations as they apply to control volumes.

## A. CONSERVATION OF MASS EQUATIONS FOR FLUIDS IN A CONTROL VOLUME

The conservation of mass law states that the total change of mass in a control volume must be equal to the net flow of mass entering and leaving at the volume surface. If  $\rho$  is the density of the fluid and  $\rho\vec{u} \cdot \vec{n}$  is the mass flux at a point on the volume surface, then by invoking the conservation of mass law we can write:

$$\frac{\partial}{\partial t} \int \rho dV = - \int (\rho\vec{u} \cdot \vec{n}) dA, \quad (\text{II.1})$$

where  $V$  is the volume and  $A$  is the volume surface area. By the divergence theorem we know that:

$$\int (\rho\vec{u} \cdot \vec{n}) dA = \int \nabla \cdot (\rho\vec{u}) dV. \quad (\text{II.2})$$

Applying this to (II.1) yields:

$$\int \left( \frac{\partial \rho}{\partial t} + \nabla \cdot (\rho\vec{u}) \right) dV = 0, \quad (\text{II.3})$$

which implies:

$$\frac{\partial \rho}{\partial t} + \nabla \cdot (\rho\vec{u}) = 0. \quad (\text{II.4})$$

Since the fluid is assumed to be incompressible and homogeneous (e.g.  $\rho$  is constant), this equation is rewritten as:

$$\nabla \cdot \vec{u} = 0, \quad (\text{II.5})$$

or, in three dimensional Cartesian coordinates:

$$\boxed{\frac{\partial u}{\partial x} + \frac{\partial v}{\partial y} + \frac{\partial w}{\partial z} = 0}, \quad (\text{II.6})$$



where  $u$ ,  $v$ , and  $w$  are the velocity components in the  $x$ -,  $y$ -, and  $z$ -directions respectively. This expression is called the continuity equation. It describes the conservation of mass for a volume element containing an incompressible fluid and is the first controlling equation of the geophysical fluid flow model.

## B. THE MOMENTUM EQUATIONS FOR FLUIDS IN A CONTROL VOLUME

The next set of controlling equations is the momentum equation and is based on Newton's Second Law:

$$Force = (mass)(acceleration).$$

Acceleration components must be carefully derived, because geophysical phenomena occur in a non-inertial rotating frame. In the following analysis, we first consider a derivation of these equations for a fluid in an inertial two-dimensional Cartesian system. A rotational component is then introduced to generate non-inertial momentum terms. A third dimension is added and acceleration components in vector form are obtained. Finally an Earth model is developed on which the geophysical fluid flow equations of momentum will be based.

### 1. Acceleration Components for a Fluid in a Cartesian Inertial Frame

We first consider acceleration in an inertial frame (e.g. one that is not accelerating or rotating). The acceleration component in the  $x$ -direction is:

$$a_x = \frac{du}{dt}, \tag{II.7}$$

where  $u$  is the velocity in the  $x$ -direction. Since we do not treat fluids as individual particles, but rather as a continuum of matter,  $u$  not only depends on time, but also on the spatial components  $x$ ,  $y$ , and  $z$ . Therefore:

$$du = \frac{\partial u}{\partial t} dt + \frac{\partial u}{\partial x} dx + \frac{\partial u}{\partial y} dy + \frac{\partial u}{\partial z} dz, \tag{II.8}$$

and (II.7) becomes:

$$a_x = \frac{du}{dt} = \frac{\partial u}{\partial t} + \frac{\partial u}{\partial x} \frac{dx}{dt} + \frac{\partial u}{\partial y} \frac{dy}{dt} + \frac{\partial u}{\partial z} \frac{dz}{dt}, \quad (\text{II.9})$$

which is rewritten as:

$$a_x = \frac{\partial u}{\partial t} + u \frac{\partial u}{\partial x} + v \frac{\partial u}{\partial y} + w \frac{\partial u}{\partial z}, \quad (\text{II.10})$$

where  $v$  and  $w$  are components of velocity in the  $y$ - and  $z$ -direction respectively. We now define the following special symbol:

$$\frac{D}{Dt} = \frac{\partial}{\partial t} + u \frac{\partial}{\partial x} + v \frac{\partial}{\partial y} + w \frac{\partial}{\partial z}, \quad (\text{II.11})$$

which is often called the *derivative following a fluid* [Ref. 27]. Using this symbol we write acceleration as:

$$a_x = \frac{Du}{Dt}. \quad (\text{II.12})$$

Similarly:

$$a_y = \frac{Dv}{Dt} \quad \text{and} \quad a_z = \frac{Dw}{Dt}, \quad (\text{II.13})$$

or in vector form:

$$\vec{a} = \frac{D\vec{u}}{Dt}. \quad (\text{II.14})$$

We now consider the effects of the rotation on the acceleration vector.

## 2. Acceleration Components in a Two-Dimension Cartesian Rotating Frame

Rotation is an important factor in dynamics if the time  $t_w$  to complete a single rotation is on the order of or less than the time  $t_L$  taken by an object/fluid field to cover a distance  $L$  at a speed  $U$  (e.g.  $\frac{t_w}{t_L} \leq 1$  where  $t_L = \frac{L}{U}$ ). For example, consider a large disc that completes one rotation every 5,000 seconds ( $t_w$ ). On this disc a particle travels 10 kilometers ( $L$ ) at a speed of 1 meters-second<sup>-1</sup> ( $U$ ), it will complete its journey 10<sup>4</sup> seconds ( $t_L$ ). Thus  $\frac{t_w}{t_L} = .5$  and we conclude that rotation will influence the momentum equations.

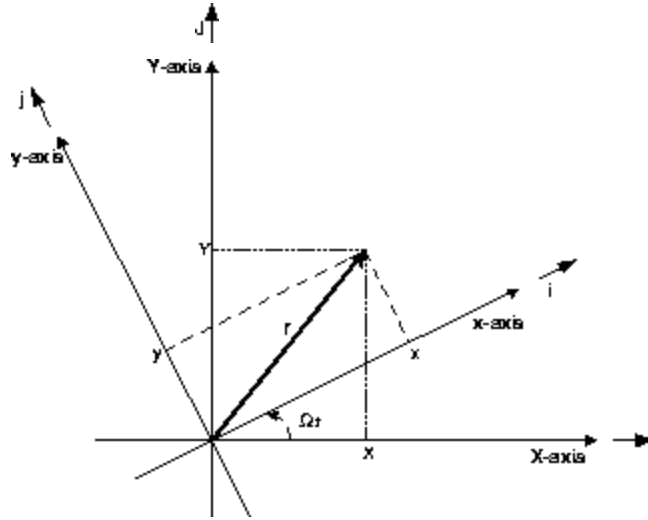


Figure 1. Cartesian Two-Dimensional Rotating Frame

In deriving the rotational acceleration terms for the simplified two-dimensional model, tracking variables is a challenging task. Figure 1, which superimposes a two-dimensional Cartesian rotational frame on an inertial frame at a common origin, introduces these variables. Additionally, Table I tabulates the variables with regards to their reference frames.

At time  $t$ , the rotating  $x$ -axis makes an angle  $\Omega t$  with the inertial  $X$ -axis.

Table I. Variables Used to Derive Rotational Components of Momentum Equation

	Inertial Frame	Rotational Frame
$\Omega$		angular rate of rotation
Unit Vectors	$\bar{I}, \bar{J}$	$\bar{i}, \bar{j}$
Coordinates	$X, Y$	$x, y$
Velocity Vector	$\vec{U}$	$\vec{u}$
Velocity Components	$U, V$	$u, v$
Acceleration Vector	$\vec{A}$	$\vec{a}$
Acceleration Components	$A, B$	$a, b$

Applying equations of rotation, it follows that:

$$\begin{aligned}\vec{\mathbf{i}} &= \vec{\mathbf{I}} \cos \Omega t + \vec{\mathbf{J}} \sin \Omega t, \\ \vec{\mathbf{j}} &= -\vec{\mathbf{I}} \sin \Omega t + \vec{\mathbf{J}} \cos \Omega t,\end{aligned}\tag{II.15}$$

and:

$$\begin{aligned}x &= X \cos \Omega t + Y \sin \Omega t, \\ y &= -X \sin \Omega t + Y \cos \Omega t.\end{aligned}\tag{II.16}$$

The velocity vector in the rotational frame is:

$$\vec{\mathbf{u}} = \frac{dx}{dt} \vec{\mathbf{i}} + \frac{dy}{dt} \vec{\mathbf{j}} = u \vec{\mathbf{i}} + v \vec{\mathbf{j}},\tag{II.17}$$

where the first time derivative yields the velocity components of the rotational frame:

$$\begin{aligned}u &= \frac{dx}{dt} = \frac{dX}{dt} \cos \Omega t + \frac{dY}{dt} \sin \Omega t - \Omega X \sin \Omega t + \Omega Y \cos \Omega t, \\ v &= \frac{dy}{dt} = -\frac{dX}{dt} \sin \Omega t + \frac{dY}{dt} \cos \Omega t - \Omega X \cos \Omega t - \Omega Y \sin \Omega t.\end{aligned}\tag{II.18}$$

Similarly, the velocity vector in the inertial frame can be expressed as:

$$\vec{\mathbf{U}} = \frac{dX}{dt} \vec{\mathbf{I}} + \frac{dY}{dt} \vec{\mathbf{J}} = U \vec{\mathbf{I}} + V \vec{\mathbf{J}},\tag{II.19}$$

Algebraic and trigonometric manipulation of (II.15) yield:

$$\begin{aligned}\vec{\mathbf{I}} &= \vec{\mathbf{i}} \cos \Omega t - \vec{\mathbf{j}} \sin \Omega t, \\ \vec{\mathbf{J}} &= \vec{\mathbf{i}} \sin \Omega t + \vec{\mathbf{j}} \cos \Omega t.\end{aligned}\tag{II.20}$$

Using these and (II.19) yields:

$$\vec{\mathbf{U}} = \left( \frac{dX}{dt} \cos \Omega t + \frac{dY}{dt} \sin \Omega t \right) \vec{\mathbf{i}} + \left( -\frac{dX}{dt} \sin \Omega t + \frac{dY}{dt} \cos \Omega t \right) \vec{\mathbf{j}}.\tag{II.21}$$

This expression along with (II.15) and (II.18) reveal the following relationships between the inertial and rotational velocities:

$$\begin{aligned}U &= u - \Omega y, \\ V &= v + \Omega x.\end{aligned}\tag{II.22}$$

We now consider the rotational components of acceleration:

$$\bar{\mathbf{a}} = \frac{d^2x}{dt^2}\bar{\mathbf{i}} + \frac{d^2y}{dt^2}\bar{\mathbf{j}} = a\bar{\mathbf{i}} + b\bar{\mathbf{j}}. \quad (\text{II.23})$$

Taking the second derivative with respect to time of (II.16) yields:

$$\begin{aligned} a &= \left( \frac{d^2X}{dt^2} \cos \Omega t + \frac{d^2Y}{dt^2} \sin \Omega t \right) + 2\Omega \left( -\frac{dX}{dt} \sin \Omega t + \frac{dY}{dt} \cos \Omega t \right) \\ &\quad - \Omega^2 (-X \cos \Omega t + Y \sin \Omega t), \\ b &= \left( -\frac{d^2X}{dt^2} \sin \Omega t + \frac{d^2Y}{dt^2} \cos \Omega t \right) - 2\Omega \left( \frac{dX}{dt} \cos \Omega t + \frac{dY}{dt} \sin \Omega t \right) \\ &\quad - \Omega^2 (-X \sin \Omega t + Y \cos \Omega t). \end{aligned} \quad (\text{II.24})$$

We express the inertial acceleration vector as:

$$\bar{\mathbf{A}} = \frac{d^2X}{dt^2}\bar{\mathbf{I}} + \frac{d^2Y}{dt^2}\bar{\mathbf{J}} = A\bar{\mathbf{I}} + B\bar{\mathbf{J}}, \quad (\text{II.25})$$

This and (II.20) result in:

$$\bar{\mathbf{A}} = \left( \frac{d^2X}{dt^2} \cos \Omega t + \frac{d^2Y}{dt^2} \sin \Omega t \right) \bar{\mathbf{i}} + \left( -\frac{d^2X}{dt^2} \sin \Omega t + \frac{d^2Y}{dt^2} \cos \Omega t \right) \bar{\mathbf{j}}. \quad (\text{II.26})$$

Based on the preceeding, we generate a final simplifying expression that relates the rotational and inertial components of acceleration:

$$\begin{aligned} a &= A + 2\Omega V - \Omega^2 x, \\ b &= B + 2\Omega U - \Omega^2 y, \end{aligned} \quad (\text{II.27})$$

or combining this with (II.22) we have:

$$\begin{aligned} A &= a - 2\Omega v - \Omega^2 x, \\ B &= b + 2\Omega u - \Omega^2 y, \end{aligned} \quad (\text{II.28})$$

This equation shows the effects of rotation on the inertial acceleration vector. The first contribution proportional to  $\Omega$  and velocity is called Coriolis acceleration. The second contribution proportional to  $\Omega^2$  and the coordinates is called centrifugal acceleration. We now refine these equations for the Earth model.

### 3. Acceleration Components in the Earth Model

From henceforth we shall use the terms geophysical and “large-scale” interchangeably, but to be more precise a quantitative definition is offered. Let:

$$\Omega = \frac{2\pi}{\text{time to complete one revolution/rotation}}.$$

For example,  $\Omega_{\text{Earth}} = 7.27 \times 10^{-5}$  radians-second<sup>-1</sup> (one rotation every 24 hours). As before, we define:

$L$  = the length of a phenomenon,

$U$  = the speed of a particle within the phenomenon.

Using  $\Omega$ ,  $L$  and  $U$  we introduce a dimensionless parameter called the Rossby number:

$$\epsilon = \frac{U}{2\Omega L}, \quad (\text{II.29})$$

If the Rossby number  $\epsilon$  is of order one or less, the phenomenon is “large-scale” and the Earth’s rotation is a significant factor in the momentum equations [Ref. 25]. For example, a 500 kilometer long ocean current with a speed of 15 meter-second<sup>-1</sup> has a Rossby number  $\epsilon = .205$ . Therefore the current is large-scale (or geophysical) and is significantly affected by Earth’s rotation.

In order to model the Earth, the momentum equations for a rotating sphere are now considered. This non-inertial frame is complicated by the fact that at any given point on the sphere we perceive ourselves on a planar disc. To recreate this “human experience” we set up a three dimensional Cartesian system whose origin is at the point of the observer. The  $x$ -,  $y$ , and  $z$ -axis are positively oriented to the east, north, and “straight-up” respectively. The Earth’s axis of rotation however, is none of these, but rather passes through the North and South Poles. This conundrum, depicted in Figure 2, is the reference frame in which we develop the geophysical fluid flow equations.

Before continuing further, we revisit the two-dimensional rotating system presented in the previous section in Figure 1. We add a third dimension to this system

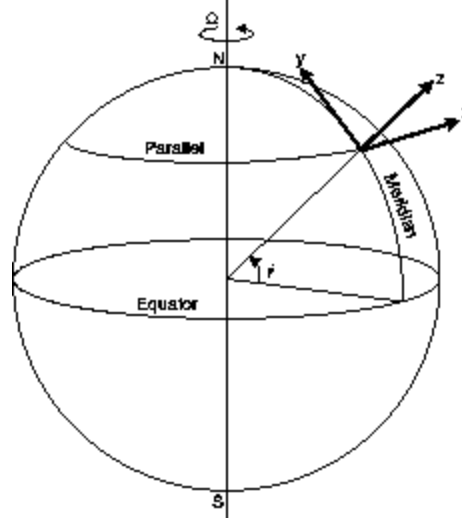


Figure 2. The Earth Model

by defining a unit vector  $\bar{\mathbf{k}}$  at the origin that is perpendicular to the plane. A rotation vector is described as  $\bar{\Omega} = \Omega \bar{\mathbf{k}}$ . We use this to write the inertial velocity equations (II.22) in vector form:

$$\bar{\mathbf{U}} = \begin{bmatrix} U \\ V \end{bmatrix} = \begin{bmatrix} u - \Omega y \\ v + \Omega x \end{bmatrix} = \bar{\mathbf{u}} + \begin{bmatrix} -\Omega y \\ +\Omega x \end{bmatrix}. \quad (\text{II.30})$$

Now let  $\bar{\mathbf{r}} = x\bar{\mathbf{i}} + y\bar{\mathbf{j}}$  and consider:

$$\bar{\Omega} \times \bar{\mathbf{r}} = \begin{vmatrix} \bar{\mathbf{i}} & \bar{\mathbf{j}} & \bar{\mathbf{k}} \\ 0 & 0 & \Omega \\ x & y & 0 \end{vmatrix} = \Omega(-y\bar{\mathbf{i}} + x\bar{\mathbf{j}}). \quad (\text{II.31})$$

This allows us to write the inertial velocity equations (II.22) in condensed vector form:

$$\bar{\mathbf{U}} = \bar{\mathbf{u}} + \bar{\Omega} \times \bar{\mathbf{r}}. \quad (\text{II.32})$$

Similarly, the inertial acceleration equations (II.28) in vector form are:

$$\bar{\mathbf{A}} = \bar{\mathbf{a}} + \begin{bmatrix} -2\Omega v \\ 2\Omega u \end{bmatrix} - \Omega^2 \begin{bmatrix} x \\ y \end{bmatrix}. \quad (\text{II.33})$$

Using an analogous approach we show that the condensed vector form of the inertial acceleration equations is:

$$\tilde{\mathbf{A}} = \tilde{\mathbf{a}} + 2\tilde{\boldsymbol{\Omega}} \times \tilde{\mathbf{u}} + \tilde{\boldsymbol{\Omega}} \times (\tilde{\boldsymbol{\Omega}} \times \tilde{\mathbf{r}}). \quad (\text{II.34})$$

In this form, the Coriolis acceleration is  $2\tilde{\boldsymbol{\Omega}} \times \tilde{\mathbf{u}}$  and the centrifugal acceleration is  $\tilde{\boldsymbol{\Omega}} \times (\tilde{\boldsymbol{\Omega}} \times \tilde{\mathbf{r}})$ . With respect to (II.32) and (II.34), the time derivative for the inertial frame is equivalent to applying the operator:

$$\frac{D}{Dt} + \tilde{\boldsymbol{\Omega}} \times, \quad (\text{II.35})$$

where  $\frac{D}{Dt}$  is the *derivative following a fluid* introduced in (II.11).

We now consider two additional simplifications in the development of the acceleration equations for the Earth model. First we neglect extraneous terms resulting from the Earth's curvature. In general this can be done if  $L \ll r$  where  $r$  is the radius of the sphere. On Earth,  $L < 1000$  kilometers is acceptable [Ref. 28]. A second simplification to (II.34) comes from our intuition about planetary phenomenom. The centrifugal force is an outwardly normal force, or from the vantage point of the Earth observer, a force that acts straight up. Yet nothing ever is “flung” upward from the face of the Earth because gravitational forces keep centrifugal forces in check. In the absence of rotation, gravity would hold the Earth together as a perfect sphere. The presence of rotation and accompanying centrifugal forces distort the sphere, flattening it to the extent that gravity and the centrifugal force negate each other. Hence, we neglect centrifugal forces in the Earth model and the inertial acceleration equations become:

$$\begin{aligned} A &= a - 2\Omega v, \\ B &= b + 2\Omega u, \end{aligned} \quad (\text{II.36})$$

or in vector form:

$$\tilde{\mathbf{A}} = \tilde{\mathbf{a}} + 2\tilde{\boldsymbol{\Omega}} \times \tilde{\mathbf{u}}. \quad (\text{II.37})$$

Using these equations, we continue with the Earth model.



Referring to Figure 2 we write the rotation vector  $\vec{\Omega}$  in terms of the unit vectors  $\vec{i}$ ,  $\vec{j}$ , and  $\vec{k}$ :

$$\vec{\Omega} = \Omega \cos \phi \vec{j} + \Omega \sin \phi \vec{k}, \quad (\text{II.38})$$

where  $\phi$  is the degree of latitude of the observer. Since  $\vec{i}$  is always orthogonal to  $\vec{\Omega}$ , it does not appear in the equation. Using (II.35) we write:

$$\vec{a} = \frac{D\vec{u}}{Dt} + 2\vec{\Omega} \times \vec{u}, \quad (\text{II.39})$$

where:

$$2\vec{\Omega} \times \vec{u} = \begin{vmatrix} \vec{i} & \vec{j} & \vec{k} \\ 0 & 2\Omega \cos \phi & 2\Omega \sin \phi \\ u & v & w \end{vmatrix}, \quad (\text{II.40})$$

or:

$$2\vec{\Omega} \times \vec{u} = (2\Omega w \cos \phi - 2\Omega v \sin \phi)\vec{i} + 2\Omega u \sin \phi \vec{j} - 2\Omega u \cos \phi \vec{k}. \quad (\text{II.41})$$

Therefore:

$$\begin{aligned} a_x &= \frac{Du}{Dt} + 2\Omega w \cos \phi - 2\Omega v \sin \phi, \\ a_y &= \frac{Dv}{Dt} + 2\Omega u \sin \phi, \\ a_z &= \frac{Dw}{Dt} - 2\Omega u \cos \phi. \end{aligned} \quad (\text{II.42})$$

For convenience, we define the following quantities:

$$\begin{aligned} \text{Coriolis Parameter:} \quad f &= 2\Omega \sin \phi, \\ \text{Reciprocal Coriolis Parameter:} \quad f_* &= 2\Omega \cos \phi, \end{aligned} \quad (\text{II.43})$$

allowing us to rewrite (II.42) as:

$$\begin{aligned} a_x &= \frac{Du}{Dt} + f_* w - f v, \\ a_y &= \frac{Dv}{Dt} + f u, \\ a_z &= \frac{Dw}{Dt} - f_* u. \end{aligned} \quad (\text{II.44})$$

The angle  $\phi$ , and therefore the Coriolis parameter, is positive in the Northern Hemisphere and negative in the Southern Hemisphere. The Coriolis parameter is zero on the Equator where  $\phi = 0$ . The reciprocal Coriolis parameter is positive everywhere except at the poles ( $\phi = \pm 90$ ) where it is zero.

One final simplification is now applied. As stated earlier, our model of geophysical fluid dynamics is based on the shallow water assumption where the vertical dimension ( $D$ ) is very small relative to the horizontal dimensions ( $L$ ):

$$\frac{D}{L} \ll 1.$$

In other words, geophysical fluid flow is “almost two-dimensional” and therefore vertical flow components are negligible (e.g.  $w \ll u, v$  and  $a_z \approx 0$ ). Thus we rewrite (II.44) as:

$$\boxed{a_x = \frac{Du}{Dt} - fv, \quad a_y = \frac{Dv}{Dt} + fu, \quad a_z = 0.} \quad (\text{II.45})$$

These are the acceleration components of the Earth model that are used to generate the momentum equations for the geophysical fluid flow model.

#### 4. Forces Acting on a Fluid Control Volume

Two types of forces act on a fluid in a control volume: *Body forces* which are proportional to the volume mass and *surface forces* which are proportional to the volume surface area.

Gravity, the only applicable force in the Earth model, acts along the  $z$ -axis toward the center of the Earth. It acts on a rectangular volume element with sides  $dx$ ,  $dy$ , and  $dz$  and is given by:

$$F_{\text{gravity}} = -mg = -(\rho \, dx \, dy \, dz)g = -\rho g dV, \quad (\text{II.46})$$

where  $dV$  is the incremental volume of the fluid element.

Salient surface forces include pressure and viscosity. Pressure acts in a direction normal to the volume’s surface as shown in Figure 3. The total difference in

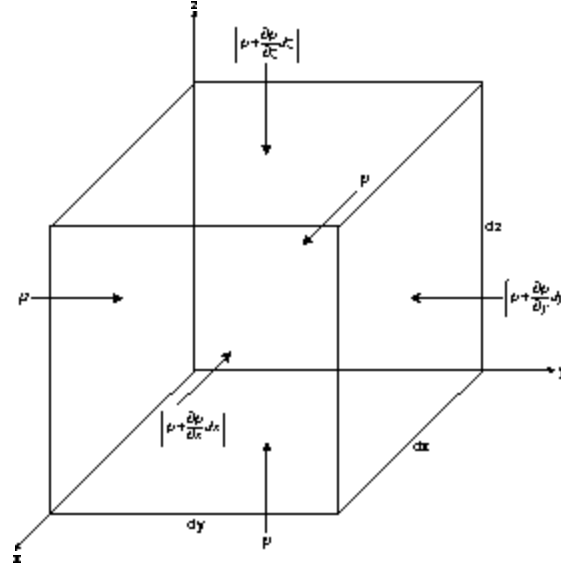


Figure 3. Pressure Effects on a Rectangular Fluid Volume

pressure along  $dx$  is:

$$\frac{\partial p}{\partial x} dx.$$

To obtain the total force due to pressure in the  $x$ -direction, this expression is multiplied by the surface area ( $dy dz$ ) upon which it acts. The result is:

$$F_{pressure_x} = -\frac{\partial p}{\partial x} dx dy dz = -\frac{\partial p}{\partial x} dV. \quad (\text{II.47})$$

This force acts in the direction of the negative gradient (e.g. from an area of high pressure to an area of low pressure). Similarly the expressions:

$$F_{pressure_y} = -\frac{\partial p}{\partial y} dV, \quad F_{pressure_z} = -\frac{\partial p}{\partial z} dV, \quad (\text{II.48})$$

describe the force due to pressure in the  $y$ - and  $z$ -directions:

Viscosity manifests itself in surfaces forces called shear. Figure 4 summarizes the viscous stress tensor. Viscous stresses are symmetrical (e.g.  $\tau_{ij} = \tau_{ji}$ ). A summation of viscous forces in the  $x$ -direction yields:

$$F_{viscous_x} = \left( \frac{\partial \tau_{xx}}{\partial x} dx \right) dy dz + \left( \frac{\partial \tau_{xy}}{\partial y} dy \right) dx dz + \left( \frac{\partial \tau_{xz}}{\partial z} dz \right) dx dy, \quad (\text{II.49})$$

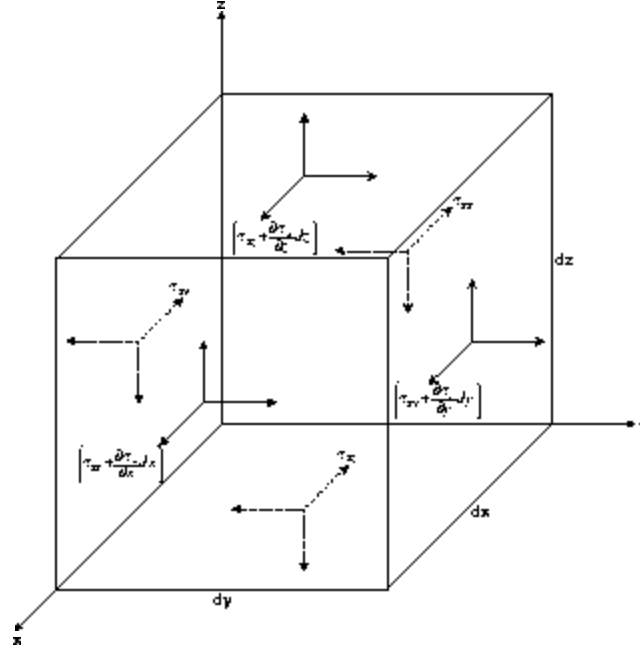


Figure 4.  $x$ -Components of Viscous Stress Tensor on a Rectangular Fluid Volume

which is rewritten for our rectangular control volume as:

$$F_{viscous_x} = \left( \frac{\partial \tau_{xx}}{\partial x} + \frac{\partial \tau_{xy}}{\partial y} + \frac{\partial \tau_{xz}}{\partial z} \right) dV \quad (\text{II.50})$$

Similarly in the  $y$ - and  $z$ -directions:

$$F_{viscous_y} = \left( \frac{\partial \tau_{xy}}{\partial x} + \frac{\partial \tau_{yy}}{\partial y} + \frac{\partial \tau_{yz}}{\partial z} \right) dV, \quad (\text{II.51})$$

$$F_{viscous_z} = \left( \frac{\partial \tau_{xz}}{\partial x} + \frac{\partial \tau_{yz}}{\partial y} + \frac{\partial \tau_{zz}}{\partial z} \right) dV.$$

The surface forces and body forces are combined to generate the total force equations:

$$\begin{aligned}
 F_x &= \left( -\frac{\partial p}{\partial x} + \frac{\partial \tau_{xx}}{\partial x} + \frac{\partial \tau_{xy}}{\partial y} + \frac{\partial \tau_{xz}}{\partial z} \right) dV \\
 F_y &= \left( -\frac{\partial p}{\partial y} + \frac{\partial \tau_{xy}}{\partial x} + \frac{\partial \tau_{yy}}{\partial y} + \frac{\partial \tau_{yz}}{\partial z} \right) dV \\
 F_z &= \left( -\frac{\partial p}{\partial z} - \rho g + \frac{\partial \tau_{xz}}{\partial x} + \frac{\partial \tau_{yz}}{\partial y} + \frac{\partial \tau_{zz}}{\partial z} \right) dV
 \end{aligned} \tag{II.52}$$

We now have the necessary expressions to set up the momentum equations for the geophysical fluid flow model.

## 5. The Momentum Equation for Geophysical Fluid Flow

Applying Newton's Second Law ( $F_i = ma_i = \rho a_i dV$ ) and using (II.45) and (II.52), we now write the momentum equations for the geophysical flow model:

$$\begin{aligned}
 \rho a_x &= \rho \left( \frac{Du}{Dt} - fv \right) = -\frac{\partial p}{\partial x} + \frac{\partial \tau_{xx}}{\partial x} + \frac{\partial \tau_{xy}}{\partial y} + \frac{\partial \tau_{xz}}{\partial z}, \\
 \rho a_y &= \rho \left( \frac{Dv}{Dt} + fu \right) = -\frac{\partial p}{\partial y} + \frac{\partial \tau_{xy}}{\partial x} + \frac{\partial \tau_{yy}}{\partial y} + \frac{\partial \tau_{yz}}{\partial z}, \\
 \rho a_z &= 0 = -\frac{\partial p}{\partial z} - \rho g + \frac{\partial \tau_{xz}}{\partial x} + \frac{\partial \tau_{yz}}{\partial y} + \frac{\partial \tau_{zz}}{\partial z}.
 \end{aligned} \tag{II.53}$$

These equations are simplified using the assumptions described earlier:

- *The Fluid is Incompressible:* Density is independent of pressure, and therefore the model is uncoupled from thermodynamic considerations.
- *The Fluid is Inviscid:* All viscous forces are equal to zero.
- *The Fluid is Homogeneous:* We need not deal with the complexities of density stratification (this simplification will be relaxed in Chapter V).
- *Centrifugal Forces are Negated by Gravity:* This allows simplification of the acceleration terms.

- $L \ll r$ : This allows us to neglect terms that arise in the acceleration components that result from the curvature of the Earth (e.g. see Cushman-Roisin (1994) [Ref. 28]).
- *The Flow is Primarily Horizontal*: Velocity and acceleration terms in the  $z$ -direction are negligible.

Since viscosity terms are negligible (II.53) becomes:

$$\begin{aligned}\rho \left( \frac{Du}{Dt} - fv \right) &= -\frac{\partial p}{\partial x}, \\ \rho \left( \frac{Dv}{Dt} + fu \right) &= -\frac{\partial p}{\partial y} \\ 0 &= -\frac{\partial p}{\partial z} - \rho g.\end{aligned}\tag{II.54}$$

Expanding the operator  $\frac{D}{Dt}$  introduced in (II.11) produces the momentum equations in simplified form:

$x\text{-momentum:}$	$\frac{\partial u}{\partial t} + u \frac{\partial u}{\partial x} + v \frac{\partial u}{\partial y} - fv = -\frac{1}{\rho} \frac{\partial p}{\partial x},$	$(\text{II.55})$
$y\text{-momentum:}$	$\frac{\partial v}{\partial t} + u \frac{\partial v}{\partial x} + v \frac{\partial v}{\partial y} + fu = -\frac{1}{\rho} \frac{\partial p}{\partial y},$	
$z\text{-momentum:}$	$0 = -\frac{1}{\rho} \frac{\partial p}{\partial z} - g.$	

Since geophysical flow is “primarily horizontal”, the term  $w \frac{\partial}{\partial z}$  does not appear in the  $x$ - and  $y$ -momentum equations. Equation (II.55) together with the continuity equation (II.6) are used to construct a shallow water model.

## 6. Governing Equations for the Shallow Water Model

The shallow water model is depicted in Figure 5. We define a variable  $h$  as the height of the fluid above a reference level  $z = 0$ . The variable  $h$  varies with  $x$ ,  $y$ , and  $t$  and describes the fluid action at the surface. The “bottom” of the shallow

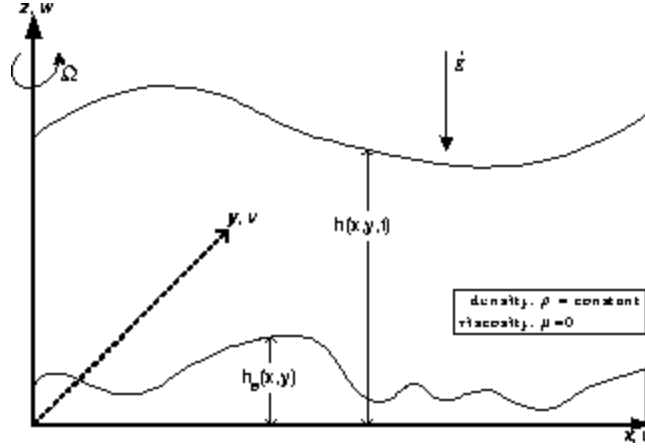


Figure 5. The Shallow Water Model

water environment consists of a rigid surface whose height that does not vary with time and is given by  $z = h_B(x, y)$ . We let  $H = h(x, y, t) - h_B(x, y)$  where  $H$  is the depth of the fluid layer with respect to the bottom contour. If  $L$  is the horizontal scale, then by the shallow water assumption it is true that  $H \ll L$ .

It is now possible manipulate the governing equations for the Earth model to produce the shallow water model. Integrating the  $z$ -component of the momentum equation (II.55) yields:

$$p(x, y, z, t) = -\rho g z + \tilde{p}(x, y, t) \quad (\text{II.56})$$

On the surface,  $z = h(x, y, t)$ , pressure  $p$  equals some ambient pressure  $P_0$ . Therefore:

$$p(x, y, z, t) = \rho g [h(x, y, t) - z] + P_0. \quad (\text{II.57})$$

Dropping the variable dependencies for brevity, (II.57) is rewritten as:

$$p = \rho g (h - z) + P_0. \quad (\text{II.58})$$

From (II.58) we obtain pressure gradients in the horizontal  $x$  and  $y$  directions:

$$\frac{\partial p}{\partial x} = \rho g \frac{\partial h}{\partial x}, \quad \frac{\partial p}{\partial y} = \rho g \frac{\partial h}{\partial y}. \quad (\text{II.59})$$

Thus we rewrite the  $x$ - and  $y$ -momentum expressions (II.55) as:

$$\begin{aligned} \text{x-momentum: } & \frac{\partial u}{\partial t} + u \frac{\partial u}{\partial x} + v \frac{\partial u}{\partial y} - fv = -g \frac{\partial h}{\partial x}, \\ \text{y-momentum: } & \frac{\partial v}{\partial t} + u \frac{\partial v}{\partial x} + v \frac{\partial v}{\partial y} + fu = -g \frac{\partial h}{\partial y}, \end{aligned} \quad (\text{II.60})$$

Equation II.59 also implies that the horizontal acceleration components,  $a_x$  and  $a_y$ , given by (II.45) and (II.55) are independent of  $z$ . It follows that the horizontal velocity components,  $u$  and  $v$ , are independent of  $z$ . This allows us to uncouple (II.6) and solve for  $w(x, y, z, t)$ :

$$w(x, y, z, t) = -z \left( \frac{\partial u(x, y, t)}{\partial x} + \frac{\partial v(x, y, t)}{\partial y} \right) + \bar{w}(x, y, t) \quad (\text{II.61})$$

Now consider the flow along the bottom contour  $h_B(x, y)$ . Since the contour is rigid, there is no normal flow. Any velocity in the  $z$ -direction is due to fluid flowing tangent to the bottom contour. Figure 6 depicts this consideration for the  $x$ - and  $z$ -directions. If  $u$  is the velocity component in the  $x$ -direction flowing tangent to the

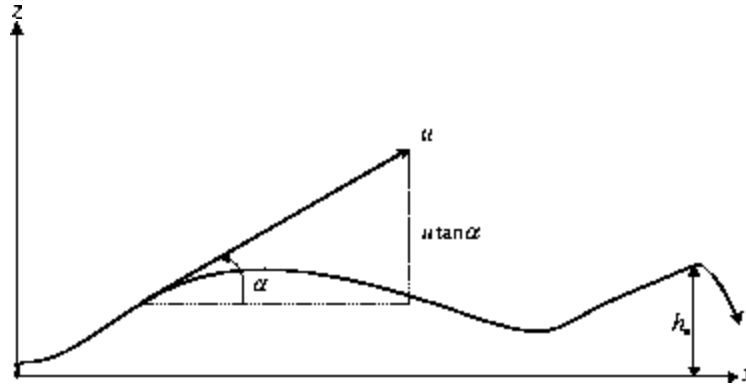


Figure 6. Flow Along the Bottom Contour in the  $x$ -Direction

bottom contour, its contribution to  $w$  is:

$$u \tan(\alpha) = u \frac{\partial h_B}{\partial x}, \quad (\text{II.62})$$



where  $\alpha$  is the angle of the line tangent to  $h_B$  and  $x$ -axis. Similarly in the  $y$ -direction, the contribution to  $w$  is:

$$v \tan(\beta) = v \frac{\partial h_B}{\partial y}, \quad (\text{II.63})$$

where  $\beta$  is the angle of the line tangent to  $h_B$  and  $y$ -axis. It follows then that:

$$w(x, y, z = h_B, t) = u \frac{\partial h_B}{\partial x} + v \frac{\partial h_B}{\partial y}. \quad (\text{II.64})$$

Therefore from (II.61) and (II.64) we generate an expression for  $w$  along the bottom contour:

$$w = (h_B - z) \left( \frac{\partial u}{\partial x} + \frac{\partial v}{\partial y} \right) + u \frac{\partial h_B}{\partial x} + v \frac{\partial h_B}{\partial y}. \quad (\text{II.65})$$

A corresponding condition at the surface,  $z = h$  yields:

$$w(x, y, z = h, t) = \frac{\partial h}{\partial t} + u \frac{\partial h}{\partial x} + v \frac{\partial h}{\partial y}. \quad (\text{II.66})$$

Since the surface is not rigid, we pick up  $\frac{\partial h}{\partial t}$  in the expression. Therefore, (II.65) and (II.66) generate:

$$\frac{\partial h}{\partial t} + u \frac{\partial h}{\partial x} + v \frac{\partial h}{\partial y} = (h_B - h) \left( \frac{\partial u}{\partial x} + \frac{\partial v}{\partial y} \right) + u \frac{\partial h_B}{\partial x} + v \frac{\partial h_B}{\partial y}, \quad (\text{II.67})$$

which is simplified to:

$$\boxed{\frac{\partial h}{\partial t} + \frac{\partial}{\partial x} [u (h - h_B)] + \frac{\partial}{\partial y} [v (h - h_B)] = 0.} \quad (\text{II.68})$$

Equations (II.60) and (II.68) are the governing equations for the shallow water model. In its current form the model is non-linear. We desire a linear form for subsequent investigations.

## 7. Linearizing the Shallow Water Model

To linearize the shallow water model we conduct a perturbation analysis on the  $x$ - and  $y$ -momentum equations (II.60) and the vertical momentum equation (II.68). Perturbation analysis on the horizontal flow is accomplished by assuming that the

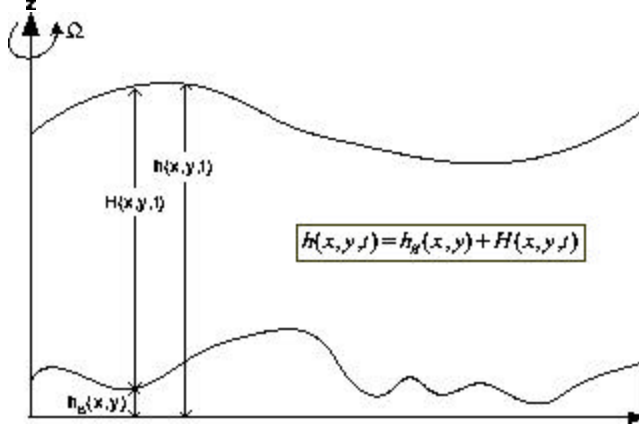


Figure 7. Shallow Water Model Cross Section with  $h = H + h_B$

$x$ - and  $y$ -components of velocity are dominated by constant terms ( $U$  and  $V$ ). Superimposed on these are small variations,  $u^*(x, y, t)$  and  $v^*(x, y, t)$ . Mathematically stated:

$$\begin{aligned} u &= U + u^*, \text{ where } U \text{ is constant and } u^* \sim O(\delta) \ll U, \\ v &= V + v^*, \text{ where } V \text{ is constant and } v^* \sim O(\delta) \ll V. \end{aligned} \quad (\text{II.69})$$

Applying these to (II.60) yields:

$$\begin{aligned} \frac{\partial u^*}{\partial t} + (U + u^*) \frac{\partial u^*}{\partial x} + (V + v^*) \frac{\partial u^*}{\partial y} - f(V + v^*) &= -g \frac{\partial h}{\partial x}, \\ \frac{\partial v^*}{\partial t} + (U + u^*) \frac{\partial v^*}{\partial x} + (V + v^*) \frac{\partial v^*}{\partial y} + f(U + u^*) &= -g \frac{\partial h}{\partial y}. \end{aligned} \quad (\text{II.70})$$

Ignoring terms of  $O(\delta^2)$  results in the following simplification:

$$\begin{aligned} \frac{\partial u^*}{\partial t} + U \frac{\partial u^*}{\partial x} + V \frac{\partial u^*}{\partial y} - f(V + v^*) &= -g \frac{\partial h}{\partial x}, \\ \frac{\partial v^*}{\partial t} + U \frac{\partial v^*}{\partial x} + V \frac{\partial v^*}{\partial y} + f(U + u^*) &= -g \frac{\partial h}{\partial y}. \end{aligned} \quad (\text{II.71})$$

A similar perturbation approach is applied to the vertical momentum equation of the shallow-water model (II.68). We let  $h(x, y, t) = h_B(x, y) + H(x, y, t)$  as depicted in Figure 7, Applying this to (II.68) yields:

$$\frac{\partial H}{\partial t} + \frac{\partial}{\partial x}(uH) + \frac{\partial}{\partial y}(vH) = 0. \quad (\text{II.72})$$

where  $H = h - h_B$ . We refine  $H(x, y, t)$  further into two parts as depicted in Figure 8. The component,  $H_0(x, y)$  is resultant from the constant velocity terms  $U$  and  $V$

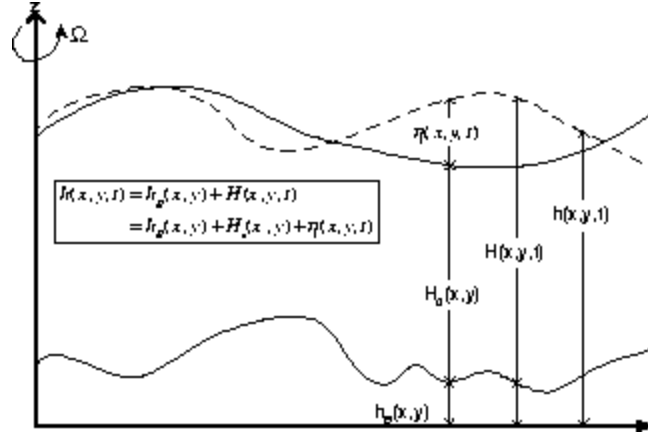


Figure 8. Shallow Water Model Cross Section with  $h = H_0 + \eta + h_B$

introduced in (II.69). If  $U$  and  $V$  are zero then  $H_0$  is constant. Likewise, if the bottom is flat, then there is no velocity in the vertical direction along the bottom that results from a non-zero  $U$  and  $V$ , and again  $H_0$  is constant. Superimposed on  $H_0$  is a small amplitudinal variation that represents the wave action and is given by  $\eta(x, y, t)$ . Mathematically stated this is:

$$H(x, y, t) = H_0(x, y) + \eta(x, y, t) \text{ where } \eta \sim O(\delta) \ll H_0 \quad (\text{II.73})$$

Applying these terms, as well as the perturbation terms introduced for the horizontal velocity allows us to rewrite (II.72) as follows:

$$\frac{\partial \eta}{\partial t} + \frac{\partial}{\partial x} [(U + u^*)(H_0 + \eta)] + \frac{\partial}{\partial y} [(V + v^*)(H_0 + \eta)] = 0. \quad (\text{II.74})$$

Neglecting terms of  $O(\delta^2)$  gives us:

$$\frac{\partial \eta}{\partial t} + \frac{\partial}{\partial x} [U(H_0 + \eta) + u^*H_0] + \frac{\partial}{\partial y} [V(H_0 + \eta) + v^*H_0] = 0. \quad (\text{II.75})$$

Since  $U$  and  $V$  are constant, II.75 becomes:

$$\frac{\partial \eta}{\partial t} + U \frac{\partial}{\partial x}(H_0 + \eta) + \frac{\partial}{\partial x}(u^* H_0) + V \frac{\partial}{\partial y}(H_0 + \eta) + \frac{\partial}{\partial y}(v^* H_0) = 0. \quad (\text{II.76})$$

This can be further simplified if the bottom is flat (e.g.  $H_0$  is constant):

$$\frac{\partial \eta}{\partial t} + U \frac{\partial \eta}{\partial x} + V \frac{\partial \eta}{\partial y} + H_0 \left( \frac{\partial u^*}{\partial x} + \frac{\partial v^*}{\partial y} \right) = 0. \quad (\text{II.77})$$

Finally, if we assume that  $V$  and  $U$  are zero (e.g. no advection), the equation becomes:

$$\boxed{\frac{\partial \eta}{\partial t} + H_0 \left( \frac{\partial u^*}{\partial x} + \frac{\partial v^*}{\partial y} \right) = 0.} \quad (\text{II.78})$$

This is the simplest form of the linearized vertical motion component of the shallow water model.

We now revisit the horizontal flow equations (II.71). By including the refinements and perturbations on  $h$ , (II.71) becomes:

$$\begin{aligned} \frac{\partial u^*}{\partial t} + U \frac{\partial u^*}{\partial x} + V \frac{\partial u^*}{\partial y} - f(V + v^*) &= -g \left( \frac{\partial h_B}{\partial x} + \frac{\partial H_0}{\partial x} + \frac{\partial \eta}{\partial x} \right), \\ \frac{\partial v^*}{\partial t} + U \frac{\partial v^*}{\partial x} + V \frac{\partial v^*}{\partial y} + f(U + u^*) &= -g \left( \frac{\partial h_B}{\partial y} + \frac{\partial H_0}{\partial y} + \frac{\partial \eta}{\partial y} \right). \end{aligned} \quad (\text{II.79})$$

Since we have assumed no advection ( $U, V = 0$  and therefore  $H_0$  is constant) and that the bottom is flat ( $h_B = 0$ ), the linearized horizontal flow component of the shallow water equation can be stated as:

$$\boxed{\begin{aligned} \frac{\partial u^*}{\partial t} - f v^* &= -g \frac{\partial \eta}{\partial x}, \\ \frac{\partial v^*}{\partial t} + f u^* &= -g \frac{\partial \eta}{\partial y}. \end{aligned}} \quad (\text{II.80})$$

Equations II.78 and II.80 are the governing equations for the linearized shallow water model. They will be further refined in the following section.

## 8. Deriving the Klein-Gordon Equation

We now combine linearized components of the shallow water model to obtain the well known Klein-Gordon, or dispersive wave equation. A step-by-step derivation follows.

**Step 1:** Perform the following substitutions to (II.78) and (II.80):

$$\hat{u} = u^* H_0 \text{ and } \hat{v} = v^* H_0.$$

The result is:

$$\frac{\partial \hat{u}}{\partial t} - f \hat{v} = -g H_0 \frac{\partial \eta}{\partial x}, \quad (\text{II.81})$$

$$\frac{\partial \hat{v}}{\partial t} + f \hat{u} = -g H_0 \frac{\partial \eta}{\partial y}, \quad (\text{II.82})$$

$$\frac{\partial \eta}{\partial t} + \frac{\partial \hat{u}}{\partial x} + \frac{\partial \hat{v}}{\partial y} = 0. \quad (\text{II.83})$$

**Step 2:** Assume  $f$  is constant and take the partial derivative of (II.81) with respect to  $x$ :

$$\frac{\partial}{\partial x} \left( \frac{\partial \hat{u}}{\partial t} \right) - f \frac{\partial \hat{v}}{\partial x} = -g H_0 \frac{\partial^2 \eta}{\partial x^2},$$

and the partial derivative of (II.82) with respect to  $y$ :

$$\frac{\partial}{\partial y} \left( \frac{\partial \hat{v}}{\partial t} \right) + f \frac{\partial \hat{u}}{\partial y} = -g H_0 \frac{\partial^2 \eta}{\partial y^2},$$

and add the resulting equations:

$$\frac{\partial}{\partial t} \left( \frac{\partial \hat{u}}{\partial x} + \frac{\partial \hat{v}}{\partial y} \right) - f \left( \frac{\partial \hat{v}}{\partial x} - \frac{\partial \hat{u}}{\partial y} \right) = -g H_0 \nabla^2 \eta. \quad (\text{II.84})$$

**Step 3:** Take the partial derivative of (II.81) with respect to  $y$ :

$$\frac{\partial}{\partial y} \left( \frac{\partial \hat{u}}{\partial t} \right) - f \frac{\partial \hat{v}}{\partial y} = -g H_0 \frac{\partial}{\partial y} \left( \frac{\partial \eta}{\partial x} \right),$$

and the partial derivative of (II.82) with respect to  $x$ :

$$\frac{\partial}{\partial x} \left( \frac{\partial \hat{v}}{\partial t} \right) + f \frac{\partial \hat{u}}{\partial x} = -g H_0 \frac{\partial}{\partial x} \left( \frac{\partial \eta}{\partial y} \right),$$

and subtract the resulting equations:

$$\frac{\partial}{\partial t} \left( \frac{\partial \hat{u}}{\partial y} - \frac{\partial \hat{v}}{\partial x} \right) - f \left( \frac{\partial \hat{v}}{\partial y} + \frac{\partial \hat{u}}{\partial x} \right) = 0. \quad (\text{II.85})$$

**Step 4:** Take the partial derivative of (II.84) with respect to  $t$  and rearrange the resulting terms:

$$f \left[ \frac{\partial}{\partial t} \left( \frac{\partial \hat{v}}{\partial x} - \frac{\partial \hat{u}}{\partial y} \right) \right] = \frac{\partial^2}{\partial t^2} \left( \frac{\partial \hat{u}}{\partial x} + \frac{\partial \hat{v}}{\partial y} \right) + gH_0 \frac{\partial}{\partial t} (\nabla^2 \eta).$$

Multiply (II.85) by  $f$  and rearrange the resulting terms:

$$-f \left[ \frac{\partial}{\partial t} \left( \frac{\partial \hat{v}}{\partial x} - \frac{\partial \hat{u}}{\partial y} \right) \right] = f^2 \left( \frac{\partial \hat{v}}{\partial y} + \frac{\partial \hat{u}}{\partial x} \right).$$

Summing these yields:

$$\left( \frac{\partial^2}{\partial t^2} + f^2 \right) \left( \frac{\partial \hat{u}}{\partial x} + \frac{\partial \hat{v}}{\partial y} \right) + gH_0 \frac{\partial}{\partial t} (\nabla^2 \eta) = 0. \quad (\text{II.86})$$

**Step 5:** Using (II.83) rewrite (II.86) as:

$$\frac{\partial}{\partial t} \left( \frac{\partial^2 \eta}{\partial t^2} + f^2 \eta - gH_0 \nabla^2 \eta \right) = 0. \quad (\text{II.87})$$

**Step 6:** Integrating (II.87) with respect to  $t$  and letting  $C_0^2 = gH_0$  yields:

$$\boxed{\frac{\partial^2 \eta}{\partial t^2} - C_0^2 \nabla^2 \eta + f^2 \eta = S(x, y)}, \quad (\text{II.88})$$

where  $S(x, y)$  is an arbitrary function of integration. Equation II.88, the linear inhomogeneous form of the Klein-Gordon equation, is a restatement of the linearized shallow water equation. It also describes other behaviors such as lateral vibrations of membrane strips and acoustic pressure waves in dispersive media [Ref. 24]. We continue with analytical considerations of the Klein-Gordon equation and the concept of dispersive waves in the next section.

## 9. Analytic Considerations of the Klein-Gordon Equation

Consider a homogeneous form of the Klein-Gordon Equation in one dimension:

$$\frac{\partial^2 \eta}{\partial t^2} - C_0^2 \frac{\partial^2 \eta}{\partial x^2} + f^2 \eta = 0. \quad (\text{II.89})$$

This equation has the following solution:

$$\eta(x, t) = \exp[i(kx - \omega t)], \quad (\text{II.90})$$

where:

$$\omega^2 = C_0^2 k^2 + f^2. \quad (\text{II.91})$$

Here  $\omega$  is the angular frequency and  $k$  is the wave number. Solving for  $k$  one obtains the dispersion equation for the Klein-Gordon equation:

$$k = \frac{\sqrt{\omega^2 - f^2}}{C_0}. \quad (\text{II.92})$$

The phase velocity of the wave (e.g. the speed of a wave crest) is given by:

$$v_p = \frac{\omega}{k}. \quad (\text{II.93})$$

Group velocity is the velocity at which the wave energy propagates and is given by:

$$v_g = \frac{\partial \omega}{\partial k} \quad (\text{II.94})$$

If the phase and group velocities are not equal, the wave is dispersive and the wave shape deforms as it travels. Using (II.91) we have:

$$v_p = \frac{\sqrt{C_0^2 k^2 + f^2}}{k}, \quad v_g = \frac{k C_0^2}{\sqrt{C_0^2 k^2 + f^2}}. \quad (\text{II.95})$$

If  $f \neq 0$ , then  $v_p \neq v_g$ , and the solution to the Klein-Gordon equation produces dispersive waves. If  $f = 0$ , then  $v_p = v_g = C_0$  and the resulting wave is non-dispersive. With respect to the Earth model,  $f$  is the Coriolis parameter given by (II.43). The magnitude of  $f$  increases as we go north or south from the equator. Thus dispersion effects will increase away from the equator. Hence the rotating Earth, with the exception of the equator where  $f = 0$ , is a dispersive environment with respect to the shallow-water model.

This form of the Klein-Gordon equation is used in initial investigations of the Higdon NRBC because it is a relatively simple mathematical model of dispersive wave

behavior. These effects are an integral part in the development of Higdon NRBC's. The simplicity of the equation also makes possible comparisons between numerical and analytical solutions and provides for easy testing of proposed boundary conditions. Chapter 2 follows with a description of the Higdon NRBC.



### III. HIGDON NON-REFLECTING BOUNDARY CONDITIONS

Our goal is to accurately describe the propagation of dispersive waves in a “manageable” domain. Such a domain is one that will not overwhelm computer capabilities when applying numerical techniques to its interior and boundaries. The actual domain in which the wave travels is much larger, or perhaps infinite. To restrict ourselves to a smaller domain of interest, artificial boundaries are constructed that allow waves that impinge upon them to freely pass.

Constructing the mathematical analog for a NRBC, is elusive. Schemes exist that allow for the total absorption of non-dispersive waves. However, when dealing with dispersive waves, the results are less than perfect, and spurious reflections occur at the artificial boundary. Hence the NRBC problem is one of optimization (e.g. minimizing unwanted reflection thus allowing most of the wave’s energy to pass). The Higdon NRBC is the focus for our investigation because it exhibits numerous advantages. We initially use a model that requires a single artificial boundary. From this we develop the details of the Higdon NRBC.

#### A. THE SEMI-INFINITE WAVE GUIDE PROBLEM

The semi-infinite wave guide problem provides a vehicle to explore the properties of the Higdon NRBC and is depicted in Figure 9. A Cartesian coordinate system

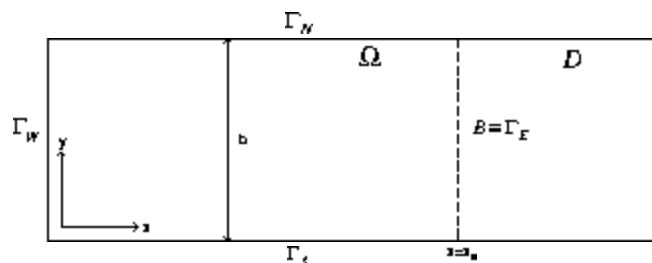


Figure 9. Semi-Infinite Wave Guide

$(x, y)$  is introduced such that the wave-guide is parallel to the  $x$ -direction. The width of the wave-guide is denoted by  $b$ . In the wave-guide we consider the inhomogeneous Klein-Gordon equation (II.88):

$$\frac{\partial^2 \eta}{\partial t^2} - C_0^2 \nabla^2 \eta + f^2 \eta = S,$$

where,  $\eta$  is the unknown wave field,  $C_0$  is the given reference wave speed,  $f$  is the given dispersion parameter, and  $S$  is a given wave source function.  $C_0$  and  $f$  are functions of location, but it is assumed that outside a finite region they do not depend on  $x$ . The wave source  $S$  is a function of location and time, but is assumed to have local support.

Dirichlet or Neumann boundary conditions are specified on the north and south boundaries,  $\Gamma_S$  and  $\Gamma_N$ :

$$\eta = 0 \quad \text{or} \quad \frac{\partial \eta}{\partial y} = 0. \quad (\text{III.1})$$

In acoustics, these correspond to “soft wall” and “hard wall” conditions, respectively. A Dirichlet boundary condition is prescribed on the west boundary  $\Gamma_W$ :

$$\eta(0, y, t) = \eta_W(y, t), \quad (\text{III.2})$$

where  $\eta_W(y, t)$  is an incoming wave function. As  $x \rightarrow \infty$ , the solution is bounded and does not include incoming waves. To complete the problem statement, the initial conditions:

$$\eta(x, y, 0) = \eta_0, \quad \frac{\partial \eta}{\partial t}(x, y, 0) = w_0, \quad (\text{III.3})$$

are given at time  $t = 0$  for the entire domain. We assume that the functions  $\eta_0$  and  $w_0$  have local support.

We now truncate the semi-infinite domain by introducing an artificial east boundary  $\mathcal{E}$  at  $x = x_E$  which we call  $\Gamma_E$ . This boundary divides the original semi-infinite domain into two subdomains: an exterior domain  $\mathcal{D}$ , and a finite computational domain  $\Omega$  bounded by  $\Gamma_N$ ,  $\Gamma_S$ ,  $\Gamma_E$ , and  $\Gamma_W$ . We chose the location of  $\Gamma_E$

such that the entire support of  $S$ ,  $\eta_0$ , and  $w_0$  is in  $\Omega$ . Thus on  $\Gamma_E$  the homogeneous counterpart of the Klein-Gordon equation holds:

$$\frac{\partial^2 \eta}{\partial t^2} - C_0^2 \nabla^2 \eta + f^2 \eta = 0.$$

On  $\Gamma_E$ ,  $C_0^2$  and  $f^2$  are  $y$ -dependent (or, as a special case constant).

## B. THE HIGDON NON-REFLECTING BOUNDARY CONDITION

The Higdon condition for non-dispersive acoustic and elastic waves was presented and analyzed in a sequence of papers (see e.g. [Ref. 17] - [Ref. 20]). These were later extended to include dispersive waves [Ref. 21]. To obtain a well-posed problem for the finite domain  $\Omega$  (see Figure 9) we impose a reformulation of the Higdon NRBC [Ref. 21] on  $\Gamma_E$  to reduce spurious wave reflection.

The Higdon NRBC is obtained by composing simple first-order differential operators. For example, a Higdon NRBC of order  $J$  (denoted by  $H_J$ ) is:

$$\boxed{\prod_{j=1}^J \left( \frac{\partial}{\partial t} + C_j \frac{\partial}{\partial x} \right) \eta = 0} \quad (\text{III.4})$$

In this section we will show that Higdon NRBC's have several advantages including:

- Their reflection coefficients are easily determined.
- They are exact for all waves that propagate in an  $x$ -direction with phase speeds equal to either of  $C_1$  through  $C_J$ .
- They constitute a sequence of conditions of increasing order. No asymptotic approximation is involved in their construction, enabling one to obtain solutions with unlimited accuracy.
- They are robust. Reflection coefficients become smaller as the order  $J$  increases. A good choice of  $C_j$ 's leads to better accuracy for a smaller  $J$ , but reductions in spurious reflection can still be obtained with non-optimal  $C_j$ 's by simply increasing  $J$ .
- They are very general applying to a variety of wave problems in one, two, or three-dimensional configurations. Moreover, they can be used for wave problems in dispersive and stratified media.

To discover the motivation for the form introduced above (III.4), consider a possible solution to the semi-infinite wave guide program suggested by (II.90):

$$\eta = AY_n(y) \exp[ik(x - C_x t + \varphi)], \quad (\text{III.5})$$

where  $A$  is the wave amplitude,  $\varphi$  is the phase,  $k$  is the  $x$ -component wave number,  $\omega$  is the wave frequency, and  $C_x = \frac{\omega}{k}$  is the phase velocity.  $Y_n(y)$  is determined from the dependency of  $C_0$  and  $f$  on  $y$ . Recall from the Klein Gordon equation derivation that  $C_0 = gH_0$ , where  $H_0(x, y)$  is described in Figure 8. Since this analysis assumes a flat bottom,  $H_0$ , and therefore  $C_0$ , is constant. Also recall that  $f$ , the dispersion or Coriolis parameter, varied with the latitude  $\phi$  (II.43). With respect to the Earth model (Figure 2),  $\phi$  was determined to be a function of  $y$  only. Therefore, in the shallow water model,  $f$  is a function of  $y$  only. Now consider the real part of (III.5):

$$\eta = AY_n(y) \cos[k(x - C_x t + \varphi)]. \quad (\text{III.6})$$

Substitution into (III.4) generates:

$$AY_n(y)k \sin[k(x - C_x t + \varphi)] \left[ \prod_{j=1}^J (C_x - C_j) \right] = 0, \quad (\text{III.7})$$

which implies:

$$\prod_{j=1}^J (C_x - C_j) = 0. \quad (\text{III.8})$$

Thus the Higdon NRBC is exact (e.g. no portion of the wave is reflected) at  $\Gamma_E$  if the phase speed  $C_x$  matches any of the chosen Higdon parameters  $C_j$ .

Typically solutions to the Klein-Gordon equation consist of an infinite number of waves, whereas, we are limited to the selection of a finite number of parameters. Therefore, in most cases  $C_x \neq C_j$ . We can still validate (III.8) by assuming that the impinging wave splits at  $\Gamma_E$  into a reflected and passing wave. The magnitude of the reflected wave is easily analyzed. Consider a simplified form of (III.6) in which  $Y_n(y) = 1$  and  $\varphi = 0$ :

$$\eta = A \cos[k(x - C_x t)], \quad (\text{III.9})$$

and a first-order Higdon NRBC:

$$\left(\frac{\partial}{\partial t} + C_j \frac{\partial}{\partial x}\right) \eta = 0, \quad (\text{III.10})$$

where  $C_x \neq C_j$ . The original wave impinging on  $\Gamma_E$  is the sum of the wave that passes through  $\Gamma_E$  and the wave that reflects back into the domain. Mathematically stated:

$$A \cos[k(x - C_x t)] = A_r \cos[-k(x + C_x t)] + A_p \cos[k(x - C_x t)]. \quad (\text{III.11})$$

where  $A_r$  and  $A_p$  are the amplitudes of the reflected and passing waves respectively. Note that reflection affects the wave by reversing its direction of travel, or mathematically by reversing the sign of the wave number  $k$ . The wave frequency  $\omega$  for the reflected wave remains unchanged. If any reflection occurs, then  $0 < |A_r| < |A|$ . With regards to the passing wave, the wave number  $k$  and phase speed  $C_x$  remain unchanged. However,  $|A_p|$  will be reduced with respect to  $|A|$ . Substituting the right-hand side of (III.11) into (III.10) yields:

$$A_r(C_x + C_j) - A_p(C_x - C_j) = 0. \quad (\text{III.12})$$

Using this equation we define the *reflection coefficient*  $R$  for a first-order Higdon NRBC to be:

$$R = \left| \frac{A_r}{A_p} \right| = \left| \frac{C_j - C_x}{C_j + C_x} \right|. \quad (\text{III.13})$$

This yields:

$$|A_r| = \frac{R}{1+R} |A| \quad \text{and} \quad |A_p| = \frac{1}{1+R} |A|. \quad (\text{III.14})$$

We see from (III.13) and (III.14) that  $|A_r| < |A_p|$  when  $C_x \neq 0$ . Note that  $R \rightarrow 1$  as  $C_x \rightarrow 0$  implying that waves with low phase speeds will result in maximum reflection of  $|A_r| = |A_p| = .5|A|$  at the artificial boundary. This circumstance is mitigated in that these same low-speed waves reach the boundary at times that are often outside the scope of the problem.

The reflection coefficient for a  $J^{\text{th}}$ -order Higdon NRBC is easily derived using the above techniques:

$$R = \prod_{j=1}^J \left| \frac{C_j - C_x}{C_j + C_x} \right|. \quad (\text{III.15})$$

This expression represents the product of  $J$  factors that are less than one. Hence simply increasing the order  $J$  reduces the amplitude of the reflecting wave. Theoretically, one could reduce the amplitude of the reflected wave at  $\Gamma_E$  to zero without regard for the value of  $C_j$  by letting  $J \rightarrow \infty$ . Practically, however, we are limited by computer capability. We can only select a finite number of  $C_j$ 's and therefore must tolerate some spurious reflection. Fortunately,  $R$  can be reduced significantly by intelligently selecting  $C_j$ 's. Strategies for this are discussed in the next section.

### C. DETERMINING OPTIMAL VALUES FOR THE HIGDON PARAMETERS

Existing literature offers no analytical means to optimize the value of the Higdon parameters  $C_j$  for a dispersive wave. Three general methods have been suggested: (1) a-priori selection, (2) computer automated selection, and (3) dynamic selection. The first two methods are explored in this section.

The first general method was suggested by Higdon (see e.g. [Ref. 17] - [Ref. 21]) and selects  $C_j$ 's using an "educated guess". One takes advantage of the properties of the reflection coefficient  $R$  and parameters of the Klein-Gordon equation to accomplish this. A second general method chooses  $C_j$ 's automatically by computer code as a preprocess. These methods typically use information about the interior wave to select  $C_j$ 's that minimize reflection. Givoli and Neta suggest a simple approach in which  $C_j$ 's are determined from wave numbers that are evenly distributed over the span of maximum resolvable wave numbers. In another approach they recommend using the minimax method to pick  $k$  values [Ref. 24]. To test these methods, the "oscilloscope" method is developed to fine tune the  $C_j$ 's and minimize the reflection of a known wave. Theoretically, this procedure produces the best result, but it is too

expensive computationally to serve as a preprocess. It is, however, a useful measure of the effectiveness of other suggested methods.

To quantitatively compare the different schemes, several numerical experiments are conducted for a semi-infinite one-dimensional domain  $[0, \infty)$  on the  $x$ -axis. This domain allows waves to travel in the  $x$ -direction only, eliminating a need to consider geometric dispersion which occurs in the semi-infinite channel. It also allows us to determine analytically the effects of Higdon parameters  $C_j$  on the reflection coefficient  $R$ . The waves in the domain are governed by the one-dimensional homogeneous Klein-Gordon equation:

$$\frac{\partial^2 \eta}{\partial t^2} - C_0^2 \frac{\partial^2 \eta}{\partial x^2} + f^2 \eta = 0, \quad (\text{III.16})$$

An artificial boundary  $\Gamma_E$  is placed at  $4\pi$ . A continuous wave is assumed to exist inside the truncated domain with the following initial conditions:

$$\eta(x, 0) = \sum_{k=1}^{75} \frac{1}{k^2} \cos(kx) \quad \text{and} \quad \eta_t(x, 0) = 0. \quad (\text{III.17})$$

The solution is assumed to be of the form:

$$\eta(x, t) = \sum_{k=1}^{75} A_k \cos(kx - \omega t), \quad (\text{III.18})$$

where the dispersion relation:

$$\omega^2 = C_0^2 k^2 + f^2 \quad (\text{III.19})$$

is necessary to satisfy (III.16). Substituting (III.19) into (III.18) yields:

$$\eta(x, t) = \sum_{k=1}^{75} \frac{1}{k^2} \cos\left(kx - \sqrt{C_0^2 k^2 + f^2} t\right). \quad (\text{III.20})$$

The resulting dispersive wave is somewhat contrived since the number of wave numbers  $k$  is finite. However, it serves for the current purpose to analyze various schemes to select Higdon parameters. Rewriting (III.20) generates:

$$\eta(x, t) = \sum_{k=1}^{75} \frac{1}{k^2} \cos[k(x - C_k t)], \quad (\text{III.21})$$

where:

$$C_k = \frac{\omega}{k} = \frac{\sqrt{C_0^2 k^2 + f^2}}{k}. \quad (\text{III.22})$$

Note that  $C_k \geq C_0$ , a fact that is important later when estimating  $C_j$ 's. Equation (III.21) is used to determine the reflection coefficient  $R$ :

$$R = \left| \frac{A_r}{A_p} \right| = \prod_{j=1}^J \left| \frac{C_j - C_k}{C_j + C_k} \right| = \prod_{j=1}^J \left| \frac{kC_j - \sqrt{C_0^2 k^2 + f^2}}{kC_j + \sqrt{C_0^2 k^2 + f^2}} \right|. \quad (\text{III.23})$$

Thus the equation for the reflected wave is:

$$\sum_{k=1}^{75} \frac{1}{k^2} \left( \frac{R}{R+1} \right) \cos(-kx - \sqrt{C_0^2 k^2 + f^2} t), \quad (\text{III.24})$$

which can be use to determine the error  $\|e(t)\|$  resulting from a specified Higdon NRBC. Note that, by (III.23),  $R$  is a function of  $k$  and must appear inside the summation. We calculate the error by taking the norm of the reflected wave from 0 to  $\Gamma_E$ . Since the experimental data is discrete, the equation for the 2-norm of the reflected wave at time  $t$  is:

$$\|e(t)\| = \sum_{i=1}^{N_x} \sqrt{\frac{\eta_R(x_i, t)}{N_x}}, \quad (\text{III.25})$$

where  $N_x$ , the number of elements in the  $x$ -vector, is determined by the refinement of the grid. In each experiment we set  $C_0 = 2$  and  $f = 1$ . The error measurement is taken at time  $t = 100$  time units.

### 1. Experiment One: $C_j = C_0$

In the first experiment, we disregard the wave generated inside the domain and offer our best guess for determining  $C_j$ 's. As shown by (III.22),  $C_k \geq C_0$ . Furthermore, from (III.23), we see that for  $|C_0 k| \gg |f|$ ,

$$R \rightarrow \prod_{j=1}^J \left| \frac{C_j - C_0}{C_j + C_0} \right|. \quad (\text{III.26})$$

It is therefore logical to let  $C_j = C_0$  for  $j = 1 \dots J$ . For a first order Higdon NRBC ( $H_1$ ), this is equivalent to the Sommerfeld condition which is utilized widely



in meteorology [Ref. 24]. By simply increasing the order  $J$  of the Higdon NRBC, (III.15) revealed that the reflection coefficient  $R$  is reduced. When we let  $C_0=2$  and  $f=1$ , our example wave (III.20) becomes:

$$\eta(x, t) = \sum_{k=1}^{75} \frac{1}{k^2} \cos(kx - \sqrt{4k^2 + 1} t). \quad (\text{III.27})$$

The  $J^{\text{th}}$ -order reflection coefficient (III.23) for this wave is:

$$R(k) = \prod_{j=1}^J \left| \frac{2k - \sqrt{4k^2 + 1}}{2k + \sqrt{4k^2 + 1}} \right| \quad (\text{III.28})$$

Using this equation we generate the reflected wave resulting from the boundary condition. Figure 10 (left) displays the reflected wave for a first-order ( $H_1$ ) through third-order ( $H_3$ ) Higdon NRBC. For  $H_4$  through  $H_9$  the amplitude of the reflected wave has decreased to the point that it is not visible unless a smaller scale is used. Figure 10 (right) displays the norms of the reflected waves, which are taken to be the measurement of error for the boundary condition. This figure quantifies the rapid drop off in the reflected or error norm for increasing  $J$ .

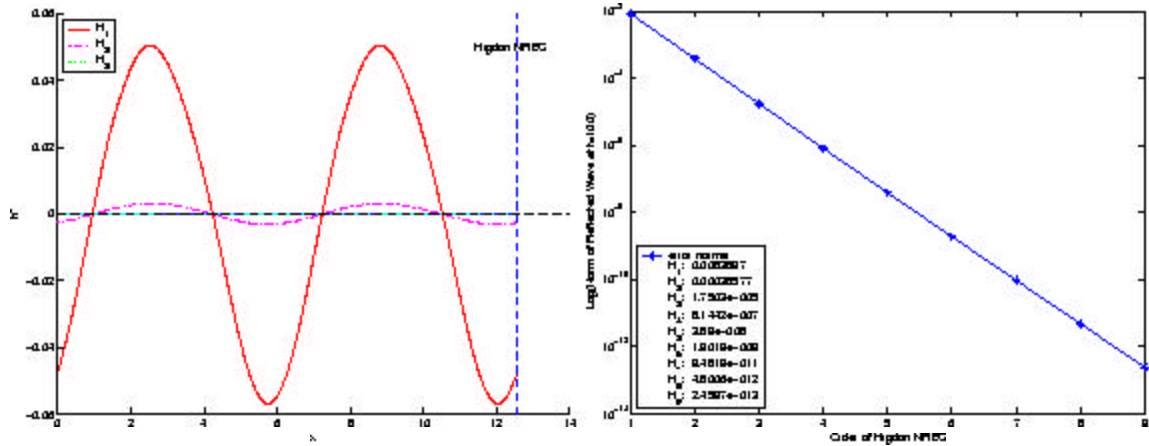


Figure 10. Left: Experiment 1a,  $\eta_R$  at  $t=100$ :  $C_j = C_0$  with  $C_0=2$  and  $f=1$  (Solid Line Depicts  $H_1$ . Dotted Line Depicts  $H_2$  Plot). Right:  $\|\eta_R\|$  at  $t=100$  for  $H_1$  through  $H_9$ .

We might refine this method even further by considering the following argument: Although (III.23) reveals  $C_j \rightarrow C_0$  as  $k$  gets large, (III.28) suggests that  $R$  is

small for large  $k$  anyway. Therefore by selecting  $C_j = C_0$ , we select Higdon coefficients that damp out waves that had a low reflection coefficient  $R$ , while waves with low wave numbers, and therefore higher reflection coefficients, are not considered in the estimation of  $C_j$ . Therefore, using (III.22), we consider:

$$C_j = \frac{\sqrt{C_0^2 k_{min}^2 + f^2}}{k_{min}}, \quad (\text{III.29})$$

where, from our experiment parameters,  $k_{min} = 1$ . For this example  $C_j = \sqrt{5}$ . Improved results are reported in Figure 11. However, one has presupposed some knowledge of the wave action inside the finite domain in order to estimate  $k_{min}$ .

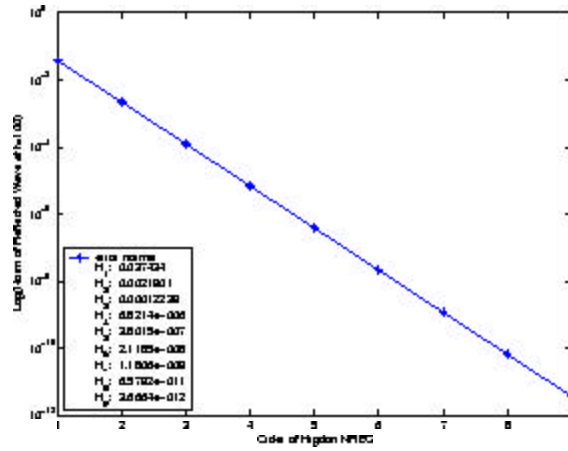


Figure 11.  $\|\eta_R\|$  at  $t=100$ :  $C_j = \frac{\sqrt{C_0^2 k_{min}^2 + f^2}}{k_{min}} = \sqrt{5}$  ( $C_0=2, f=1$ )

## 2. Experiment Two: $C_j$ Determined from Wave Numbers Distributed Evenly over $[k_{min}, k_{max}]$

In the second experiment, we selected  $C_j$ 's by evenly distributing wave numbers over the interval  $[k_{min}, k_{max}]$ . All other parameters used are the same as those used in the first experiment. Here,  $k_{min}$ , the minimum significant wave number, might be determined by some advanced knowledge of the internal wave, or by the time scale of the problem (e.g.  $k_{min}$  describes a wave that moves so slowly that it never reaches the boundary). For this experiment,  $k_{min} = 1$ . With regards to  $k_{max}$ , assuming 10

grid points per wave length are necessary to resolve any given wave, a reasonable estimate is:

$$k_{max} = \frac{\pi}{5\Delta x}, \quad (\text{III.30})$$

where  $\Delta x$  is the grid spacing. The  $k$  values are then given by:

$$k_{j_i} = k_{min} + \frac{i(k_{max} - k_{min})}{J - 1}, \quad i = 0, 1, \dots, J - 1 \quad (\text{III.31})$$

where  $J$  is the order of the Higdon NRBC and  $k_{j_i}$  is the  $i^{\text{th}}$   $k$ -value for a  $J^{\text{th}}$ -order boundary condition. Equation (III.30) suggests that  $k_{max} = 50$  for this experiment. After determining the  $k_j$ 's, we now use (III.22) to calculate the  $C_j$ 's:

$$C_{j_i} = \frac{\sqrt{C_0^2 k_{j_i}^2 + f^2}}{k_{j_i}}, \quad (\text{III.32})$$

where  $C_{j_i}$  is the  $i^{\text{th}}$  Higdon parameter for a  $J^{\text{th}}$ -order boundary condition. The resulting  $C_j$ 's for this experiment are:

$H_1$  : 2.2361  
 $H_2$  : 2.0001 2.2361  
 $H_3$  : 2.0001 2.0004 2.2361  
 $H_4$  : 2.0001 2.0002 2.0008 2.2361  
 $H_5$  : 2.0001 2.0002 2.0004 2.0014 2.2361  
 $H_6$  : 2.0001 2.0002 2.0003 2.0006 2.0021 2.2361  
 $H_7$  : 2.0001 2.0001 2.0002 2.0004 2.0008 2.0030 2.2361  
 $H_8$  : 2.0001 2.0001 2.0002 2.0003 2.0005 2.0011 2.0039 2.2361  
 $H_9$  : 2.0001 2.0001 2.0002 2.0002 2.0004 2.0007 2.0014 2.0049 2.2361

The error measurements are reported in Figure 12 and represent a significant improvement over those reported in the first experiment. We now seek to improve the estimation of  $C_j$ 's using a method suggested by Neta and Givoli [Ref. 24].

### 3. Experiment Three: Estimating $C_j$ 's from Wave Numbers Obtained using the Minimax Formula

The third experiment utilizes a method that computes  $C_j$ 's from wave numbers obtained using the minimax formula based on the Chebyshev polynomial, an

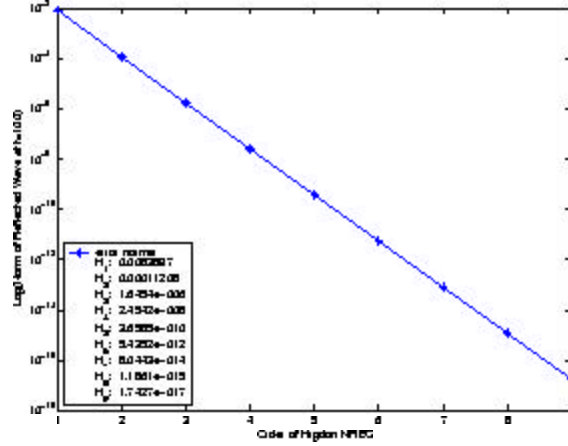


Figure 12. Experiment 2,  $\|\eta_R\|$  at  $t=100$ :  $C_j$  from  $k$  Evenly Distributed on  $[k_{min}, k_{max}]$  ( $C_0=2, f=1$ )

approach adopted by Neta and Givoli [Ref. 24]. We consider the method for the one-dimensional problem presented by the current experiment in which wave numbers are given by:

$$k_{j,i} = \sqrt{\frac{k_{max}^2}{2} \left[ 1 + \cos \left( \frac{(2i-1)}{2(j-1)} \pi \right) \right]}, \quad i = 1, 2, \dots, j-1, \quad (\text{III.33})$$

where  $k_{j,i}$  is the  $i^{\text{th}}$  wave number calculated for a  $j^{\text{th}}$ -order boundary condition. As before, the maximum resolvable wave number  $k_{max}$  equals 50. The Higdon parameters are calculated using (III.32). The  $J^{\text{th}}$  Higdon parameter  $C_j$  is set equal to  $C_0$ . The resulting Higdon parameters were:

$$\begin{aligned} H_1 &: 2 \\ H_2 &: 2 \quad 2.0002 \\ H_3 &: 2 \quad 2.0001 \quad 2.0007 \\ H_4 &: 2 \quad 2.0001 \quad 2.0002 \quad 2.0015 \\ H_5 &: 2 \quad 2.0001 \quad 2.0001 \quad 2.0003 \quad 2.0026 \\ H_6 &: 2 \quad 2.0001 \quad 2.0001 \quad 2.0002 \quad 2.0005 \quad 2.0041 \\ H_7 &: 2 \quad 2.0001 \quad 2.0001 \quad 2.0002 \quad 2.0003 \quad 2.0007 \quad 2.0059 \\ H_8 &: 2 \quad 2.0001 \quad 2.0001 \quad 2.0001 \quad 2.0002 \quad 2.0004 \quad 2.0009 \quad 2.0080 \\ H_9 &: 2 \quad 2.0001 \quad 2.0001 \quad 2.0001 \quad 2.0002 \quad 2.0002 \quad 2.0004 \quad 2.0012 \quad 2.0104 \end{aligned}$$

The error norms reported in Figure 13 (left) are not the predicted improvement over the results reported in the second experiment. However with a minor adjustment to the method, we can bring this about. Rather than setting  $C_j = C_0$ , we use (III.29) and let:

$$C_j = \frac{\sqrt{C_0^2 k_{min}^2 + f^2}}{k_{min}}.$$

The Higdon parameters are now shifted slightly as follows:

$H_1$  : 2.2361  
 $H_2$  : 2.0002 2.2361  
 $H_3$  : 2.0001 2.0007 2.2361  
 $H_4$  : 2.0001 2.0002 2.0015 2.2361  
 $H_5$  : 2.0001 2.0001 2.0003 2.0026 2.2361  
 $H_6$  : 2.0001 2.0001 2.0002 2.0005 2.0041 2.2361  
 $H_7$  : 2.0001 2.0001 2.0002 2.0003 2.0007 2.0059 2.2361  
 $H_8$  : 2.0001 2.0001 2.0001 2.0002 2.0004 2.0009 2.0080 2.2361  
 $H_9$  : 2.0001 2.0001 2.0001 2.0002 2.0002 2.0004 2.0012 2.0104 2.2361

The decrease in error measure reported in Figure 13 (right) indicates that though the change in the method is minor, the results are substantial and are a small improvement over the results of the second experiment. We now conduct a final experiment that will fine tune the results found in this experiment and minimize the reflected wave.

#### 4. Experiment Four: A Procedure for Optimizing $C_j$ 's

The fourth experiment utilizes a procedure for optimizing  $C_j$ 's that can be utilized if an exact solution is known. It is computationally intensive, but provides a quantitative comparison for the methods introduced thus far. Imagine the Higdon parameters  $C_j$  to be controlled by the dials on an oscilloscope. A boundary condition of order  $J$  is represented by  $J$  dials. The screen on of the oscilloscope represents the finite domain and displays the reflected wave. An experimenter adjusts the first dial up or down in order to reduce the size of the reflected wave. He continues his



Higdon parameters were:

$H_1$  : 2.2229  
 $H_2$  : 2.0481 2.2359  
 $H_3$  : 2.0170 2.0607 2.2361  
 $H_4$  : 2.0075 2.0260 2.0615 2.2361  
 $H_5$  : 2.0038 2.0135 2.0275 2.0615 2.2361  
 $H_6$  : 2.0031 2.0116 2.0206 2.0278 2.0616 2.2361  
 $H_7$  : 2.0021 2.0075 2.0151 2.0276 2.0608 2.0615 2.2361  
 $H_8$  : 2.0012 2.0047 2.0094 2.0156 2.0276 2.0615 2.0615 2.2361  
 $H_9$  : 2.0010 2.0037 2.0075 2.0106 2.0156 2.0276 2.0615 2.0616 2.2361

The error measurements reported in Figure 14 show a significant decrease when compared to those generated by the modified minimax method. Clearly the “oscilloscope” procedure was effective in substantially reducing the magnitude of the reflected wave. It is also interesting to note that the maximum  $C_j$  for  $H_3$  through  $H_9$  is based on  $k_{min}$  which is 1 in this experiment. This has the effect of allowing the wave with the smallest wave number to pass through the boundary unhindered. This is significant because this wave has largest reflection. We can obtain the remaining wave numbers that pass without reflection at the boundary using the above  $C_j$ ’s. These are calculated as follows:

$$k_{ji} = \sqrt{\frac{f^2}{C_{ji}^2 - C_0^2}}. \quad (\text{III.34})$$

Using this formula, the resulting  $k_J$ 's from the oscilloscope procedure are:

$H_1$ :	1.0308								
$H_2$ :	2.2662	1.0004							
$H_3$ :	3.8287	2.0139	1						
$H_4$ :	5.7711	3.0908	2.0008	1					
$H_5$ :	8.0799	4.2890	3.3035	2.0008	1				
$H_6$ :	9.0027	4.6387	3.4745	2.9870	1.9992	1			
$H_7$ :	11.011	5.7748	4.0590	3.0010	2.0132	2.0008	1		
$H_8$ :	14.333	7.3193	5.1511	4.0014	2.9986	2.0009	2.0002	1	
$H_9$ :	15.918	8.1628	5.7489	4.8542	3.9942	3.0011	2.0004	1.9992	1

This information by itself is uninteresting, but is useful when compared to the  $k_J$ 's obtained by the modified minimax method which were:

$H_1$ :	1								
$H_2$ :	35.355	1							
$H_3$ :	46.794	19.134	1						
$H_4$ :	48.296	35.355	12.941	1					
$H_5$ :	49.039	41.574	27.779	9.7545	1				
$H_6$ :	49.384	44.550	35.355	22.700	7.8217	1			
$H_7$ :	49.572	46.194	39.668	30.438	19.134	6.5263	1		
$H_8$ :	49.686	47.194	42.336	35.355	26.602	16.514	5.5982	1	
$H_9$ :	49.759	47.847	44.096	38.651	31.720	23.570	14.5142	4.9009	1

These results indicate that:

- It is more effective to select  $C_j$ 's that correspond to lower wave numbers.
- The span of wave numbers generated by the minimax method is much greater than the optimized span indicated by the "oscilloscope" procedure.
- The wave numbers inside the minimax span increase too quickly when compared to the optimal span.



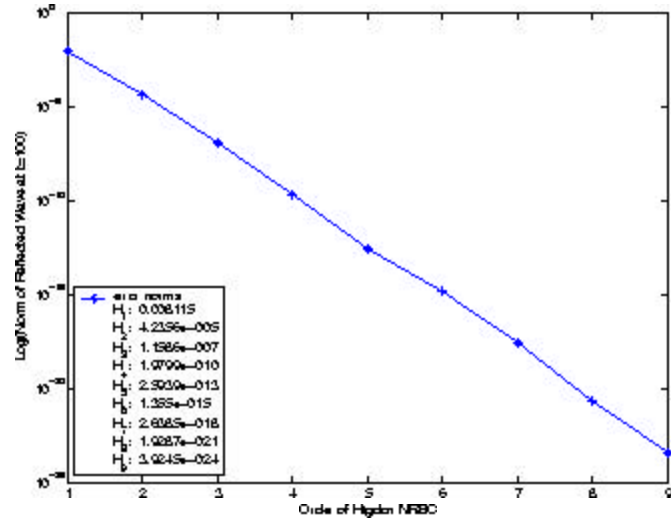


Figure 14. Experiment 4,  $\|\eta_R\|$  at  $t=100$ :  $C_j$  Optimized using Oscilloscope Procedure

In the next chapter we explore the properties of the Higdon NRBC with respect to the two-dimensional infinite wave guide.

THIS PAGE INTENTIONALLY LEFT BLANK

## IV. DISCRETIZING THE SEMI-INFINITE WAVE GUIDE PROBLEM WITH ARTIFICIAL BOUNDARIES

In this section we discretize the Klein-Gordon equation. We also derive two forms of the discrete Higdon NRBC using the two- and three-point backward-difference equations for the first-order derivative. A scheme proposed by Givoli and Neta [Ref. 22] is used to simplify this step. We then compare the two Higdon forms, as well as previously discussed schemes for selecting  $C_j$ , via numerical example. We accomplish this by numerically solving the semi-infinite wave guide problem (Figure 9). A spatial grid for  $x$  and  $y$  and a temporal grid for  $t$  is set up and the  $\eta$  value at a point  $(x_p, y_q)$  at time  $t = t_n$  is denoted by:

$$\eta_{p,q}^n = \eta(x_p, y_q, t_n). \quad (\text{IV.1})$$

The  $\eta$  values of the wave guide's interior points are determined using the discrete Klein-Gordon equation. We then obtain  $\eta$  values on the north and south boundaries. Neumann conditions are imposed here and discretization schemes are required. Finally, the  $\eta$  values on the east boundary are determined using the discrete form of the Higdon NRBC.

### A. DISCRETIZING THE KLEIN-GORDON EQUATION

The homogeneous linearized shallow water *with zero mean* or Klein-Gordon equation is given by (II.88):

$$\frac{\partial^2 \eta}{\partial t^2} - C_0^2 \nabla^2 \eta + f^2 \eta = 0.$$

Higdon proved that in the context of the scalar Klein-Gordon equation, discrete Higdon NRBC's are stable if such a standard second-order central-difference scheme is used to discretize (V.19) [Ref. 21]. Thus we use the following approximation for the

second derivative:

$$F''(x_0) = \frac{1}{h^2} [F(x_0 - h) - 2F(x_0) + F(x_0 + h)] + O(h^2), \quad (\text{IV.2})$$

where  $h$  is the grid size and  $O(h^2)$  is an approximation error of order  $h^2$ . We approximate the Klein-Gordon equation by:

$$\begin{aligned} \frac{1}{(\Delta t)^2} (\eta_{p,q}^{n-1} - 2\eta_{p,q}^n + \eta_{p,q}^{n+1}) - \left( \frac{C_0}{\Delta x} \right)^2 (\eta_{p-1,q}^n - 2\eta_{p,q}^n + \eta_{p+1,q}^n) \\ - \left( \frac{C_0}{\Delta y} \right)^2 (\eta_{p,q-1}^n - 2\eta_{p,q}^n + \eta_{p,q+1}^n) + f^2 \eta_{p,q}^n = 0. \end{aligned} \quad (\text{IV.3})$$

Solving for  $\eta_{p,q}^{n+1}$  gives:

$$\begin{aligned} \eta_{p,q}^{n+1} = & \left( \frac{C_0 \Delta t}{\Delta x} \right)^2 (\eta_{p-1,q}^n - 2\eta_{p,q}^n + \eta_{p+1,q}^n) \\ & + \left( \frac{C_0 \Delta t}{\Delta y} \right)^2 (\eta_{p,q-1}^n - 2\eta_{p,q}^n + \eta_{p,q+1}^n) + [2 - (f \Delta t)^2] \eta_{p,q}^n - \eta_{p,q}^{n-1}. \end{aligned}$$

(IV.4)

We use this equation to approximate the interior points of the domain. The approximation error is of order  $O(\Delta x^2, \Delta y^2, \Delta t^2)$ . Note that the scheme is two level in time and thus one requires an additional starting value. This can be accomplished using the Matsuno scheme [Ref. 33].

## B. DISCRETIZING THE NORTH AND SOUTH BOUNDARIES

If the conditions on the north and south boundaries contain derivatives, then they too must be discretized. For example, consider the Neumann type condition:

$$\frac{\partial \eta}{\partial y} = 0,$$

The south boundary is discretized by using a three-point forward-difference formula for  $F'(x_0)$ :

$$F'(x_0) = \frac{1}{2h} [-3F(x_0) + 4F(x_0 + h) - F(x_0 + 2h) + O(h^2)]. \quad (\text{IV.5})$$

Thus the south boundary condition is approximated by:

$$\frac{\partial \eta}{\partial y} = \frac{1}{2\Delta y} [-3\eta_{p,S}^n + 4\eta_{p,S+1}^n - \eta_{p,S+2}^n] + O(\Delta y^2) = 0, \quad (\text{IV.6})$$

where  $S$  is the  $y$ -index marking the south boundary,  $\Delta y$  is the size of the  $y$ -grid, and  $O(\Delta y^2)$  is an approximation error of order  $\Delta y^2$ . We now approximate  $\eta$  on the south boundary:

$$\eta_{p,S}^n = \frac{4}{3}\eta_{p,S+1}^n - \frac{1}{3}\eta_{p,S+2}^n. \quad (\text{IV.7})$$

Similarly on the north boundary, three-point backward-difference formula for  $F'(x_0)$ , an approximation of order  $\Delta y^2$  for  $\eta$  is:

$$\eta_{p,N}^n = \frac{4}{3}\eta_{p,N-1}^n - \frac{1}{3}\eta_{p,N-2}^n, \quad (\text{IV.8})$$

where  $N$  is the  $y$ -index marking the north boundary.

### C. THE DISCRETE FORM OF THE HIGDON NRBC

The  $J^{\text{th}}$ -order Higdon NRBC  $H_J$  (III.4) is the product of  $J$  operators:

$$\prod_{j=1}^J \left( \frac{\partial}{\partial t} + C_j \frac{\partial}{\partial x} \right) \eta = 0. \quad (\text{IV.9})$$

To discretize this equation, use the two-point backward-difference formula for the first derivative:

$$F'(x_0) = \frac{1}{h} [F(x_0) - F(x_0 - h)] + O(h), \quad (\text{IV.10})$$

where  $O(h)$  is an approximation error of order  $h$ . The discrete form of (IV.9) becomes:

$$\begin{aligned} \prod_{j=1}^J \left[ \left( \frac{\eta(x, y, t) - \eta(x, y, t - \Delta t)}{\Delta t} \right) \right. \\ \left. + C_j \left( \frac{\eta(x, y, t) - \eta(x - \Delta x, y, t)}{\Delta x} \right) \right] = 0. \end{aligned} \quad (\text{IV.11})$$

The approximation error for this equation is of order  $O(\Delta x, \Delta t)$ .

Two special operators are defined to further facilitate the discussion. The temporal shift operator, denoted by  $S_t^-$ , affects a grid point as follows:

$$S_t^- \eta_{p,q}^n = \eta_{p,q}^{n-1} = \eta(x_p, y_q, t_n - \Delta t). \quad (\text{IV.12})$$

Similarly, the spatial shift operator in the  $x$ -direction, denoted by  $S_x^-$ , affects a grid point as follows:

$$S_x^- \eta_{p,q}^n = \eta_{p-1,q}^n = \eta(x_p - \Delta x, y_q, t_n). \quad (\text{IV.13})$$

The identity operator, denoted by  $I$ , has no effect when operating on the grid point, e.g.  $I \eta_{pq}^n = \eta_{pq}^n$ . Using these operators, the discrete form of the Higdon NRBC is:

$$\prod_{j=1}^J \left[ \frac{I - S_t^-}{\Delta t} + C_j \left( \frac{I - S_x^-}{\Delta x} \right) \right] \eta_{E,q}^n = 0, \quad (\text{IV.14})$$

where the index  $E$  corresponds to the location of the Higdon NRBC at  $x = x_E$ . By collecting the operator terms  $I$ ,  $S_t^-$ , and  $S_x^-$ , (IV.14) can be rewritten as:

$$\prod_{j=1}^J \left[ \left( 1 + C_j \frac{\Delta t}{\Delta x} \right) I - S_t^- - \left( C_j \frac{\Delta t}{\Delta x} \right) S_x^- \right] \eta_{E,q}^n = 0. \quad (\text{IV.15})$$

Making the following substitutions:

$$a_j = 1 + C_j \frac{\Delta t}{\Delta x}, \quad d_j = -1, \quad \text{and} \quad e_j = -C_j \frac{\Delta t}{\Delta x}, \quad (\text{IV.16})$$

allows us to rewrite (IV.15) as:

$$\prod_{j=1}^J \left( a_j I + d_j S_t^- + e_j S_x^- \right) \eta_{E,q}^n = 0. \quad (\text{IV.17})$$

Now consider a second order Higdon NRBC  $H_2$ , which by using (IV.17) and expanding can be written as:

$$\begin{aligned} & [a_1 a_2 I^2 + a_1 d_2 I S_t^- + a_1 e_2 I S_x^- + d_1 a_2 I S_t^- + d_1 d_2 S_t^{-2} \\ & + d_1 e_2 S_t^- S_x^- + e_1 a_2 I S_x^- + e_1 d_2 S_t^- S_x^- + e_1 e_2 S_x^{-2}] \eta_{E,q}^n = 0. \end{aligned} \quad (\text{IV.18})$$

In this form,  $H_J$  is represented as the summation of  $3^J$  terms:

$$\sum_{m=0}^{3^J-1} A_m P_m \eta_{E,q}^n = 0, \quad (\text{IV.19})$$

where  $A_m$  is a product of  $a_j$ ,  $d_j$  and/or  $e_j$ , and  $P_m$  is made up of a combination of operators  $I$ ,  $S_t^-$  and/or  $S_x^-$ . The first term of (IV.17) is:

$$a_1 a_2 I^2 \eta_{E,q}^n = \left( \prod_{j=1}^J a_j \right) \eta_{E,q}^n. \quad (\text{IV.20})$$

By letting:

$$A_0 = \prod_{i=1}^J a_i \quad \text{and} \quad Z^* = \sum_{m=1}^{3^J-1} A_m P_m \eta_{E,q}^n, \quad (\text{IV.21})$$

we can rewrite (IV.19) as:

$$A_0 \eta_{E,q}^n + Z^* \eta_{E,q}^n = 0. \quad (\text{IV.22})$$

Since  $A_0 \neq 0$ , this implies:

$$\eta_{E,q}^n = \frac{-Z^* \eta_{E,q}^n}{A_0}. \quad (\text{IV.23})$$

The problem now is to evaluate  $Z^*$ .

We now employ the scheme devised by Givoli and Neta [Ref. 22]. Consider the coefficient  $A_m$  and the operator  $P_m$ . We rewrite the index  $m$  in base 3 and refer to it as  $m_{(3)}$ . Table II summarizes  $A_{m_{(3)}}$  and  $P_{m_{(3)}}$  and their corresponding values for the discrete form of  $H_2$  described by (IV.18). Inspection of the table reveals a useful

Table II.  $H_2$  Values for  $A_{m_{(3)}}$  and  $P_{m_{(3)}}$

$A_0 \rightarrow A_{00_{(3)}} = a_1 a_2$	$P_0 \rightarrow P_{00_{(3)}} = I^2$	$P_{00_{(3)}} \eta_{E,q}^n = \eta_{E,q}^n$
$A_1 \rightarrow A_{01_{(3)}} = a_1 d_2$	$P_1 \rightarrow P_{01_{(3)}} = I S_t^-$	$P_{01_{(3)}} \eta_{E,q}^n = \eta_{E,q}^{n-1}$
$A_2 \rightarrow A_{02_{(3)}} = a_1 e_2$	$P_2 \rightarrow P_{02_{(3)}} = I S_x^-$	$P_{02_{(3)}} \eta_{E,q}^n = \eta_{E-1,q}^n$
$A_3 \rightarrow A_{10_{(3)}} = d_1 a_2$	$P_3 \rightarrow P_{10_{(3)}} = S_t^- I$	$P_{10_{(3)}} \eta_{E,q}^n = \eta_{E,q}^{n-1}$
$A_4 \rightarrow A_{11_{(3)}} = d_1 d_2$	$P_4 \rightarrow P_{11_{(3)}} = (S_t^-)^2$	$P_{11_{(3)}} \eta_{E,q}^n = \eta_{E,q}^{n-2}$
$A_5 \rightarrow A_{12_{(3)}} = d_1 e_2$	$P_5 \rightarrow P_{12_{(3)}} = S_t^- S_x^-$	$P_{12_{(3)}} \eta_{E,q}^n = \eta_{E-1,q}^{n-1}$
$A_6 \rightarrow A_{20_{(3)}} = e_1 a_2$	$P_6 \rightarrow P_{20_{(3)}} = S_x^- I$	$P_{20_{(3)}} \eta_{E,q}^n = \eta_{E-1,q}^n$
$A_7 \rightarrow A_{21_{(3)}} = e_1 d_2$	$P_7 \rightarrow P_{21_{(3)}} = S_x^- S_t^-$	$P_{21_{(3)}} \eta_{E,q}^n = \eta_{E-1,q}^{n-1}$
$A_8 \rightarrow A_{22_{(3)}} = e_1 e_2$	$P_8 \rightarrow P_{22_{(3)}} = (S_x^-)^2$	$P_{22_{(3)}} \eta_{E,q}^n = \eta_{E-2,q}^n$

pattern that allows us to quickly generate the discrete form of  $H_J$  for any order  $J$ .

With regards to the index  $m_{(3)}$ , a digit value of 0, 1, or 2 implies that the coefficients

Table III. Constructing  $P_m$  and  $A_m$  from the Base Three Index  $0221_{(3)}$

Digit Position	1	2	3	4
Digit Value	0	2	2	1
Use Digit Value to Select Constant	$a_j$	$e_j$	$e_j$	$d_j$
Use Digit Position to Set Constant's Subscript	$a_1$	$e_2$	$e_3$	$d_4$
Use Digit Value to Select Operator	$I$	$S_x^{-1}$	$S_x^{-1}$	$S_t^{-1}$

$a_j$ ,  $d_j$ , or  $e_j$  respectively are part of the product that make up  $A_{m_{(3)}}$ . The position of the digit determines the index  $j$  for each term, where we consider the left most digit to be in position 1. Similarly, the digits 0, 1, and 2 imply the application of the  $I$ ,  $S_t^-$ , or  $S_x^-$  operator respectively in the construction of  $P_{m_{(3)}}$ . For example,  $H_4$  has 81 terms. The index for the 25<sup>th</sup> term has a base 3 equivalent equal to  $0221_{(3)}$  (note that  $J$  digits are always used for  $H_J$ ). Table III summarizes the application of the base three index  $0221_{(3)}$  to construct  $A_m$  and  $P_m$ . Therefore:

$$A_{25} \rightarrow A_{0221_{(3)}} = a_1 e_2 e_3 d_4 \text{ and } P_{25} \rightarrow P_{0221_{(3)}} = I(S_x^-)^2 S_t^-,$$

and:

$$A_{25} P_{25} \eta_{E,q}^n = a_1 e_2 e_3 d_4 \eta_{E-2,q}^{n-1}$$

We can further generalize the operator equation as follows:

$$P_{m_{(3)}} \eta_{E,q}^n = \eta_{E-b,q}^{n-a}, \quad (\text{IV.24})$$

where  $a$  and  $b$  are the number of times that the digits 1 and 2 appear respectively in  $m_{(3)}$ .

Thus far we have indicated that this scheme will generate  $3^J$  terms, but this number is reduced considerably when one combines terms containing the same operator. For example, in Table II the operators  $IS_t^-$ ,  $IS_x^-$ , and  $S_x^- S_t^-$  appear twice. When combined, the number of terms for the discretized form of  $H_2$  is reduced by three. In



general, terms will contain operators of the form  $S_x^{-a} S_t^{-b}$  where  $0 \leq a + b \leq J$ . The number of integer combinations of  $a$  and  $b$  that satisfy the inequality is:

$$\sum_{j=1}^{J+1} j = \frac{(J+2)(J+1)}{2}, \quad (\text{IV.25})$$

and represents the number of different operator possibilities for  $H_J$ . This is significant, because it greatly reduces storage requirements as well as processing time when using higher order Higdon NRBC's. For example,  $H_9$  is fully discretized using 55 vice 19,683 ( $3^9$ ) terms.

## D. IMPROVED FORM FOR THE DISCRETE HIGDON NRBC

In the previous section, we formulated a discrete form of the Higdon NRBC with an approximation error of order  $O(h)$ . The approximation error for the discretized Klein-Gordon equation and for the north/south boundaries were of order  $O(h^2)$ . This suggests that we might improve our scheme for discretizing the Higdon NRBC by using the three-point backward-difference formula which is given by:

$$F'(x_0) = \frac{1}{2h} [3F(x_0) - 4F(x_0 - h) + F(x_0 - 2h)] + O(h^2), \quad (\text{IV.26})$$

Using this in operator notation, the improved discrete form of the Higdon NRBC is:

$$\prod_{j=1}^J \left[ \frac{3I - 4S_t^- + S_t^{-2}}{\Delta t} + C_j \left( \frac{3I - 4S_x^- + S_x^{-2}}{\Delta x} \right) \right] \eta_{E,q}^n = 0. \quad (\text{IV.27})$$

Collecting the operator terms  $I$ ,  $S_t^-$ , and  $S_x^-$ , (IV.27) can be rewritten as:

$$\prod_{j=1}^J \left[ \left( 1 + C_j \frac{\Delta t}{\Delta x} \right) I - \frac{4}{3} S_t^- + \frac{1}{3} S_t^{-2} - \frac{4}{3} C_j \frac{\Delta t}{\Delta x} S_x^- + \frac{1}{3} C_j \frac{\Delta t}{\Delta x} S_x^{-2} \right] \eta_{E,q}^n = 0. \quad (\text{IV.28})$$

Making the following substitutions:

$$a_j = 1 + C_j \frac{\Delta t}{\Delta x}, \quad b_j = -\frac{4}{3}, \quad c_j = \frac{1}{3}, \quad d_j = -\frac{4}{3} C_j \frac{\Delta t}{\Delta x}, \quad \text{and} \quad e_j = \frac{1}{3} C_j \frac{\Delta t}{\Delta x}, \quad (\text{IV.29})$$

allows us to rewrite (IV.28) as:

$$\prod_{j=1}^J \left( a_j I + b_j S_t^- + c_j S_t^{-2} + d_j S_x^- + e_j S_x^{-2} \right) \eta_{E,q}^n = 0. \quad (\text{IV.30})$$

In the expanded form,  $H_J$  is represented as the summation of  $5^J$  terms:

$$\sum_{m=0}^{5^J-1} A_m P_m \eta_{E,q}^n = 0, \quad (\text{IV.31})$$

where  $A_m$  is a product of  $a_j$ ,  $b_j$ ,  $c_j$ ,  $d_j$ , and/or  $e_j$ . Similarly  $P_m$  is made up of a combination of operators  $I$ ,  $S_t^-$ ,  $S_t^{-2}$ ,  $S_x^-$  and/or  $S_x^{-2}$ . By letting:

$$A_0 = \prod_{i=1}^J a_i \quad \text{and} \quad Z^* = \sum_{m=1}^{5^J-1} A_m P_m \eta_{E,q}^n, \quad (\text{IV.32})$$

and noting that  $A_0 \neq 0$  we rewrite (IV.31) as:

$$\eta_{E,q}^n = \frac{-Z^* \eta_{E,q}^n}{A_0}. \quad (\text{IV.33})$$

Using a procedure similar to that employed by Givoli and Neta [Ref. 22], we can easily sift through the algebraic complexities of (IV.33).

Consider again the coefficient  $A_m$  and the operator  $P_m$ . We rewrite the index  $m$  in base 5 which we will refer to as  $m_{(5)}$ . With regards to this index, a digit value of 0, 1, 2, 3, and 4 implies that the coefficients  $a_j$ ,  $b_j$ ,  $c_j$ ,  $d_j$ , or  $e_j$  respectively are part of the product that makes up  $A_{m_{(5)}}$ . The position of the digit determines the index  $j$  for each term, where the left most digit is in position 1. Similarly, the digits 0, 1, 2, 3, and 4 imply the application of the  $I$ ,  $S_t^-$ ,  $S_t^{-2}$ ,  $S_x^-$ , or  $S_x^{-2}$  operator respectively in the construction of  $P_{m_{(5)}}$ . For example,  $H_5$  has 3125 terms. The index of the 1454<sup>th</sup> term has a base 5 equivalent of 21304<sub>(5)</sub>. Therefore:

$$A_{1454} = c_1 b_2 d_3 a_4 e_5 \quad \text{and} \quad P_{1454} = S_t^{-3} S_x^{-3},$$

and:

$$A_{1454} P_{1454} \eta_{E,q}^n = c_1 b_2 d_3 a_4 e_5 \eta_{E-3,q}^{n-3}.$$

We have indicated that this scheme will generate  $5^J$  terms, but this number is reduced considerably by combining terms with the same operator. Terms will contain operators of the form  $I S_x^{-a} S_t^{-b}$  where  $0 \leq a + b \leq 2J$ . The number of integer combinations of  $a$  and  $b$  must be less than:

$$\sum_{j=1}^{2J+1} j = \frac{(2J+2)(2J+1)}{2}. \quad (\text{IV.34})$$

We note that certain operator combinations are not possible. For example, consider  $H_3$ . The operator  $S_t^{-5}S_x^-$  is impossible because all three operators are required to construct the  $S_t^{-5}$  term leaving no possibility for it to coexist with the  $S_x^-$  term. Taking into consideration these operators, the number of terms needed to describe  $H_J$ :

$$\frac{(2J+1)^2+1}{2}. \quad (\text{IV.35})$$

Hence  $H_9$  is fully discretized using 181 vice 1,953,125 ( $5^9$ ) terms.

## E. NUMERICAL EXAMPLE: EMPLOYING HIGDON NRBC'S FOR A SINGLE WAVE PULSE AT $\Gamma_W$ IN A SEMI-INFINITE WAVE GUIDE

We now return to the semi-infinite wave guide depicted in Figure 9 of Section A. We let the wave guide width  $b = 5$  and depth  $\Theta = .1$ . The medium is dispersive with  $f = .5$  and a gravitation acceleration of  $g = 10$  is used. The initial values are zero everywhere. The boundary function  $\eta_w$  on the west boundary  $\Gamma_W$  is:

$$\eta_w(y, t) = \begin{cases} .005\Theta \cos\left[\frac{\pi}{2r}(y - y_0)\right] & \text{if } |y - y_0| \leq r \quad \& \quad 0 \leq t \leq t_0, \\ 0 & \text{otherwise,} \end{cases} \quad (\text{IV.36})$$

where  $y_0$ ,  $r$  and  $t_0$  are the wave pulse center, radius and time duration respectively. The parameter values are set at  $y_0 = 2.5$ ,  $r = 1.5$ , and  $t_0 = 0.5$ .

An artificial boundary  $\mathcal{B}$  is imposed at  $x = 5$ , defining the computational domain  $\Omega$  as a  $5 \times 5$  square. A mesh of  $20 \times 20$  is used in  $\Omega$ . The two-point backward difference method as described in Section IV. Equation IV.23 is used to estimate the Higdon boundary values. The extended domain  $\mathcal{D}$  for the reference solution  $\eta_{ref}$  is a  $15 \times 5$  rectangle with a  $60 \times 20$  mesh. An artificial boundary is imposed on  $\mathcal{D}$  at  $x = 15$ . Any spurious reflections resulting from this boundary will not affect  $\eta_{ref}$  if the run time is less than  $\frac{25}{C_0}$ . This the time it takes for a wave to travel from  $x = 0$  ( $\Gamma_E$ ) to  $x = 15$  ( $\Gamma_W$  for  $\mathcal{D}$ ) plus the time it takes for any reflection to travel back to  $x = 5$  ( $\Gamma_W$  for  $\Omega$ ). On the north and south boundaries we impose  $\frac{\partial \eta}{\partial y} = 0$ .

This “hard wall” condition, which causes waves to bounce off the north and south boundaries, will result in additional geometric dispersion.

Two cases with artificial boundaries,  $\eta_{\text{casel}}$  and  $\eta_{\text{case2}}$ , are computed and juxtaposed to  $\eta_{\text{ref}}$ . For  $\eta_{\text{casel}}$ , an NRBC with  $J = 4$  is constructed with parameters  $C_j = \{C_0, C_0, C_0, C_0\}$ . Here  $C_0 = \sqrt{g\Theta} = 1$  is the minimum wave speed. An error measurement error  $\|e(t)\|_\Omega$  on the truncated domain  $\Omega$  is obtained by using:

$$\|e(t)\|_\Omega = \sum_{i=1}^{N_x} \sum_{j=1}^{N_y} \sqrt{\frac{[\eta_{\text{ref}}(x_i, y_j, t) - \eta_{\text{casel}}(x_i, y_j, t)]^2}{N_x N_y}}, \quad (\text{IV.37})$$

where  $N_x$  and  $N_y$  are the number of grid-points in the  $x$ - and  $y$ -directions as determined by the grid spacing. For  $\eta_{\text{case2}}$ , an NRBC with  $J = 1$  and  $C_j = \{C_0\}$  is constructed and its numerical solution is compared to  $\eta_{\text{ref}}$  to obtain a second error measurement. We rate the effectiveness of NRBC's by comparing the values of  $\|e(t)\|_\Omega$ . Note that  $\|e(t)\|_\Omega$  is a function of time and will start to increase as the wave impinges on the artificial boundary.

Figures 15 through 19 show the solutions for  $\eta_{\text{ref}}$ ,  $\eta_{\text{casel}}$  and  $\eta_{\text{case2}}$  at times  $t=1, 4, 5, 8$  and 10 seconds. The top-left and -right plots depict  $\eta_{\text{ref}}$  on the truncated domain  $\Omega$  and extended domain  $\mathcal{D}$  respectively (note that, though the extended domain is continuous, it is separated in the figure so that  $\eta_{\text{ref}}$  may be better contrasted with  $\eta_{\text{casel}}$  and  $\eta_{\text{case2}}$ ). The middle- and bottom-left plots correspond to  $\eta_{\text{casel}}$  and  $\eta_{\text{case2}}$  respectively. Two graphs on the center- and bottom-right present  $\|e(t)\|_\Omega$  for  $\eta_{\text{casel}}$  and  $\eta_{\text{case2}}$ . Note that “HNRBC-2DR-1S-1L-U0-V0-T01” appears in the caption. This shorthand will be used throughout the paper to identify the figures. It is defined as follows:

- HNRBC: Higdon non-reflecting boundary condition,
- nDR:  $n$ -dimensional rectangular domain,
- nS: HNRBC applied to  $n$  sides of domain,
- nL:  $n$ -layer problem,

- $U_{mpn}$ :  $x$ -direction advection  $U = -.n$  (note:  $m$  denotes a minus sign and  $p$  a decimal point)
- $V_{pn}$ :  $y$ -direction advection  $V = .n$ .
- $Tn$ : solution at  $t = n$ .

Therefore “HNRBC-2DR-1S-1L-U0-V0-T01” refers to the solution at  $t = 1$  of a problem in which a Higdon NRBC as applied to one side of a two-dimensional rectangular domain consisting on a single layer with no advection. We will introduce multi-layer stratification and advection models in later chapters.

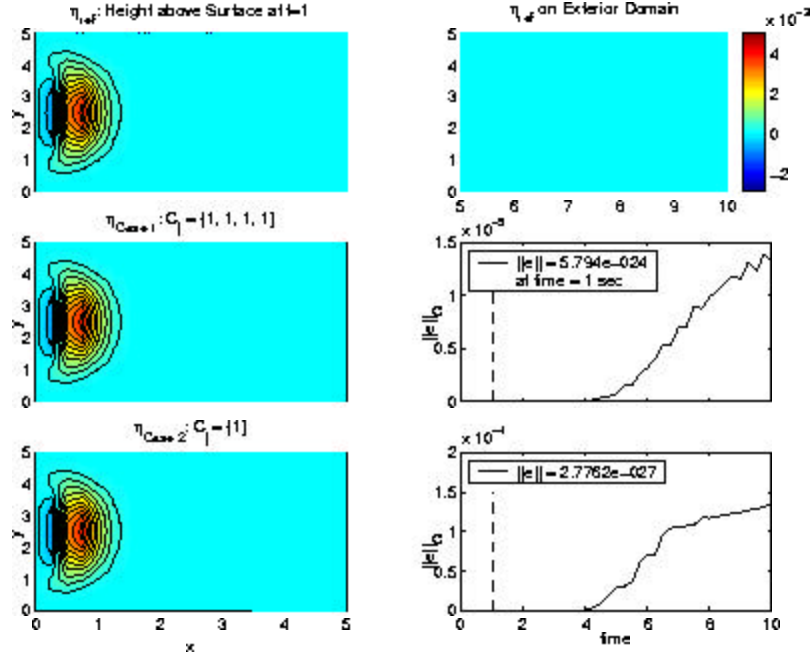


Figure 15. HNRBC-2DR-1S-1L-U0-V0-T01 with Simple Pulse Boundary Condition

At  $t = 1$  (Figure 15) the wave packet is still close to  $\Gamma_W$  and no spurious reflections have occurred. The plots for  $\eta_{ref}$ ,  $\eta_{case1}$  and  $\eta_{case2}$  are identical and  $\|e(t)\|_2$  for  $\eta_{case1}$  and  $\eta_{case2}$  is essentially 0.

At  $t = 4$  (Figure 16) the leading edge of the wave packet reaches  $\mathcal{B}$ . A slight spurious reflection is measured for  $\eta_{case1}$  and  $\eta_{case2}$ , but overall the three solutions are still very similar. At  $t = 5$  (Figure 17) the wave packet crosses  $\mathcal{B}$ . The  $\eta_{case1}$  and

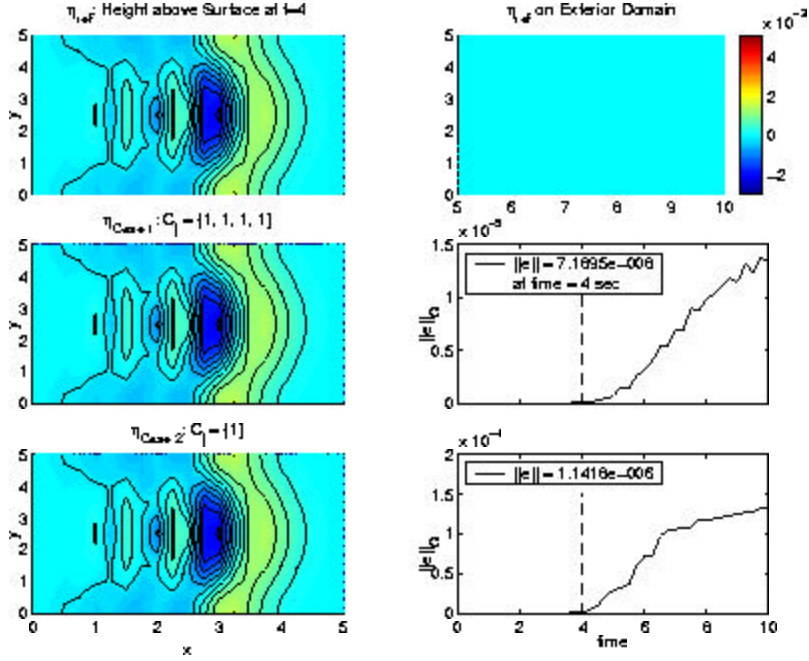


Figure 16. HNRBC-2DR-1S-1L-U0-V0-T04 with Simple Pulse Boundary Condition

$\eta_{Case2}$  plots are still indistinguishable from  $\eta_{ref}$ . At  $t = 8$  and 10 (Figures 18 and 19), most of the wave packet has left  $\Omega$  and is now visible in the extended domain  $\mathcal{D}$ . The  $\eta_{Case1}$  solution exhibits wave traces similar to those in  $\eta_{ref}$ , whereas the  $\eta_{Case2}$  solution does not. The difference in scale for  $\|e(t)\|_0$  reveals an improvement of one order of magnitude for  $\eta_{Case1}$ . This is quantitatively significant, but the qualitative results are of greater note. For  $\eta_{Case1}$ , the wave's energy has passed through  $\mathcal{B}$  relatively unimpeded. On the other hand,  $\eta_{Case2}$  reveals visible spurious reflections resulting in a backwards-moving wave that pollutes the computational domain  $\Omega$ .

This example illustrates the robustness of the Higdon NRBC. The performance of the NRBC is improved by simply increasing the order  $J$ . We now use this example to measure any improvement in the solution using the two-point Higdon NRBC approximation derived in Section IV.C versus the three-point Higdon NRBC approximation derived in Section IV.D. In both cases  $C_j = \{C_0, C_0, C_0, C_0\}$  where  $C_0 = 1$ . The results in Figure 20 report a solution improvement of an order of about

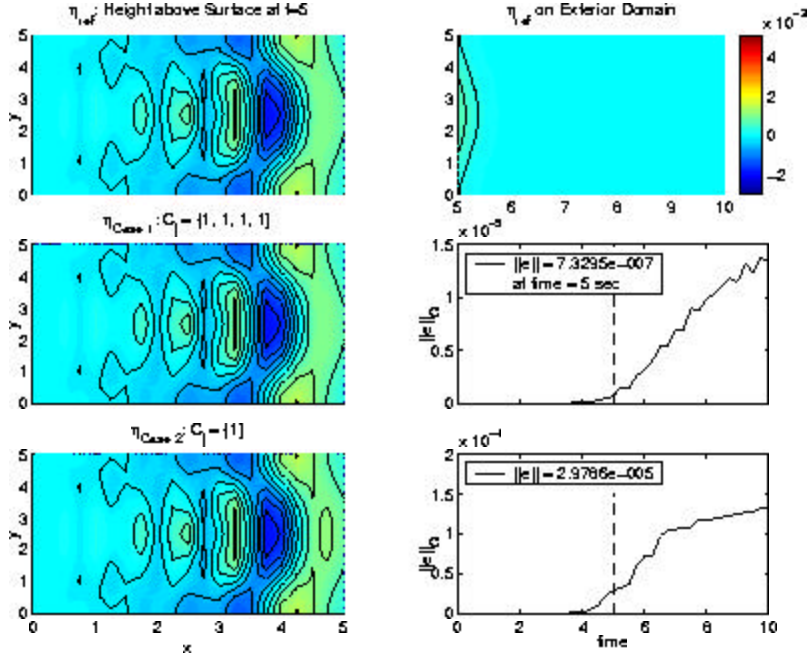


Figure 17. HNRBC-2DR-1S-1L-U0-V0-T05 with Simple Pulse Boundary Condition

1/3 when three-point approximations are used. We also use the current example's parameters to compare results when the  $C_j$  are chosen as a preprocess. An algorithm using the symmetric minimax formula (based on the Chebyshev polynomial) proposed by Sommeijer et al. [Ref. 32]. In Case 1, the Higdon NRBC has an order  $J = 4$  with  $C_j = \{C_0, C_0, C_0, C_0\}$  while in Case 2,  $J = 4$  and the  $C_j$ 's are chosen as a preprocess. In both cases the 2<sup>nd</sup> order approximation for the Higdon NRBC is used. The expected improvement is not revealed by Figure 21. This discrepancy will be checked in a follow-up example.

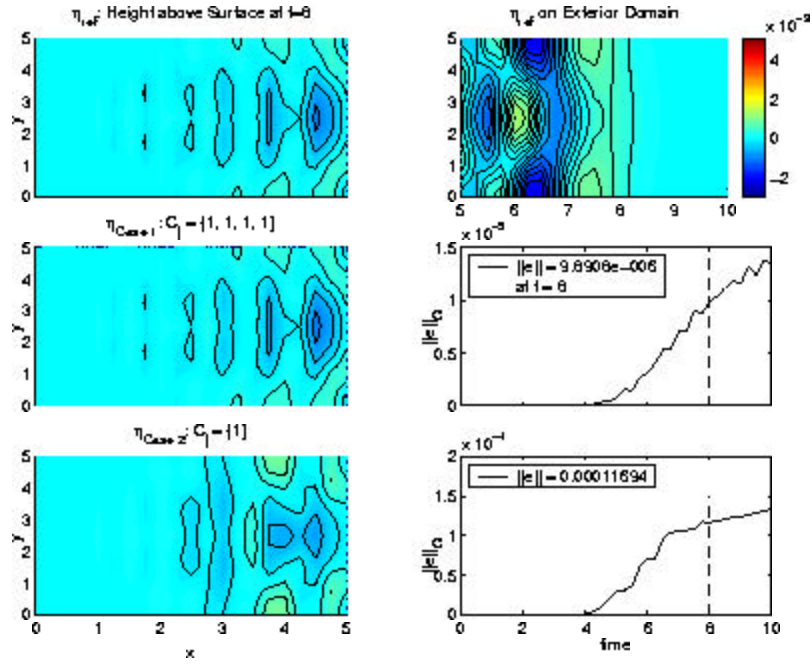


Figure 18. HNRBC-2DR-1S-1L-U0-V0-T08 with Simple Pulse Boundary Condition

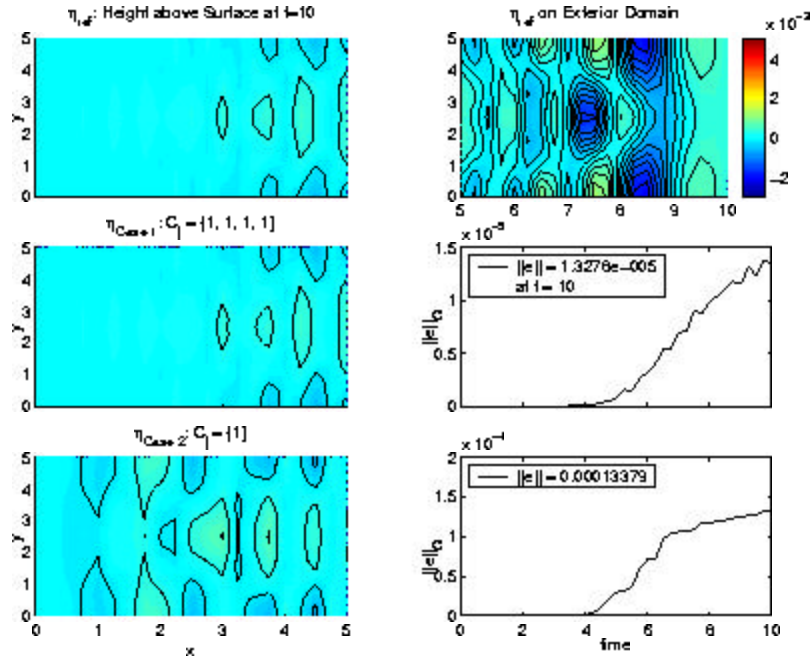


Figure 19. HNRBC-2DR-1S-1L-U0-V0-T10 with Simple Pulse Boundary Condition



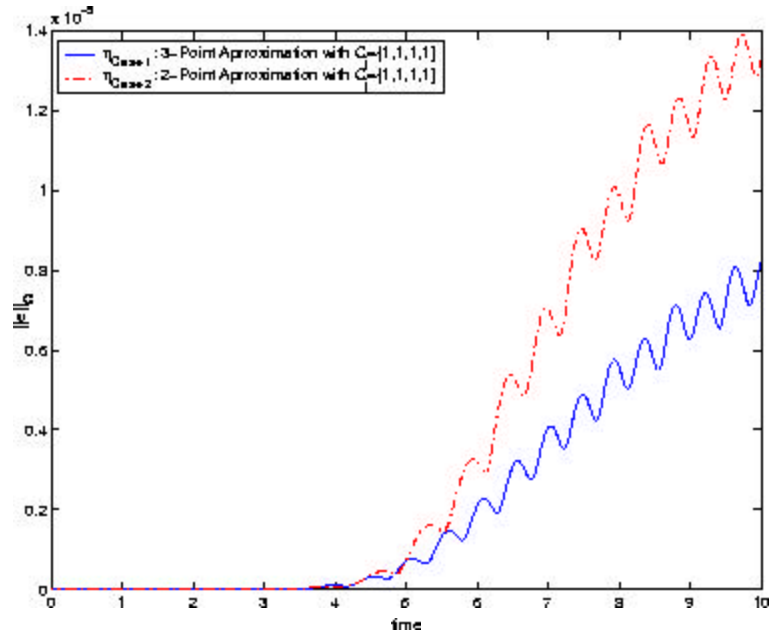


Figure 20.  $\|e(t)\|_2$  Plots for 2-Point vs. 3-Point Higdon NRBC Approximations

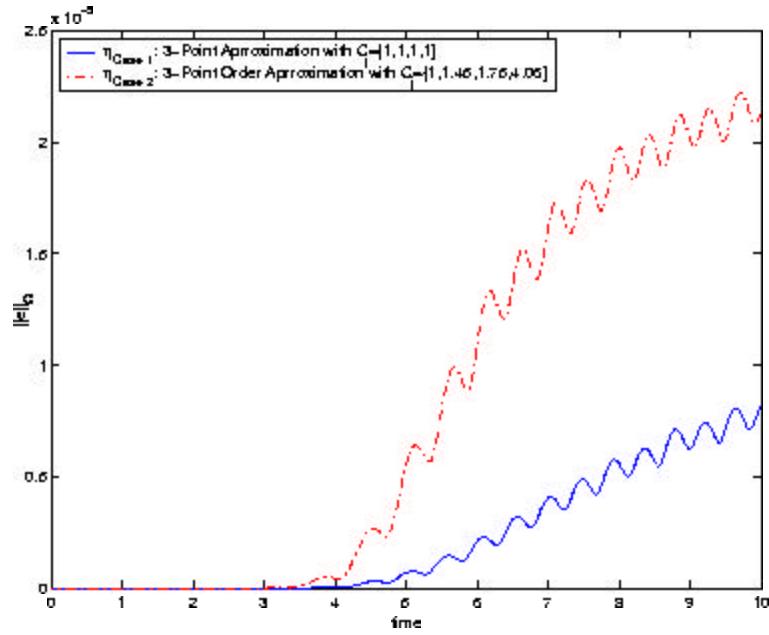


Figure 21.  $\|e(t)\|_2$  Plots for  $C_j = \{C_0, C_0, C_0, C_0\}$  vs.  $C_j$  Selected using a the Symmetric Minimax Formula with 3-Point Higdon NRBC Approximations

## F. NUMERICAL EXAMPLE: SEMI-INFINITE WAVE GUIDE WITH A CONTINUOUS WAVE INTRODUCED AT $\Gamma_W$

The set up for this example is the same as the previous example with the following exceptions: Instead of a single pulse, the boundary function on  $\Gamma_W$  is continuous, linear combination of three waves with the form:

$$\eta_w(y, t) = \sum_{m=1}^3 A_m \cos\left(\frac{n_m \pi y}{b}\right) \cos(k_m x - \omega_m t), \quad (\text{IV.38})$$

whose parameters are selected a priori to be:

$$\begin{aligned} A_m &= .01, \quad .01, \quad .01: \\ n_m &= 1, \quad 2, \quad 2: \\ \omega_m &= .81, \quad 1.37, \quad 1.68. \end{aligned}$$

To satisfy the Klein-Gordon equation, the dispersion relation:

$$\omega_m^2 = C_0^2 \left( k_m^2 + \frac{n_m^2 \pi^2}{b^2} \right) + f^2, \quad (\text{IV.39})$$

must be invoked to determine  $k_m$ :

$$k_m = \sqrt{\frac{\omega_m^2 - f^2}{C_0^2} - \frac{n_m^2 \pi^2}{b^2}}. \quad (\text{IV.40})$$

Thus  $k_m$ , using the parameters given for (IV.38), is:

$$k_m = .11, \quad .22, \quad 1.00.$$

Two cases,  $\eta_{\text{case1}}$  and  $\eta_{\text{case2}}$ , are again juxtaposed to  $\eta_{\text{ref}}$  in Figure 22. For  $\eta_{\text{case1}}$ , an NRBC with  $J = 5$  and parameters  $C_j = \{C_0, C_0, C_0, C_0, C_0\}$  is used. For  $\eta_{\text{case2}}$ ,  $J = 2$  and  $C_j = \{C_0, C_0\}$  is used. An error measurement  $\|e(t)\|_n$  given by (IV.37) is determined. As expected, the higher-order Higdon NRBC results in a smaller  $\|e(t)\|_n$  and therefore generates less spurious reflection at  $\mathcal{B}$ .

We now examine previous suppositions considered in Section III.C concerning the selection of the Higdon parameters  $C_j$ .

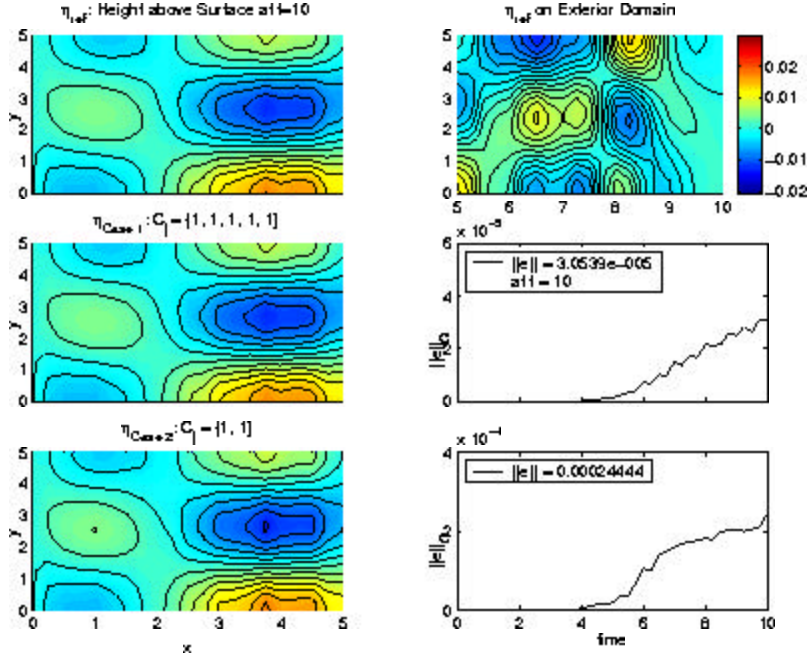


Figure 22. HNRBC-2DR-1S-1L-U0-V0-T10 with Continuous Wave Boundary Condition

- In Figure 23 we compare  $C_j = \{1, 1, 1, 1, 1\}$  vs. a 5<sup>th</sup>-order Higdon NRBC where the  $C_j$ 's are automatically selected using the minimax formula based on Chebyshev polynomials. The result favors the former, discounting previous supposition that auto-selection of  $C_j$ 's using this scheme might yield an improvement.
- In Figure 24 we compare  $C_j = \{1, 1, 1, 1, 1\}$  to a 5<sup>th</sup>-order NRBC where the  $C_j$ 's are evenly distributed from  $C_0$  to  $\sqrt{C_0^2 + f^2}$ . Any improvement indicated by using the latter scheme is not significant.
- In Figure 25 we compare  $C_j = \{1, 1, 1, 1, 1\}$  to a set of five  $C_j$ 's that are evenly distributed from  $C_0$  to the maximum resolvable wave number  $k_{max} = \frac{\pi}{5\Delta x}$ . Again the simpler scheme for choosing  $C_j$ 's is numerically superior.

Based on results in this and the previous section we conclude that spurious reflections at the Higdon boundary are reduced by using:

- $C_j$ 's equal to  $\{C_0, \dots, C_0\}$ .
- Higher order Higdon NRBC's.

- three-point approximations for the derivatives in the Higdon NRBC.

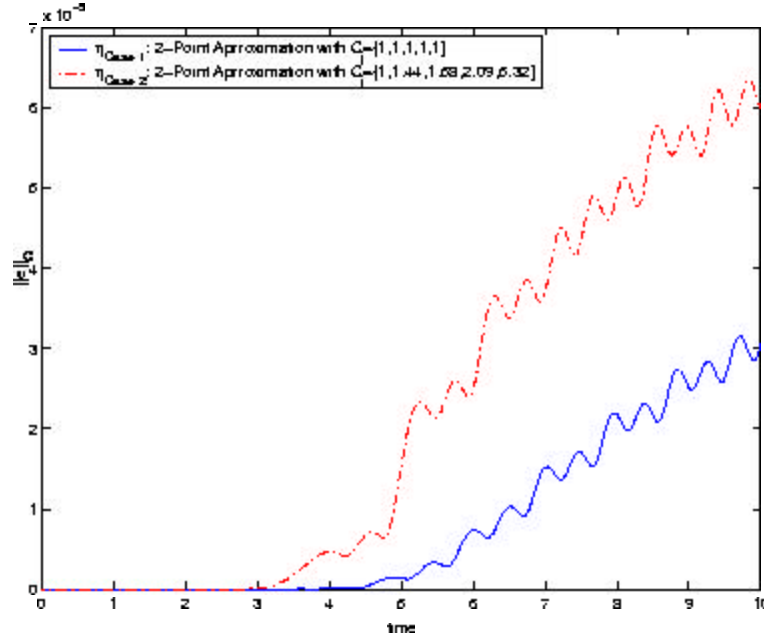


Figure 23.  $\|e(t)\|_n$  for  $C_j = \{1, 1, 1, 1, 1\}$  vs.  $C_j$  Auto-Selected Using Minimax Formula Based on Chebyshev Polynomials.

We make one final comparison before closing. In Figure 26 a Higdon NRBC with  $J = 5$  that uses a two-point approximation is juxtaposed to a Higdon NRBC with  $J = 4$  that uses a three-point approximation. We see that the results are quite close. However differences in computational effort is significant. From Section IV.C we know that to discretize a two-point Higdon NRBC with  $J = 5$  required the generation of 125 ( $3^5$ ) terms that were subsequently reduced to 21 terms when redundancies are combined (IV.25). From Section IV.D we determined that to discretize a three-point Higdon NRBC with  $J = 4$  required the generation of 625 ( $5^4$ ) terms that were subsequently reduced to 41 terms (IV.35). Since the discrete Higdon NRBC formula must be applied every time an artificial boundary grid point is encountered, it is apparent from this comparison that it is more efficient to use the two-point approximation with a higher Higdon order  $J$ .

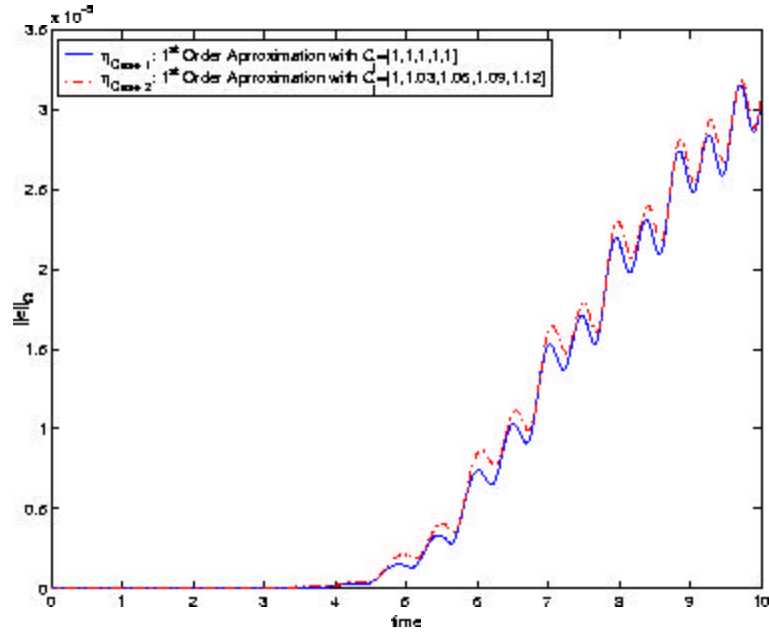


Figure 24.  $\|e(t)\|_n$  for  $C_j = \{1, 1, 1, 1, 1\}$  vs.  $C_j$  Distributed Evenly from  $C_0$  to  $\sqrt{C_0^2 + f^2}$

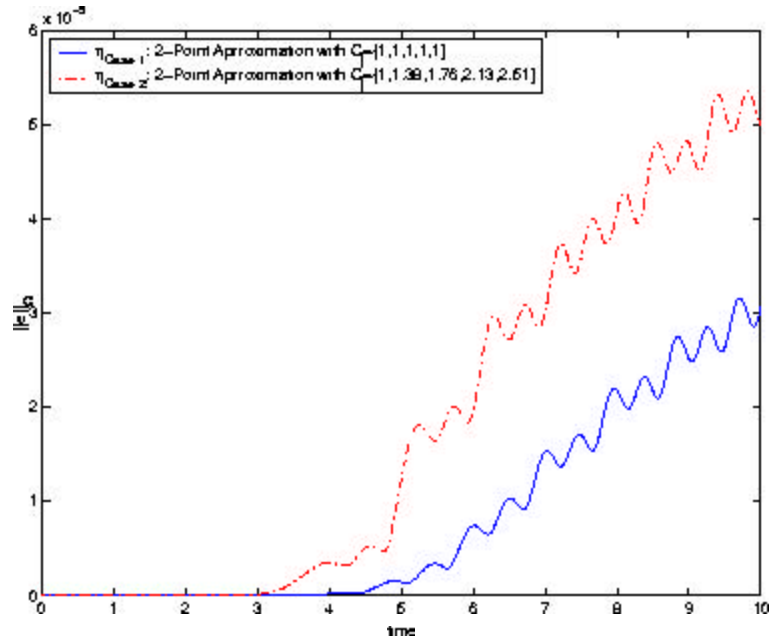


Figure 25.  $\|e(t)\|_n$  for  $C_j = \{1, 1, 1, 1, 1\}$  vs.  $C_j$  Distributed Evenly from  $C_0$  to  $k_{max} = \frac{\pi}{5\Delta x}$

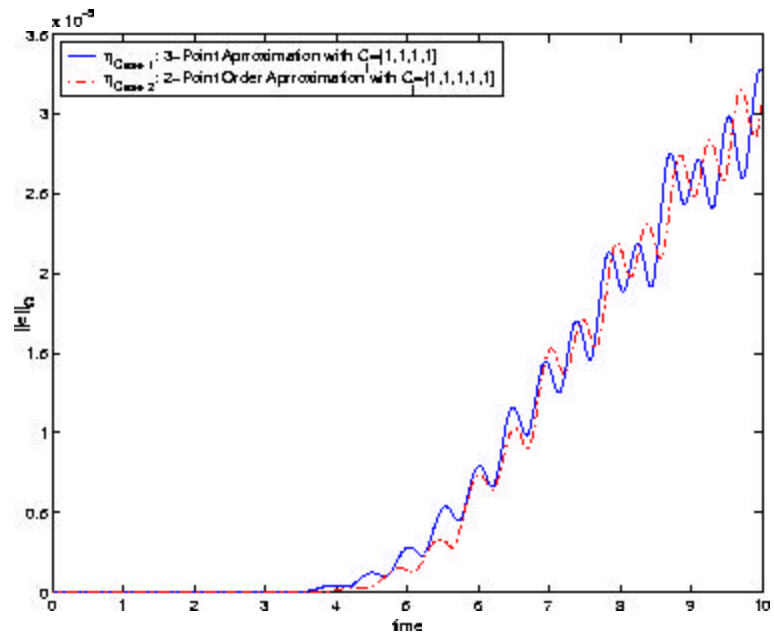


Figure 26.  $\|e(t)\|_2$  for  $C_j = \{1, 1, 1, 1, 1\}$  Using a Two-Point HNRBC Approximation vs.  $C_j = \{1, 1, 1, 1\}$  Using a Three-Point Higdon Approximation

## V. A N-LAYER STRATIFIED DISPERSIVE WAVE MODEL

We now lift the homogeneous fluid assumption and develop equations to model geophysical flow in a stratified medium. A suitable medium for a geophysical dynamics is the open ocean where fluid density  $\rho$  is affected by salinity and temperature. Salinity changes are slight in this environment, and temperature remains relatively constant in the horizontal directions. However, temperature does change significantly in the vertical direction. Therefore we approximate  $\rho$  to be a function of  $z$  only. Since the fluid is assumed to be incompressible,  $\rho$  does not vary with pressure  $p$ .

The linearized shallow water equations (II.78 and II.80) were derived in part from the continuity equation for homogenous, incompressible fluids (II.6):

$$\frac{\partial u}{\partial x} + \frac{\partial v}{\partial y} + \frac{\partial w}{\partial z} = 0.$$

It was shown by (II.59) that  $u$  and  $v$  are independent of  $z$  for a constant density fluid enabling us to uncouple  $w$  from  $u$  and  $v$  in (II.6), which after integrating yielded (II.61):

$$w(x, y, z, t) = -z \left( \frac{\partial u(x, y, t)}{\partial x} + \frac{\partial v(x, y, t)}{\partial y} \right) + \bar{w}(x, y, t).$$

This critical step in the derivation is no longer possible when we assume that  $\rho$  is dependent on  $z$ .

We extricate ourselves from this conundrum by developing a layered shallow water approximation where  $\rho$  is constant in each layer (Fig. 27). Here it is assumed that the fluid is still incompressible and that density  $\rho_i$  is constant in each layer  $L_i$ , but varies in the different layers. In order for this stratification scheme to be stable,  $\rho_i$  must be monotonically increasing downward [Ref. 28]. Additionally we assume that there is no fluid mixing between layers.

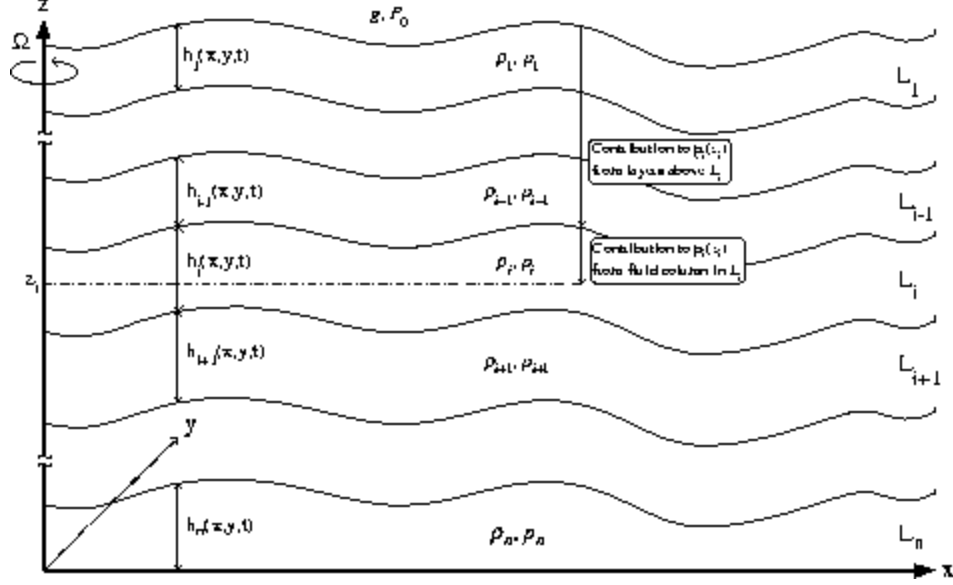


Figure 27.  $N$ -Layer Shallow Water Model

Referring to the  $N$ -layer shallow water model, the pressure  $p_i$  at any point in  $L_i$  is determined from hydrostatic principles:

$$p_i = P_0 + g \left( \sum_{j=1}^{i-1} \rho_j h_j + \rho_i \sum_{j=i}^N (h_j - z) \right), \quad (\text{V.1})$$

where  $P_0$  is a constant ambient pressure at the surface  $h_0$  and  $N$  is the total number of layers in the model. In (V.1), the first summation term is the contribution to  $p_i$  from the layers above  $L_i$ . The second summation term is the contribution to  $p_i$  from the liquid column in  $L_i$ . We use (II.80) and (V.1) to obtain the horizontal momentum equations in  $L_i$ :

$$\begin{aligned} \frac{\partial u_i}{\partial t} + u_i \frac{\partial u_i}{\partial x} + v_i \frac{\partial u_i}{\partial y} - f v_i &= -g \left( \sum_{j=1}^{i-1} \frac{\rho_j}{\rho_i} \frac{\partial h_j}{\partial x} + \sum_{j=i}^N \frac{\partial h_j}{\partial x} \right), \\ \frac{\partial v_i}{\partial t} + u_i \frac{\partial v_i}{\partial x} + v_i \frac{\partial v_i}{\partial y} + f u_i &= -g \left( \sum_{j=1}^{i-1} \frac{\rho_j}{\rho_i} \frac{\partial h_j}{\partial y} + \sum_{j=i}^N \frac{\partial h_j}{\partial y} \right), \end{aligned} \quad (\text{V.2})$$

where  $u_i$ ,  $v_i$  and  $w_i$  are the  $x$ -,  $y$ -, and  $z$ -components of velocity in  $L_i$ .



Derivation of the vertical momentum equation in  $L_i$  is more complex. Since  $\rho_i$  is constant in  $L_i$ , we can uncouple the continuity equation for  $L_i$ :

$$w_i(x, y, z, t) = -z \left( \frac{\partial u_i(x, y, t)}{\partial x} + \frac{\partial v_i(x, y, t)}{\partial y} \right) + \bar{w}_i(x, y, t), \quad (\text{V.3})$$

where  $w_i$  is a vertical velocity component in  $L_i$ . For brevity we drop dependent variables from subsequent expressions. At the interface between  $L_{i-1}$  and  $L_i$  where  $z = \sum_{j=i}^N h_j$ , the vertical speed component  $w_i$  (see similar discussion in Section II.B.6) is:

$$w_i = \frac{\partial}{\partial t} \sum_{j=i}^N h_j + u_i \frac{\partial}{\partial x} \sum_{j=i}^N h_j + v_i \frac{\partial}{\partial y} \sum_{j=i}^N h_j. \quad (\text{V.4})$$

This implies that:

$$\bar{w}_i = \frac{\partial}{\partial t} \sum_{j=i}^N h_j + \frac{\partial}{\partial x} \left( u_i \sum_{j=i}^N h_j \right) + \frac{\partial}{\partial y} \left( v_i \sum_{j=i}^N h_j \right). \quad (\text{V.5})$$

Similarly, at the interface between  $L_i$  and  $L_{i+1}$  where  $z = \sum_{j=i+1}^N h_j$ , the vertical speed component  $w_i$  is:

$$w_i = \frac{\partial}{\partial t} \sum_{j=i+1}^N h_j + u_i \frac{\partial}{\partial x} \sum_{j=i+1}^N h_j + v_i \frac{\partial}{\partial y} \sum_{j=i+1}^N h_j. \quad (\text{V.6})$$

which implies that:

$$\bar{w}_i = \frac{\partial}{\partial t} \sum_{j=i+1}^N h_j + \frac{\partial}{\partial x} \left( u_i \sum_{j=i+1}^N h_j \right) + \frac{\partial}{\partial y} \left( v_i \sum_{j=i+1}^N h_j \right). \quad (\text{V.7})$$

Since  $\bar{w}_i$  is independent of  $z$ , (V.5) and (V.7) must be equal. Therefore:

$$\boxed{\frac{\partial}{\partial t} h_i + \frac{\partial}{\partial x} (u_i h_i) + \frac{\partial}{\partial y} (v_i h_i) = 0,} \quad (\text{V.8})$$

Equation (V.8) is the vertical momentum equation for  $L_i$ . Together with (V.2) this completes the description of the fluid motion inside of the  $i^{\text{th}}$ -layer  $L_i$ .

Before considering a numerical solution we linearize the governing equations for each layer. We assume that the  $u_i$ ,  $v_i$ , and  $h_i$  are dominated by constant terms  $U_i$ ,  $V_i$  and  $\Theta_i$ . Superimposed on these are small variations  $u_i^*$ ,  $v_i^*$ , and  $\eta_i$  of  $O(\delta)$ , i.e.:

$$u_i = U_i + u_i^*, \quad v_i = V_i + v_i^*, \quad \text{and} \quad h_i = \Theta_i + \eta_i. \quad (\text{V.9})$$

Substituting these in (V.2) and (V.8) and neglecting terms of  $O(\delta^2)$  yields:

$$\begin{aligned}\frac{\partial u_i^*}{\partial t} + U_i \frac{\partial u_i^*}{\partial x} + V_i \frac{\partial u_i^*}{\partial y} - f(V_i + v_i^*) &= -g \left( \sum_{j=1}^{i-1} \frac{\rho_j}{\rho_i} \frac{\partial \eta_j}{\partial x} + \sum_{j=i}^N \frac{\partial \eta_j}{\partial x} \right), \\ \frac{\partial v_i^*}{\partial t} + U_i \frac{\partial v_i^*}{\partial x} + V_i \frac{\partial v_i^*}{\partial y} + f(U_i + u_i^*) &= -g \left( \sum_{j=1}^{i-1} \frac{\rho_j}{\rho_i} \frac{\partial \eta_j}{\partial y} + \sum_{j=i}^N \frac{\partial \eta_j}{\partial y} \right), \\ \frac{\partial \eta_i}{\partial t} + U_i \frac{\partial \eta_i}{\partial x} + V_i \frac{\partial \eta_i}{\partial y} + \Theta_i \left( \frac{\partial u_i^*}{\partial x} + \frac{\partial v_i^*}{\partial y} \right) &= 0,\end{aligned}\tag{V.10}$$

If we assume that there is no advection (e.g.  $U_i = V_i = 0$ ), then (V.10) reduces to:

$$\boxed{\begin{aligned}\frac{\partial u_i^*}{\partial t} - f v_i^* &= -g \left( \sum_{j=1}^{i-1} \frac{\rho_j}{\rho_i} \frac{\partial \eta_j}{\partial x} + \sum_{j=i}^N \frac{\partial \eta_j}{\partial x} \right), \\ \frac{\partial v_i^*}{\partial t} + f u_i^* &= -g \left( \sum_{j=1}^{i-1} \frac{\rho_j}{\rho_i} \frac{\partial \eta_j}{\partial y} + \sum_{j=i}^N \frac{\partial \eta_j}{\partial y} \right), \\ \frac{\partial \eta_i}{\partial t} + \Theta_i \left( \frac{\partial u_i^*}{\partial x} + \frac{\partial v_i^*}{\partial y} \right) &= 0.\end{aligned}}\tag{V.11}$$

Equation (V.11) is the linearized shallow water equation for the stratified  $N$ -layer model with no advection.

## A. REDUCING THE STRATIFIED $N$ -LAYER MODEL TO THE KLEIN-GORDON FORM

In order to combine linearized components of the stratified  $N$ -layer model (V.11) to a Klein-Gordon form, we use a step-by-step derivation that is similar to that used in Section II.B.8.

**Step 1:** Perform the following substitutions in (V.11):

$$\hat{u}_i = u_i^* \Theta_i \text{ and } \hat{v}_i = v_i^* \Theta_i.$$

Recalling that  $\Theta_i$  is independent of time, the result is:

$$\frac{\partial \hat{u}_i}{\partial t} - f \hat{v}_i = -g \Theta_i \left( \sum_{j=1}^{i-1} \frac{\rho_j}{\rho_i} \frac{\partial \eta_j}{\partial x} + \sum_{j=i}^N \frac{\partial \eta_j}{\partial x} \right), \quad (\text{V.12})$$

$$\frac{\partial \hat{v}_i}{\partial t} + f \hat{u}_i = -g \Theta_i \left( \sum_{j=1}^{i-1} \frac{\rho_j}{\rho_i} \frac{\partial \eta_j}{\partial y} + \sum_{j=i}^N \frac{\partial \eta_j}{\partial y} \right), \quad (\text{V.13})$$

$$\frac{\partial \eta_i}{\partial t} + \frac{\partial \hat{u}_i}{\partial x} + \frac{\partial \hat{v}_i}{\partial y} = 0. \quad (\text{V.14})$$

**Step 2:** Let  $f$  be constant. Take the partial derivative of (V.12) with respect to  $x$ :

$$\frac{\partial}{\partial x} \left( \frac{\partial \hat{u}_i}{\partial t} \right) - f \frac{\partial \hat{v}_i}{\partial x} = -g \Theta_i \left( \sum_{j=1}^{i-1} \frac{\rho_j}{\rho_i} \frac{\partial^2 \eta_j}{\partial x^2} + \sum_{j=i}^N \frac{\partial^2 \eta_j}{\partial x^2} \right),$$

and the partial derivative of (V.13) with respect to  $y$ :

$$\frac{\partial}{\partial y} \left( \frac{\partial \hat{v}_i}{\partial t} \right) + f \frac{\partial \hat{u}_i}{\partial y} = -g \Theta_i \left( \sum_{j=1}^{i-1} \frac{\rho_j}{\rho_i} \frac{\partial^2 \eta_j}{\partial y^2} + \sum_{j=i}^N \frac{\partial^2 \eta_j}{\partial y^2} \right).$$

Add the resulting equations:

$$\frac{\partial}{\partial t} \left( \frac{\partial \hat{u}_i}{\partial x} + \frac{\partial \hat{v}_i}{\partial y} \right) - f \left( \frac{\partial \hat{v}_i}{\partial x} - \frac{\partial \hat{u}_i}{\partial y} \right) = -g \Theta_i \nabla^2 \left( \sum_{j=1}^{i-1} \frac{\rho_j}{\rho_i} \eta_j + \sum_{j=i}^N \eta_j \right). \quad (\text{V.15})$$

**Step 3:** Take the partial derivative of (V.12) with respect to  $y$ :

$$\frac{\partial}{\partial y} \left( \frac{\partial \hat{u}_i}{\partial t} \right) - f \frac{\partial \hat{v}_i}{\partial y} = -g \Theta_i \frac{\partial}{\partial y} \left( \sum_{j=1}^{i-1} \frac{\rho_j}{\rho_i} \frac{\partial \eta_j}{\partial x} + \sum_{j=i}^N \frac{\partial \eta_j}{\partial x} \right),$$

and the partial derivative of (V.13) with respect to  $x$ :

$$\frac{\partial}{\partial x} \left( \frac{\partial \hat{v}_i}{\partial t} \right) + f \frac{\partial \hat{u}_i}{\partial x} = -g \Theta_i \frac{\partial}{\partial x} \left( \sum_{j=1}^{i-1} \frac{\rho_j}{\rho_i} \frac{\partial \eta_j}{\partial y} + \sum_{j=i}^N \frac{\partial \eta_j}{\partial y} \right).$$

Subtract the resulting equations:

$$\frac{\partial}{\partial t} \left( \frac{\partial \hat{u}_i}{\partial y} - \frac{\partial \hat{v}_i}{\partial x} \right) - f \left( \frac{\partial \hat{v}_i}{\partial y} + \frac{\partial \hat{u}_i}{\partial x} \right) = 0. \quad (\text{V.16})$$

**Step 4:** Take the partial derivative of (V.15) with respect to  $t$  and rearrange the resulting terms:

$$f \frac{\partial}{\partial t} \left( \frac{\partial \hat{v}_i}{\partial x} - \frac{\partial \hat{u}_i}{\partial y} \right) = \frac{\partial^2}{\partial t^2} \left( \frac{\partial \hat{u}_i}{\partial x} + \frac{\partial \hat{v}_i}{\partial y} \right) + g \Theta_i \frac{\partial}{\partial t} \nabla^2 \left( \sum_{j=1}^{i-1} \frac{\rho_j}{\rho_i} \eta_j + \sum_{j=i}^N \eta_j \right).$$

Multiply (V.16) by  $f$  and rearrange the resulting terms:

$$-f \frac{\partial}{\partial t} \left( \frac{\partial \hat{v}_i}{\partial x} - \frac{\partial \hat{u}_i}{\partial y} \right) = f^2 \left( \frac{\partial \hat{v}_i}{\partial y} + \frac{\partial \hat{u}_i}{\partial x} \right).$$

Add the resulting equations:

$$\left( \frac{\partial^2}{\partial t^2} + f^2 \right) \left( \frac{\partial \hat{u}_i}{\partial x} + \frac{\partial \hat{v}_i}{\partial y} \right) + g \Theta_i \frac{\partial}{\partial t} \nabla^2 \left( \sum_{j=1}^{i-1} \frac{\rho_j}{\rho_i} \eta_j + \sum_{j=i}^N \eta_j \right) = 0. \quad (\text{V.17})$$

**Step 5:** Using (V.14) rewrite (V.17) as:

$$\frac{\partial}{\partial t} \left[ \frac{\partial^2 \eta_i}{\partial t^2} + f^2 \eta_i - g \Theta_i \nabla^2 \left( \sum_{j=1}^{i-1} \frac{\rho_j}{\rho_i} \eta_j + \sum_{j=i}^N \eta_j \right) \right] = 0. \quad (\text{V.18})$$

**Step 6:** Integrating (V.18) with respect to  $t$  yields:

$$\boxed{\frac{\partial^2 \eta_i}{\partial t^2} - g \Theta_i \nabla^2 \left( \sum_{j=1}^{i-1} \frac{\rho_j}{\rho_i} \eta_j + \sum_{j=i}^N \eta_j \right) + f^2 \eta_i = S_i(x, y)}, \quad (\text{V.19})$$

where  $S_i(x, y)$  is an arbitrary function that results from integration. Equation V.19, resembles the Klein-Gordon form reported in (II.88), and is a restatement of the set of linearized (about a zero mean) shallow water equations (V.11) generated for the  $N$ -layer stratification model.

## B. DISCRETIZING THE KLEIN-GORDON FORM OF THE STRATIFIED $N$ -LAYER MODEL

A standard second-order central-difference scheme is used to discretize (V.19). On a spatial and temporal grid of our choosing, we let  $\eta_{i,pq}^n$  be the FD approximation of  $\eta_i(x, y, t)$  at grid point  $(x_p, y_q)$  and at time  $t_n$  in layer  $L_i$ . Thus solving explicitly

for  $\eta_{i,pq}^{n+1}$  yields:

$$\begin{aligned}
\eta_{i,pq}^{n+1} = & \left[ 2 - (f\Delta t)^2 \right] \eta_{i,pq}^n - \eta_{i,pq}^{n-1} \\
& + \left( \frac{C_{0i}\Delta t}{\Delta x} \right)^2 \left[ \sum_{j=1}^{i-1} \frac{\rho_j}{\rho_i} \left( \eta_{j,p+1,q}^n - 2\eta_{j,pq}^n + \eta_{j,p-1,q}^n \right) \right] \\
& + \left( \frac{C_{0i}\Delta t}{\Delta x} \right)^2 \left[ \sum_{j=i}^N \left( \eta_{j,p+1,q}^n - 2\eta_{j,pq}^n + \eta_{j,p-1,q}^n \right) \right] \\
& + \left( \frac{C_{0i}\Delta t}{\Delta y} \right)^2 \left[ \sum_{j=1}^{i-1} \frac{\rho_j}{\rho_i} \left( \eta_{j,p,q+1}^n - 2\eta_{j,pq}^n + \eta_{j,p,q-1}^n \right) \right] \\
& + \left( \frac{C_{0i}\Delta t}{\Delta y} \right)^2 \left[ \sum_{j=i}^N \left( \eta_{j,p,q+1}^n - 2\eta_{j,pq}^n + \eta_{j,p,q-1}^n \right) \right]
\end{aligned} \tag{V.20}$$

where  $C_{0i} = \sqrt{g\Theta_i}$ . We use this interior scheme in the numerical experiments presented in the next section. The Higdon NRBC is applied independently to each layer and takes the form:

$$\prod_{j=1}^J \left( \frac{\partial}{\partial t} + C_{ji} \frac{\partial}{\partial x} \right) \eta_i = 0 \tag{V.21}$$

The development of its discretization follows the discussion in Section IV.C. Hard wall or Neumann conditions are also applied independently to each layer and discretized accordingly. Since the discrete forms of the Higdon NRBC, Nuemann condition, and the time stepping scheme (V.20) are explicit, the whole scheme is explicit.

### C. NUMERICAL EXAMPLE: THE STRATIFIED $N$ -LAYER MODEL

Consider a geophysical process that occurs in a semi-infinite channel (Figure 9). All assumptions and simplifications used to derive the  $N$ -layer model apply. A Cartesian coordinate system  $(x, y)$  is introduced such that the channel is parallel

to the  $x$ -direction. On the north and south boundaries  $\Gamma_N$  and  $\Gamma_S$  we specify the Neumann condition:

$$\frac{\partial \eta_i}{\partial y} = 0 \quad \text{for} \quad i = 1 \dots N. \quad (\text{V.22})$$

On the west boundary  $\Gamma_W$  we prescribe  $\eta_i$  using a Dirichlet condition, i.e.,

$$\eta_i(0, y, t) = \eta_{w_i}(y, t) \quad \text{for} \quad i = 1 \dots N, \quad (\text{V.23})$$

where  $\eta_{w_i}(y, t)$  is a given function for an incoming wave or disturbance. At  $x \rightarrow \infty$  the solution is bounded and does not include any incoming waves. The initial conditions are:

$$\eta_i(x, y, 0) = 0, \quad \frac{\partial \eta_i(x, y, 0)}{\partial t} = 0 \quad \text{for} \quad i = 1 \dots N. \quad (\text{V.24})$$

To obtain a well-posed problem in a finite domain  $\Omega$  we impose a high-order Higdon-NRBC on the east boundary  $\Gamma_E$ .

We now apply the new stratification scheme to a test problem using the semi-infinite wave-guide. A channel width  $b = 5$  and depth  $d = \sum_{i=1}^N \Theta_i = .1$  are selected (note that to satisfy the shallow water assumption, it must be true that depth  $d \ll$  horizontal dimensions). The stratified medium is modeled with six layers. The layer thicknesses from top to bottom are  $\theta_i = \{.01, .01, .01, .01, .01, .05\}$ . The density for each layer is given by  $\rho_i = \{1, 1.05, 1.1, 1.15, 1.2, 1.25\}$ . A gravitational parameter  $g = 10$  and a dispersion parameter  $f = .5$  is used.

The boundary function  $\eta_w$  on  $\Gamma_W$  is stipulated to simulate two geophysical events. A surface disturbance, akin to the wind acting on the ocean, is initiated in  $L_1$  by setting:

$$\eta_{w_1}(y, t) = \begin{cases} .0005 \cos \left[ \frac{\pi}{5}(y - 2.5) \right] \sin \pi t & 0 \leq t \leq 12.5, \\ 0 & \text{otherwise.} \end{cases} \quad (\text{V.25})$$

Note that the maximum amplitude of the disturbance is small relative to the layer thickness  $\theta_1 = .01$  so that the validity of the model, which is based on perturbation analysis, is not violated. A second disturbance, simulating seismic activity on the

ocean floor, is initiated in the  $L_6$  and given by:

$$\eta_{w_6} = \begin{cases} .001 & \text{if } |y - 2.5| \leq 1.5 \quad \& \quad 6 \leq t \leq 7.5, \\ 0 & \text{otherwise.} \end{cases} \quad (\text{V.26})$$

All other values for  $\eta_{w_i}$  are zero. The simulation is run for 15 time units.

The problem is solved for three different scenarios. First, an extended domain  $\mathcal{D}$  is constructed using a  $15 \times 5$  rectangle with a  $60 \times 20$  mesh to compute a reference solution  $\eta_{ref}$ . Then two additional solutions,  $\eta_{case1}$  and  $\eta_{case2}$ , are computed on a truncated domain  $\Omega$  in which an artificial boundary  $\mathcal{B}$  imposed at  $x = 5$ . A  $20 \times 20$  mesh is used on the resulting  $5 \times 5$  square so that the mesh for  $\Omega$  and  $\mathcal{D}$  are identical in the truncated region. For  $\eta_{case1}$ , a Higdon NRBC of order  $J = 5$  with parameters  $C_j = \{1, 1, 1, 1, 1\}$  is used for each layer. For  $\eta_{case2}$ ,  $J = 2$  and  $C_j = \{1, 1\}$  is used. Note that the value  $\eta$  in each case represents the total perturbation on the domain surface and is a combination of perturbation effects in each layer.

The reference solution  $\eta_{ref}$  is then juxtaposed with  $\eta_{case1}$  and  $\eta_{case2}$  both graphically and quantitatively. The respective numerical solutions are used to produce filled contour plots that provide a “fingerprint” for the resulting wave action. All contours and color schemes are relative to  $\eta_{ref}$ . These solutions are then used to obtain error measurements  $\|e(t)\|_\Omega$  which are calculated by:

$$\|e(t)\|_\Omega = \sum_{i=1}^{N_x} \sum_{j=1}^{N_y} \sqrt{\frac{[\eta_{ref}(x_i, y_j, t) - \eta_{case1}(x_i, y_j, t)]^2}{N_x N_y}}, \quad (\text{V.27})$$

where  $N_x$  and  $N_y$  are determined by grid spacing. In both cases, the error at the surface and for each layer interface is plotted versus time. Note that the size of  $\mathcal{D}$  precludes spurious reflections from polluting  $\eta_{ref}$ . Therefore  $\|e(t)\|_\Omega$  serves as a measure of spurious reflection at  $\mathcal{B}$ .

At  $t = 7$  (Figure 28), the surface disturbance in  $L_1$  has populated  $\Omega$  and is now visible in  $\mathcal{D}$ . In addition, the bottom disturbance has been initiated and is propagating in  $\Omega$ . Both  $case1$  and  $\eta_{case2}$  exhibit wave traces similar to those in  $\eta_{ref}$ . However, the error measurement for  $\eta_{case1}$  is an order of magnitude smaller than that

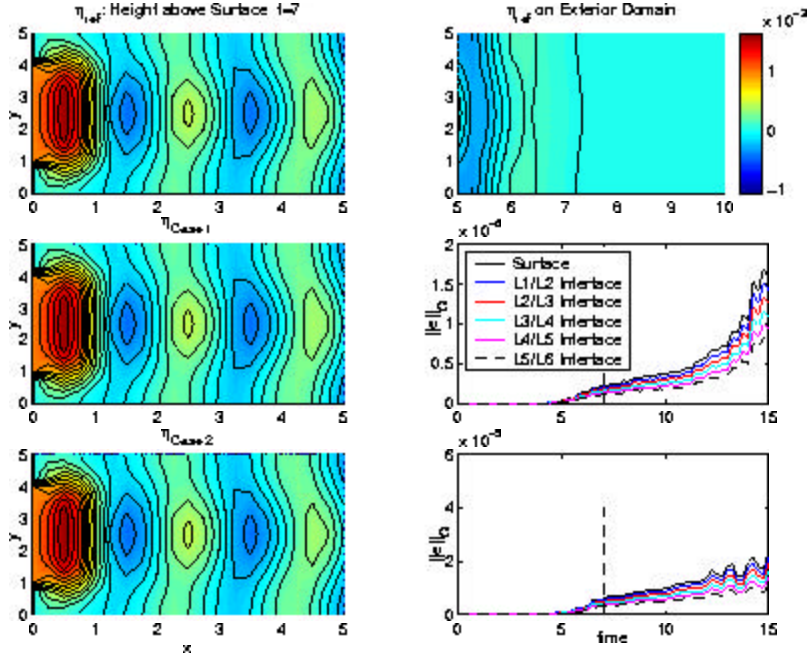


Figure 28. HNRBC-2DR-1S-6L-U0-V0-T07

of  $\eta_{\text{case } 2}$ . This demonstrates that simply increasing the Higdon NRBC order  $J$  reduces spurious reflection. A description of the shorthand notation used in the figure caption was given in Section IV.E.

At time  $t = 15$  (Figure 29), the surface disturbance, which ended at  $t = 12.5$ , continues to propagate in  $\Omega$  and  $\mathcal{D}$ . The bottom disturbance has successfully passed through  $\Gamma_E$  without a significant increase in spurious reflection. The wave trace for  $\eta_{\text{case } 1}$  closely resembles that of  $\eta_{\text{ref}}$ , however deviations in  $\eta_{\text{case } 2}$  are now visible. This example demonstrates that a properly constructed Higdon NRBC can be used to restrict the domain of the  $N$ -layer stratification model governed by the linearized shallow water equation.



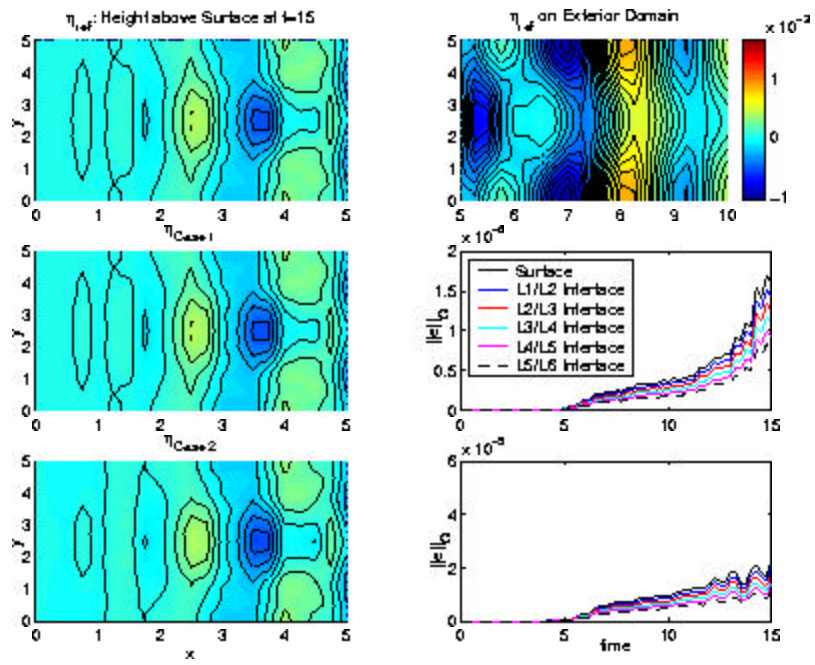


Figure 29. HNRBC-2DR-1S-6L-U0-V0-T15

## D. ADDITIONAL OBSERVATIONS FOR THE STRATIFIED $N$ -LAYER MODEL

Using the same problem parameters as in the previous example, we now consider the behavior of the perturbation at each layer as predicted by the model. Filled contour plots are constructed to measure the magnitude of perturbation for the layers  $L_1$  through  $L_6$ . All contours and color schemes are relative to the perturbation in  $L_6$ . In Figure 30, we see that the action for both the surface and bottom initiated events has affected all layers, but most of the energy transmitted by the wave “sinks” to the lower, denser layer  $L_6$ . This remains true at  $t = 15$  (Figure 31) at which time both events have passed through the truncated domain  $\Omega$ .

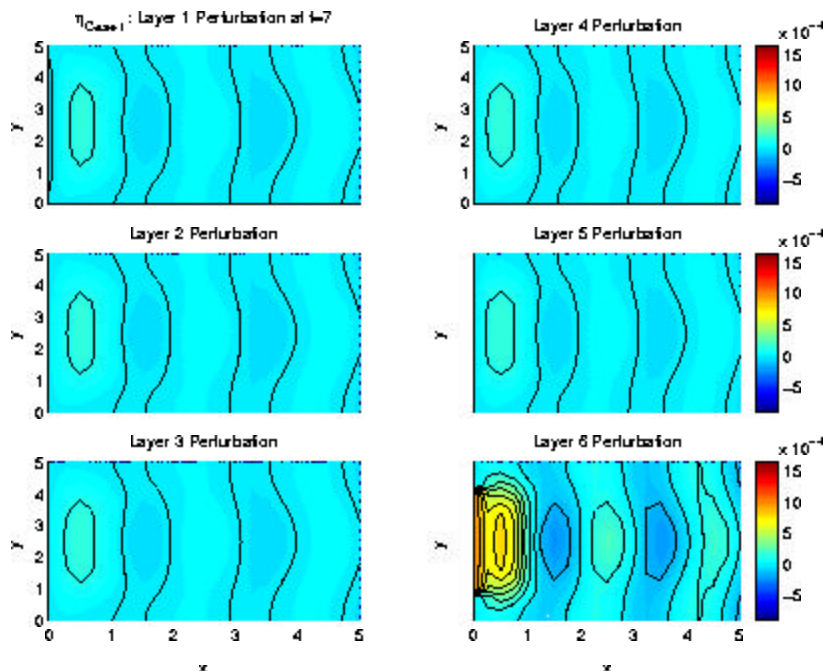


Figure 30. HNRBC-2DR-1S-6L-U0-V0-T07 Layer Perturbation Comparison

We further consider model predictions for the behavior of the perturbation at each layer interface. Recall that the disturbance at a layer interface is the sum of the disturbances of all layers below the interface. Filled contour plots are now constructed for the surface and the five layer interfaces using data obtained from

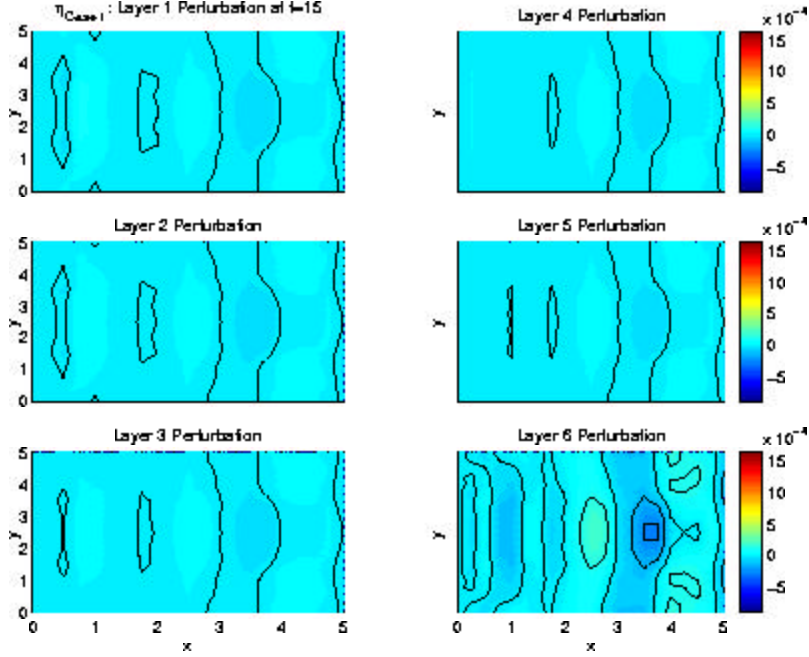


Figure 31. HNRBC-2DR-1S-6L-U0-V0-T15 Layer Perturbation Comparison

$\eta_{\text{case1}}$ . All contours and color schemes are relative to the total surface perturbation. The first comparison is again at  $t = 7$  (Figure 32). The contour plots reveal that the magnitude of the response to the surface event is damped with each successive layer interface downward. However, the wave appears to maintain its character at each layer interface as far as wave speed and geometric dispersion is concerned. We also note that the bottom layer event on the left side of the plot has immediately propagated to the surface. This is reasonable since the fluid is incompressible. However, as the wave propagates through  $\Omega$ , the effect on the lower layer interfaces once again dampens. At  $t = 15$ , the damping phenomenon in the lower layers is more pronounced (Figure 33). However, there is an exception on right side of the plot. In this regime, the perturbation is nearly zero and affected primarily by spurious reflection from  $\mathcal{B}$ . Differences in each layer's reflection may have caused this visible anomaly.

For a final comparison, we consider a six-layer, two-layer, and single-layer model. For this we set up the parameters for two-layer model as follows:  $\theta_i =$

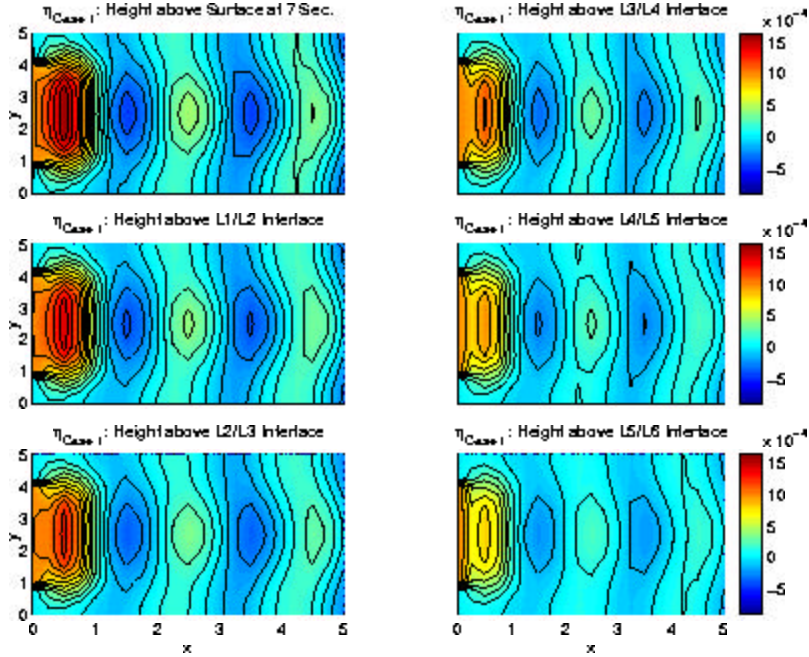


Figure 32. HNRBC-2DR-1S-6L-U0-V0-T07 Layer Interface Perturbation Comparison

$\{.05, .05\}$  and  $\rho_i = \{1.1, 1.25\}$ . Essentially we have combined the upper five layers of the six-layer model and used the average density for the first layer of the two-layer model. The second layer of the two-layer model is the same as the bottom layer of the six-layer model. The parameters for the single-layer model are  $\theta = .1$  and  $\rho = 1.175$  (note that from (V.19) we conclude that density is not a parameter in the single-layer model and therefore the value for  $\rho$  is irrelevant). The problem is again run for 15 time units, however the domain is extended to  $x = 15$  for each model and a  $60 \times 20$  mesh is used. This eliminates artificial boundary effects and comparisons can be made without concern for spurious reflection. All other parameters are the same. The results of the three models are presented for  $t = 15$  (Figure 34). Comparing the contours of the models reveal that the surface effect is reduced as the number of layers increases. Hence, the single-layer representation tends to over-predict surface wave action if the medium is stratified.

We now wish to apply the  $N$ -layer model to an ocean environment. However,

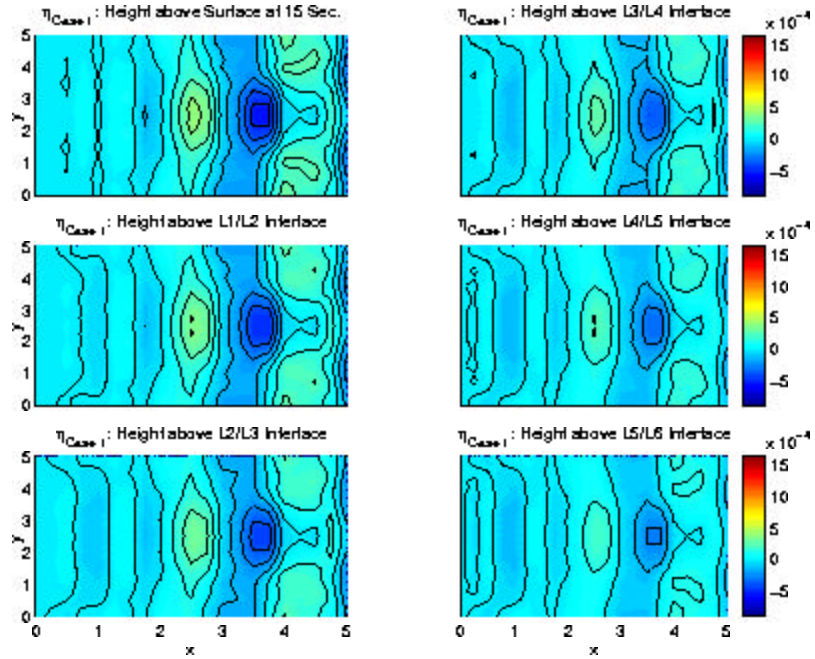


Figure 33. HNRBC-2DR-1S-6L-U0-V0-T15 Layer Interface Perturbation Comparison

before doing so, we must first extend the application of the Higdon NRBC to two dimensions. This will enable us to model a “patch of ocean” vice “a semi-infinite channel with hard walls”.

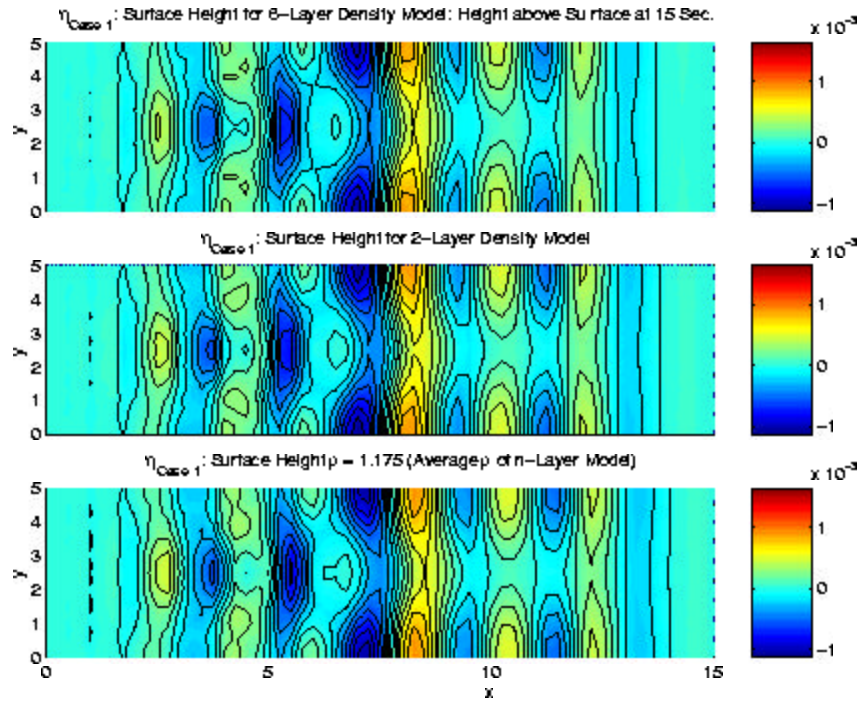


Figure 34. Model Comparison: HNRBC-2DR-1S-6L-U0-V0-T15 vs. HNRBC-2DR-1S-2L-U0-V0-T15 vs. HNRBC-2DR-1S-1L-U0-V0-T15

## VI. APPLYING HIGDON NRBC'S TO TWO OR MORE SIDES OF A TWO-DIMENSIONAL RECTANGULAR DOMAIN

The equations and concepts are now in place to construct finite domains in which Higdon NRBC's are imposed at two or more boundaries. In this chapter we employ the use of several examples to check the viability and the stability of schemes that utilize Higdon NRBC's on two and four sides of the single- and multi-layer models. Special attention is given to the corners where two Higdon boundaries intersect.

### A. EXAMPLE ONE: A TWO-DIMENSIONAL SINGLE-LAYER SCHEME WITH HIGDON NRBC'S ON TWO SIDES

For this example we employ a quarter plane shown in Figure 35. The semi-

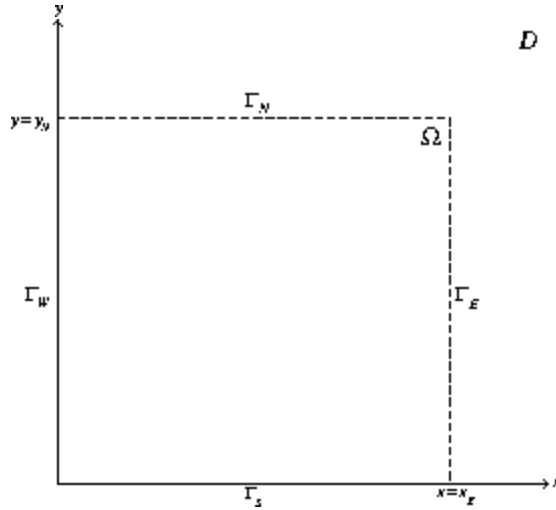


Figure 35. The Semi-Infinite Quarter-Plane

infinite domain  $\mathcal{D}$  is bounded by  $\Gamma_S$  and  $\Gamma_W$  and is represented by a  $10 \times 10$  square with a  $40 \times 40$  mesh. The truncated domain  $\Omega$  is a  $5 \times 5$  square with a  $20 \times 20$  mesh

and bounded by  $\Gamma_N$ ,  $\Gamma_S$ ,  $\Gamma_E$ , and  $\Gamma_W$ . On both domains  $\Delta x = .25$ ,  $\Delta y = .25$ , and  $\Delta t = .025$ . A gravitational parameter  $g = 10$  and a dispersion parameter  $f = .5$  is used. A single-layer non-stratified medium with a thickness of  $d = 0.1$  is considered. The problem is run for 15 time steps.

The specification for the Higdon NRBC on  $\Gamma_N$  is given by:

$$\prod_{j=1}^J \left( \frac{\partial}{\partial t} + C_j \frac{\partial}{\partial y} \right) \eta = 0. \quad (\text{VI.1})$$

This equation is the  $y$ -direction analog of (IV.9) which was used to describe the Higdon condition for  $\Gamma_E$ . A discussion equivalent to that in Section III.C applies in discretizing (VI.1). If  $\Delta x = \Delta y$  on the specified grid, and the same  $C_j$ 's are used for each boundary, then the parameters and operators used to discretize the  $\Gamma_E$  boundary condition may also be used to discretize the  $\Gamma_N$  boundary condition. To complete problem description, a Neumann condition is imposed at  $\Gamma_S$  and given by:

$$\frac{\partial \eta}{\partial y} = 0,$$

and a boundary function is imposed on  $\Gamma_W$  and is given by:

$$\eta_w(y, t) = \begin{cases} \sum_{m=1}^3 A_m \cos\left(\frac{n_m \pi (y - 1.875)}{3.75}\right) \sin(\omega_m t) & \text{if } y \leq 3.75, \\ 0 & \text{otherwise,} \end{cases} \quad (\text{VI.2})$$

where the parameters  $A_m$ ,  $n_m$ , and  $\omega_m$  are selected a priori as follows:

$$\begin{aligned} A_m &= .001, \quad .002, \quad .001: \\ n_m &= 1, \quad 3, \quad 1: \\ \omega_m &= .81, \quad 1.37, \quad 1.68, \end{aligned} \quad (\text{VI.3})$$

The restriction  $y \leq 3.75$  is discussed in the next section. Homogeneous initial conditions apply.

A solution  $\eta_{ref}$  and  $\eta_{case1}$  is computed for  $\mathcal{D}$  and  $\Omega$  respectively. Filled contour plots are generated for each solution. In Figure 36, these solutions are reported at  $t = 3$ . The upper-right subplot displays the solution for  $\eta_{ref}$  on  $\mathcal{D}$ . The upper-left



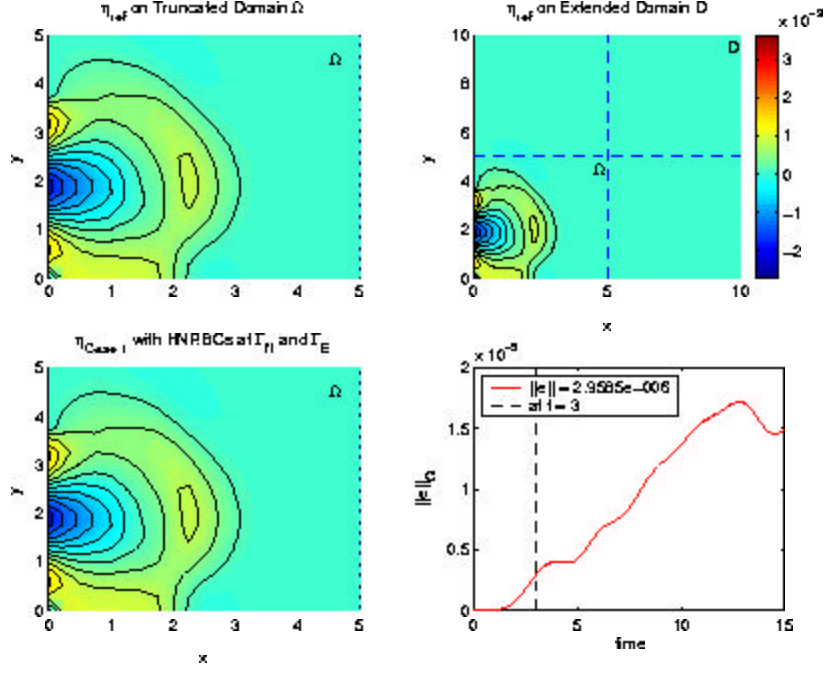


Figure 36. HNRBC-2DR-2S-1L-U0-V0-T03: Wave Pulse Passes through  $\Gamma_N$

subplot is a magnification of  $\eta_{ref}$  on the sub-domain  $\Omega$  and represents a solution on  $\Omega$  as if no boundaries were present at  $x = 5$  and  $y = 5$ . The lower-left subplot reports the solution for  $\eta_{case1}$  on  $\Omega$  where Higdon NRBC's are imposed at  $\Gamma_N$  and  $\Gamma_E$ . A qualitative comparison can be made between the two left-side subplots to determine the effectiveness of the NRBC in restricting the domain. A quantitative measurement of this comparison appears in the lower-right subplot, which reports an error measure  $\|e(t)\|_2$  (See IV.37). Note that for computational purposes, Higdon NRBC's with  $C_J = \{1, 1, 1, 1, 1, 1, 1\}$  are imposed at  $y = 10$  and  $x = 10$  on  $\mathcal{D}$ . Any reflection from these extended boundaries of  $\mathcal{D}$  will have little or no effect on the domain of interest  $\Omega$ .

In Figure 36 at  $t = 3$ , the wave pulse has reached  $\Gamma_N$ . A visual inspection reveals no discernible spurious reflection. The magnitude of the error measurement is within acceptable norms (i.e. less than the error due to the discretization).

At  $t = 5$  (Figure 37), the wave pulse has reached  $\Gamma_E$  and passes without visible

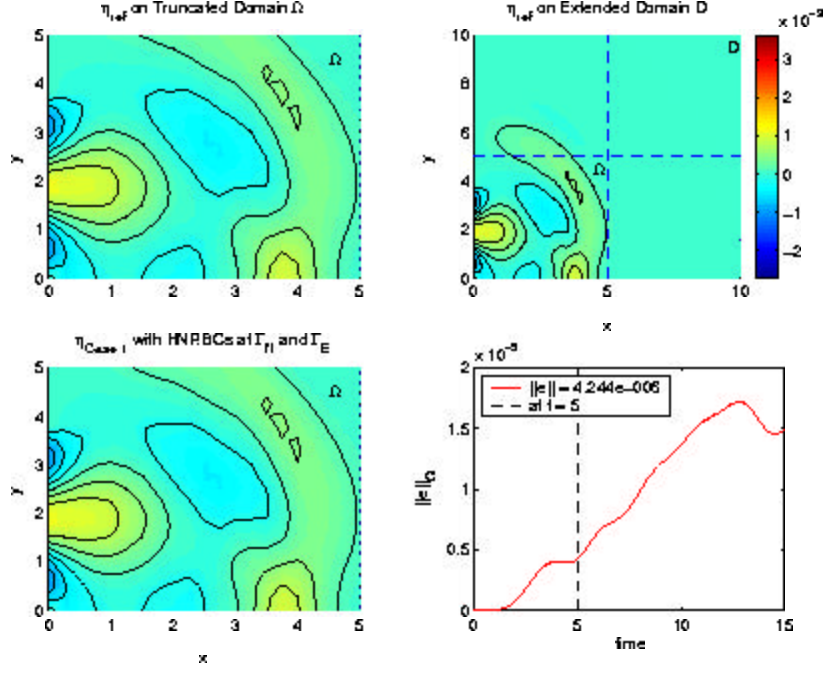


Figure 37. HNRBC-2DR-2S-1L-U0-V0-T05: Wave Pulse Passes through  $\Gamma_E$

reflection or undue increase in  $\|e(t)\|_n$ . Note that a leading edge of the pulse is about to reach the intersection of  $\Gamma_N$  and  $\Gamma_E$ . At  $t = 15$  (Figure 38), the wave has passed through the corner unimpeded with no adverse effect on  $\|e(t)\|_n$  and the two left-side subplots are similar with no visible differences. The measured error  $\|e(t)\|_n$  has stabilized at approximately  $2 \times 10^{-5}$ .

The corner, however, is still cause for concern, because two different ways to approximate the Higdon boundary grid points are possible. In the first method we initially evaluate the  $\Gamma_E$  grid points excluding the corner point. We then evaluate the  $\Gamma_N$  grid points including the corner point. Hence the corner point is evaluated based on boundary values calculated for  $\Gamma_E$ . This method was used in generating Figures 36 through 38. In a second method, the grid points for  $\Gamma_N$  (excluding the corner point) are fully evaluated first followed by the grid points of  $\Gamma_E$  (including the corner point). Now the corner point values are obtained from  $\Gamma_N$  boundary values. Regardless of the method used, the value of the corner point should be the same. This

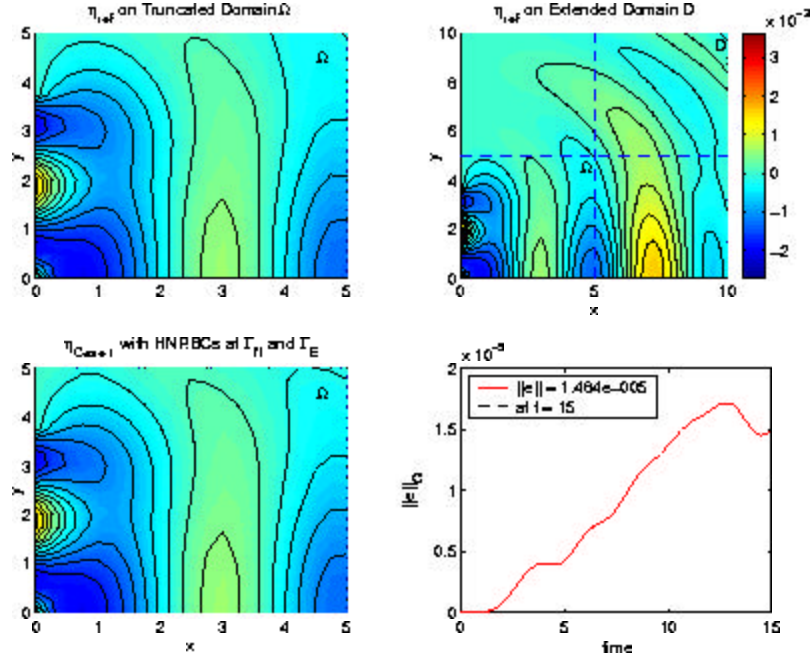


Figure 38. HNRBC-2DR-2S-1L-U0-V0-T15: Wave Pulse Passes through Corner

was tested and the results are compared via the error measurement plot in Figure 39. The figure indicates that the two solutions are exactly the same. Hence no special considerations must be given when handling corner points that are the intersection of the Higdon boundaries. However, one must be careful to ensure that the corner point is not evaluated twice when designing algorithms to compute these boundary values.

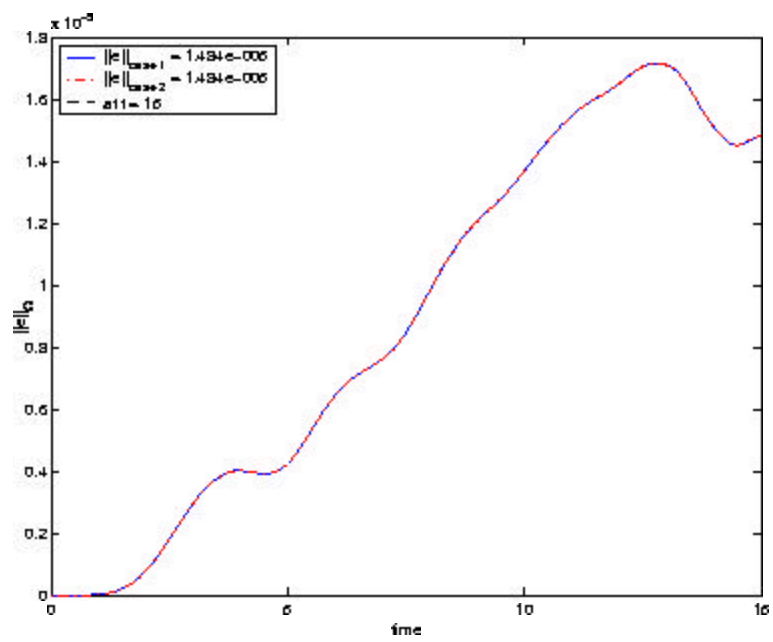


Figure 39. Corner Point Check: Two Approaches to Evaluating HNRBC Grid Points

## B. INSTABILITIES IN THE 2-D, 2-SIDED HIGDON NRBC SCHEME

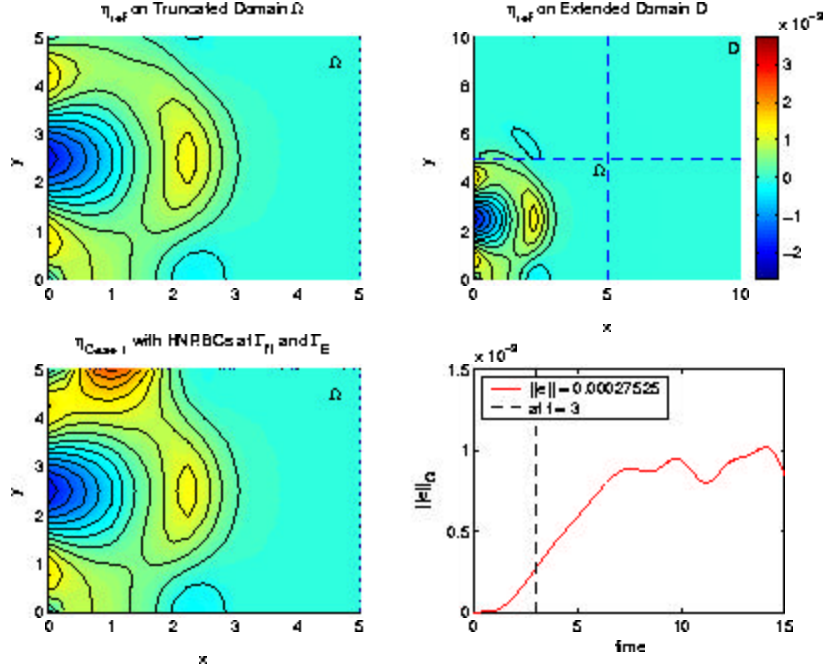


Figure 40. HNRBC-2DR-2S-1L-U0-V0-T03:  $\Gamma_N$  Instability with  $C_j = \{1, 1, 1, 1, 1\}$

Despite the heartening results of the previous example, a stability problem does emerge along the entire northern NRBC if a non-zero boundary function  $\eta_W$  is extended to  $\Gamma_N$ . Recall the constraint  $y \leq 3.75$  in (VI.4). This was specified in order to set up a buffer consisting of five zero valued grid points between the boundary function in the northern Higdon boundary. If this is not done, the boundary instability occurs and propagates through  $\Omega$ . For example, define the boundary function at  $\Gamma_W$  as:

$$\eta_W(y, t) = \sum_{m=1}^3 A_m \cos\left(\frac{n_m \pi (y - 2.5)}{5}\right) \sin(\omega_m t) \quad (\text{VI.4})$$

The grid point at  $y = 5$  is immediately adjacent to  $\Gamma_N$ . All other parameters with regards to the previous example remaining unchanged. The problem is run with  $J = 5$  and  $C_j = \{1, 1, 1, 1, 1\}$ . In Figure 40 at  $t = 3$ , we discern turbulence in the upper

left-hand corner of  $\Omega$  for  $\eta_{case1}$ . In Figure 41 at  $t = 10$ , we see that the instability has propagated through  $\Omega$ .

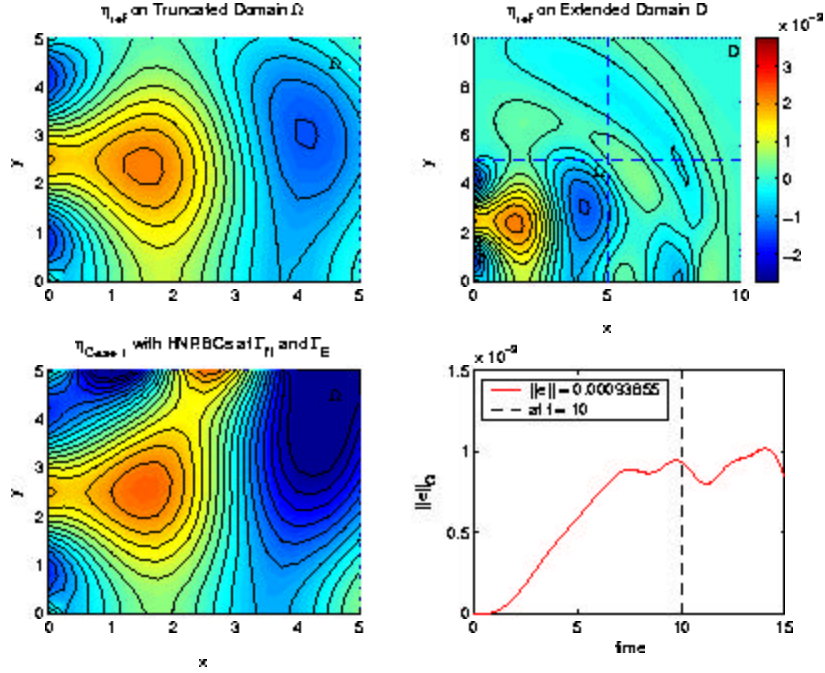


Figure 41. HNRBC-2DR-2S-1L-U0-V0-T10:  $\Gamma_N$  Instability with  $C_j = \{1, 1, 1, 1, 1\}$

To explain the unstable behavior, recall that the 5<sup>th</sup>-order Higdon NRBC on  $\Gamma_N$  is constructed with up to 5<sup>th</sup>-order derivatives with respect to  $y$  and  $t$ . Using the backward-difference method to construct the discretized forms of these derivatives requires that we reach back as many as five grid points both temporally and spatially. During the initial time-stepping sequence, we only have a history of one time step. The current algorithm uses a default of zero if the discretization calls for data at a time that is less than zero. This is a poor estimate if the initial condition is some non-zero value because it introduces a discontinuity in time. The problem corrects itself somewhat if a Sommerfeld condition ( $J = 1$  and  $C_j = \{1\}$ ) is utilized on  $\Gamma_N$  as in Figure 42. However, our goal is to use high-order Higdon conditions to increase the accuracy of the estimate. Experimentation showed that a buffer of  $J$  grid points is necessary to achieve stability for a  $J^{\text{th}}$ -order Higdon-NRBC. The exact nature of

the instability must be further investigated. However, for the time being we continue to present examples while maintaining the required buffer zone to achieve stability. This is one of the reasons Givoli and Neta introduced auxiliary variables [Ref. 24]. See also Givoli et al [Ref. 26].

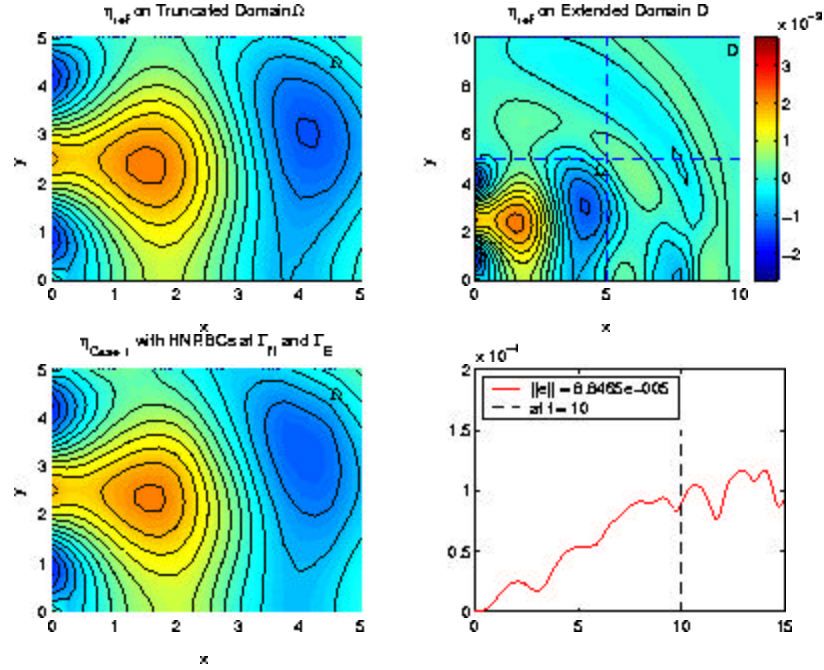


Figure 42. HNRBC-2DR-2S-1L-U0-V0-T10: Mitigation of Instability using Sommerfeld Condition ( $J = 1$  and  $C_j = \{1\}$ )

### C. EXAMPLE TWO: A TWO-DIMENSIONAL MULTI-LAYER STRATIFIED SCHEME WITH HIGDON NRBC'S ON TWO SIDES

In this section we check the compatibility of the two-sided Higdon model with the multi-layer stratification model presented in Chapter 5. This example will again use the semi-infinite quarter-plane (Figure 35) and the same domain specification as used in Example 1 of this chapter. The stratified medium is modeled with six layers. The layer thicknesses from top to bottom are  $\theta_i = \{.01, .01, .01, .01, .01, .05\}$ . The density for each layer is given by  $\rho_i = \{1, 1.05, 1.1, 1.15, 1.2, 1.25\}$ . A gravitational parameter  $g = 10$  and a dispersion parameter  $f = .5$  is used.

The boundary function  $\eta_w$  on  $\Gamma_w$  is stipulated to simulate two geophysical events. A surface disturbance akin to the wind is initiated in  $L_1$ . Using the function:

$$f_1(y, t) = \sum_{m=1}^3 A_m \cos\left(\frac{n_m \pi(y - 1.875)}{3.75}\right) \sin(\omega_m t), \quad (\text{VI.5})$$

we let:

$$\eta_{w_1}(y, t) = \begin{cases} f_1(y, t) & \text{if } t \leq 12.5 \text{ \& } y \leq 3.75, \\ 0 & \text{otherwise} \end{cases} \quad (\text{VI.6})$$

where  $A_m$ ,  $n_m$ , and  $\omega_m$  are given by (VI.3). A second disturbance, simulating seismic activity on the ocean floor, is initiated in the  $L_6$  using the function:

$$f_2(y, t) = .001 \cos\left(\frac{\pi(y - 1.875)}{1.75}\right) \cos\left(\frac{\pi(t - 6.5)}{3}\right), \quad (\text{VI.7})$$

and letting:

$$\eta_{w_6}(y, t) = \begin{cases} f_2(y, t) & \text{if } 5 \leq t \leq 8 \text{ \& } 1 \leq y \leq 2.75, \\ 0 & \text{otherwise} \end{cases} \quad (\text{VI.8})$$

All other values for  $\eta_{w_i}$  are zero. The simulation is run for 15 time units and results are reported using a similar presentation as that used in Example 1.

At  $t = 6$  (Figure 43), the surface effect has passed through  $\Gamma_N$  and  $\Gamma_E$  and  $\|e(t)\|_\Omega$  at the surface falls within acceptable tolerances. The effects of the bottom disturbance are readily visible near the west boundary. At  $t = 15$  (Figure 44), the bottom disturbance has propagated through  $\Omega$  and has successfully passed through



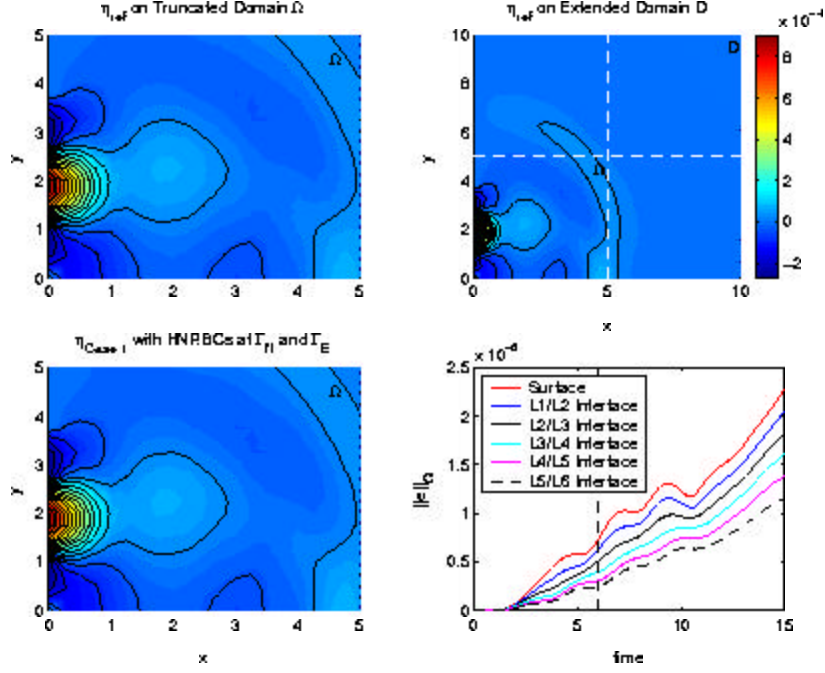


Figure 43. HNRBC-2DR-2S-6L-U0-V0-T06 with  $J = 5$  and  $C_j = \{1, 1, 1, 1, 1\}$  for each Layer

both artificial boundaries. Some differences between  $\eta_{ref}$  and  $\eta_{case1}$  are visible, but again, the error measure  $\|e(t)\|_\Omega$  is less than the discretization error. From this example, we conclude that the multi-layer stratification model will work effectively when Higdon NRBC's are placed on two-sides of the domain  $\Omega$ .

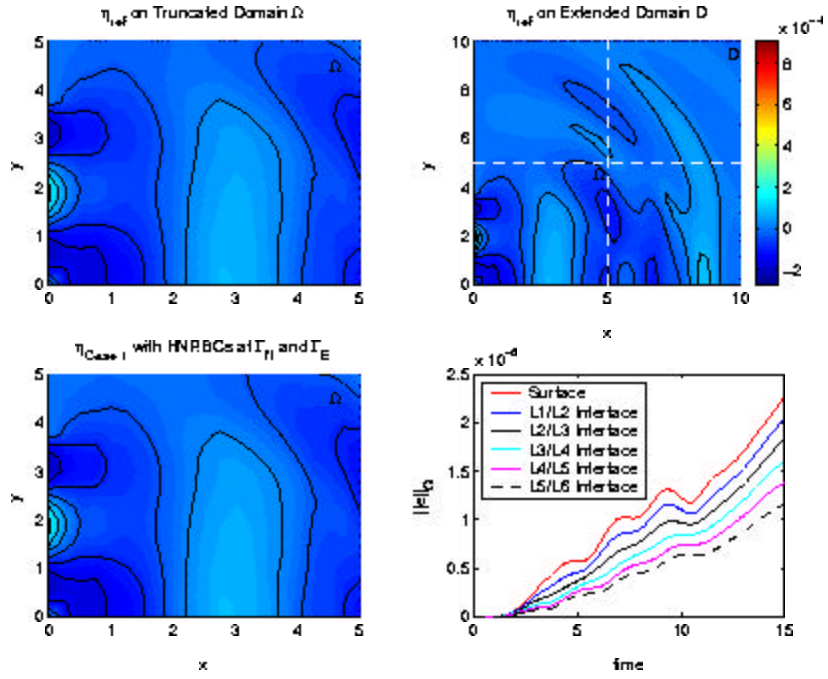


Figure 44. HNRBC-2DR-2S-6L-U0-V0-T15 with  $J = 5$  and  $C_j = \{1, 1, 1, 1, 1\}$  for each Layer

## D. EXAMPLE FOUR: A TWO-DIMENSIONAL MULTI-LAYER STRATIFIED SCHEME WITH HIGDON NRBC'S ON FOUR SIDES

In this example we consider a truncated domain  $\Omega$  where Higdon NRBC's are imposed on four sides. The boundary conditions on  $\Gamma_N$  and  $\Gamma_E$  are discretized as before. The boundary conditions on  $\Gamma_S$  and  $\Gamma_W$  are discretized in a similar manner (see Section III.C), however forward- vice backward-difference equations are used in approximating the spatial derivatives. As before,  $\Omega$  is a  $5 \times 5$  square with a  $20 \times 20$  mesh. Higdon NRBC's are located at  $x = 0$ ,  $y = 0$ ,  $x = 5$ , and  $y = 5$  with  $C_j = \{1, 1, 1, 1, 1\}$  at each boundary.

The extended domain  $\mathcal{D}$  is the infinite plane. It is represented by a  $15 \times 15$  square with a  $60 \times 60$  mesh. The domain of interest  $\Omega$  is located in the center of  $\mathcal{D}$  at  $5 \leq x, y \leq 10$ . Higdon boundaries are placed at  $x = 0$ ,  $y = 0$ ,  $x = 15$ , and  $y = 15$  with  $C_j = \{1, 1, 1, 1, 1, 1, 1\}$  at each boundary. This is done for computational purposes only and any spurious reflection from these extended boundaries will not significantly pollute the domain of interest. On both domains  $\Delta x = \Delta y = .25$  and the time-step  $\Delta t = .0125$ . A gravitation parameter of  $g = 10$  and a dispersion parameter of  $f = .5$  is used. The layer thicknesses are  $\theta_i = \{.01, .01, .01, .01, .01, .05\}$  with respective densities given by  $\rho_i = \{1, 1.05, 1.1, 1.15, 1.2, 1.25\}$ .

Random values that represent physical disturbances in  $\Omega$  are introduced at designated times at specified  $x$ - and  $y$ -ranges in specified layers. At the given time, these random values are added to existing values of  $\eta$  in the designated layer. The dispersive mechanism defined by (II.88) is then allowed to act on the event. These random events are sufficiently complex in nature and “flex” the Higdon NRBC's exposing any unacceptable spurious reflection.

For this example two separate disturbances or events are imposed. Event 1 is a surface event given by:

$$S_{L_1}^{t=.025} = \begin{cases} .0001 * rand(-.5, .5) & \text{if } 1.5 \leq x, y \leq 3.5, \\ 0 & \text{otherwise} \end{cases} \quad (\text{VI.9})$$

where  $S_{L_1}^{t=.025}(x, y)$  represents a disturbance initiated in the first layer  $L_1$  at  $t = .025$  and  $rand(-.5, .5)$  is a random number on the interval  $[-.5, .5]$ . Event 2 is a bottom event given by:

$$S_{L_6}^{t=5} = \begin{cases} .00015 * rand(-.25, .75) & \text{if } 1.5 \leq x \leq 2.25 \text{ \& } 1.5 \leq y \leq 3.5, \\ 0 & \text{otherwise.} \end{cases} \quad (\text{VI.10})$$

where  $S_{L_6}^{t=5}(x, y)$  indicates that the event was initiated in  $L_6$  at  $t = 5$ . The maximum amplitude of each event is set to be a small fraction of the total thickness of the layer in which it is initiated, thus maintaining the integrity of the perturbation analysis that was utilized to derive the Klein-Gordon equation. A buffer of at least 5 zero-valued grid points was maintained between the NRBC and the event acknowledging the stability considerations discussed in Section VI.C. All events must be shifted 5 units in the  $x$ - and  $y$ -directions when initiating activity on  $\mathcal{D}$ , in order to properly place them in the domain's center. The random seed for these events are preserved for use in later examples.

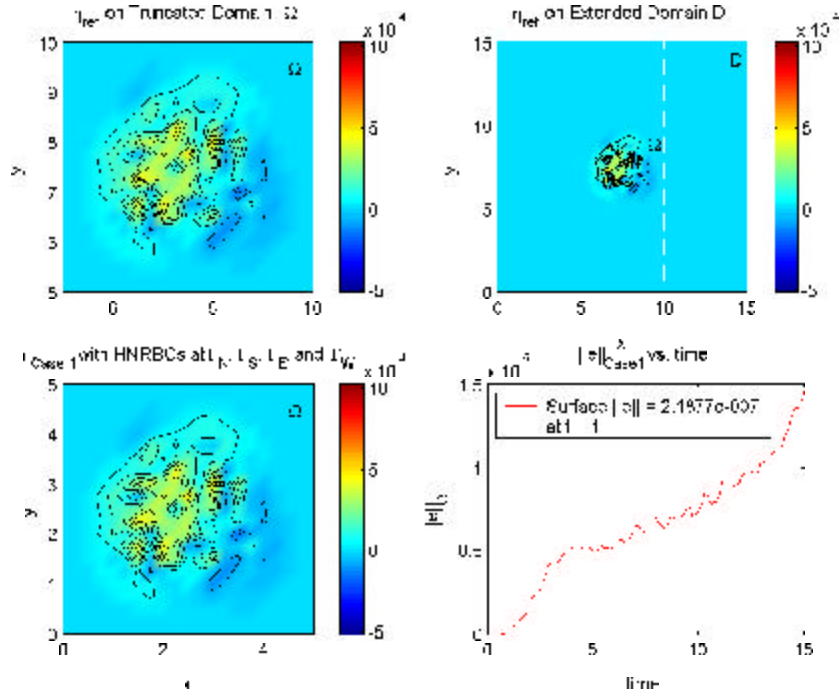


Figure 45. HNRBC-2DR-4S-6L-U0-V0-T01: Surface Disturbance Initiated.

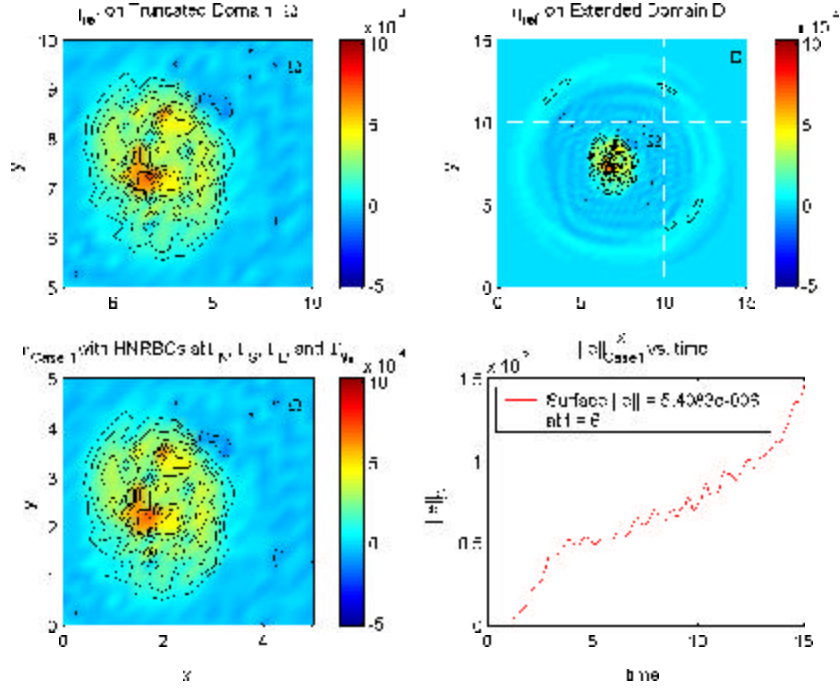


Figure 46. HNRBC-2DR-4S-6L-U0-V0-T06: Surface Disturbance has Left  $\Omega$ . Bottom Disturbance Initiated.

A trial is run for 15 time units. At  $t = 1$  (Figure 45), the surface event has been initiated and the resulting waves are propagating toward the four sides of  $\Omega$ . The error measurement  $\|e(t)\|_{\Omega}$  is near zero. At  $t = 6$  (Figure 46), the surface event has left  $\Omega$  with no significant spurious reflection at either the boundaries or the corners. Additionally, the bottom event has been initiated and is now propagating outward in  $\Omega$ . At  $t = 13$  (Figure 47), both events have passed through the artificial boundary successfully. An outward radiating wave front can be seen in the upper-right subplot of the extended domain  $\mathcal{D}$ . The left-side sub-plots are remarkably similar indicating that the boundary conditions are suitable for the layered problem. At  $t = 15$  (Figure 48), the wave energy resulting from the disturbances have left  $\Omega$ . The effect due to spurious reflection starts to become significant thus increasing  $\|e(t)\|_{\Omega}$ .

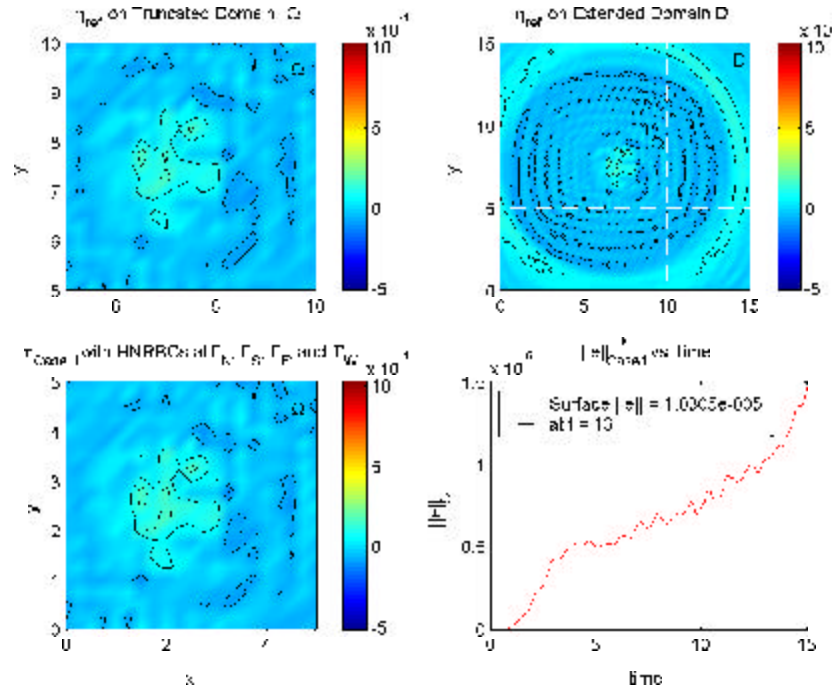


Figure 47. HNRBC-2DR-4S-6L-U0-V0-T13: All Events have Passed through HNRBC's.

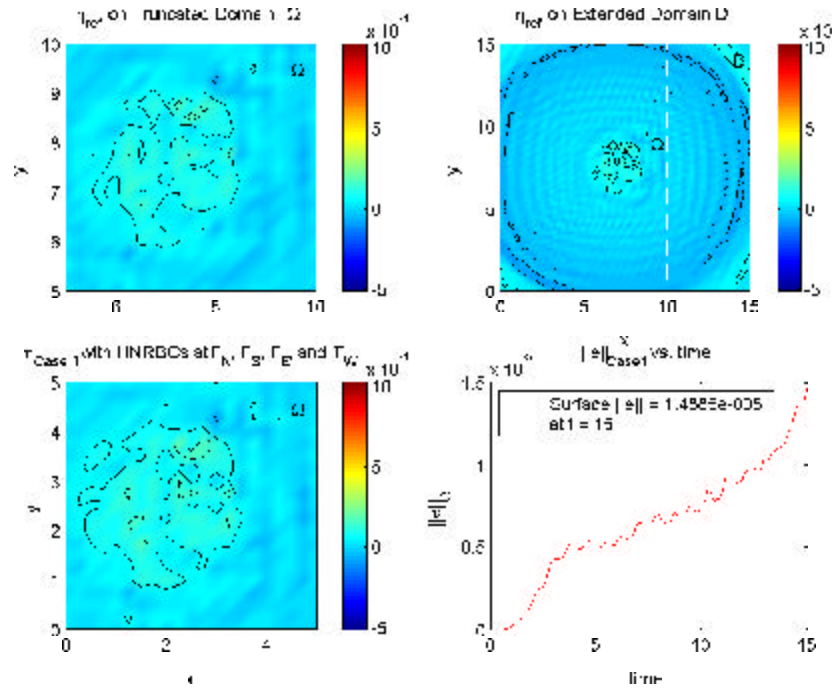


Figure 48. HNRBC-2DR-4S-6L-U0-V0-T15: Spurious Reflection Predominates in  $\Omega$ .

## VII. LINEARIZED SHALLOW WATER EQUATIONS WITH NON-ZERO ADVECTION

In this chapter the linearized shallow-water model is further developed by lifting the zero-advection requirement. Recall the linearized form of the shallow water model is described by (II.77 and II.79):

$$\begin{aligned}\frac{\partial u^*}{\partial t} + U \frac{\partial u^*}{\partial x} + V \frac{\partial u^*}{\partial y} - f(V + v^*) &= -g \left( \frac{\partial h_B}{\partial x} + \frac{\partial H_0}{\partial x} + \frac{\partial \eta}{\partial x} \right), \\ \frac{\partial v^*}{\partial t} + U \frac{\partial v^*}{\partial x} + V \frac{\partial v^*}{\partial y} + f(U + u^*) &= -g \left( \frac{\partial h_B}{\partial y} + \frac{\partial H_0}{\partial y} + \frac{\partial \eta}{\partial y} \right), \\ \frac{\partial \eta}{\partial t} + U \frac{\partial \eta}{\partial x} + V \frac{\partial \eta}{\partial y} + H_0 \left( \frac{\partial u^*}{\partial x} + \frac{\partial v^*}{\partial y} \right) &= 0,\end{aligned}\tag{VII.1}$$

where  $U$  and  $V$  are constant advection terms in the  $x$ - and  $y$ -directions respectively. As per discussion in Section II.B.3, if the bottom contour  $h_B$  is flat, then  $H_0$  is constant. This allows simplification of (VII.1) to:

$$\begin{aligned}\frac{\partial u^*}{\partial t} + U \frac{\partial u^*}{\partial x} + V \frac{\partial u^*}{\partial y} - f(V + v^*) &= -g \frac{\partial \eta}{\partial x}, \\ \frac{\partial v^*}{\partial t} + U \frac{\partial v^*}{\partial x} + V \frac{\partial v^*}{\partial y} + f(U + u^*) &= -g \frac{\partial \eta}{\partial y}, \\ \frac{\partial \eta}{\partial t} + U \frac{\partial \eta}{\partial x} + V \frac{\partial \eta}{\partial y} + H_0 \left( \frac{\partial u^*}{\partial x} + \frac{\partial v^*}{\partial y} \right) &= 0.\end{aligned}\tag{VII.2}$$

Now define the operator:

$$\frac{D}{Dt} = \frac{\partial}{\partial t} + U \frac{\partial}{\partial x} + V \frac{\partial}{\partial y}.\tag{VII.3}$$

Substituting this into (VII.2) yields:

$$\begin{aligned}\frac{D}{Dt}(u^*) - fv^* - fV &= -g\frac{\partial\eta}{\partial x}, \\ \frac{D}{Dt}(v^*) + fu^* + fU &= -g\frac{\partial\eta}{\partial y}, \\ \frac{D}{Dt}(\eta) + H_0\left(\frac{\partial u^*}{\partial x} + \frac{\partial v^*}{\partial y}\right) &= 0,\end{aligned}\tag{VII.4}$$

where  $fV$  and  $fU$  are constant products of the Coriolis parameter and the advection components. Note that this is analogous to the zero-advection form of the shallow water equation given by (II.78) and (II.80) with  $\frac{D}{Dt}$  replacing  $\frac{\partial}{\partial t}$ . Equation (VII.4) is combined into a single form using the same steps delineated in Section II.B.9. The result is:

$$\frac{D}{Dt}\left(\frac{D^2}{Dt^2}(\eta) - C_0^2\nabla^2\eta + f^2\eta\right) = 0,\tag{VII.5}$$

where  $C_0 = \sqrt{gH_0}$ . This is the Klein-Gordon form of the linearized shallow water equation with non-zero advection. This can be rewritten as:

$$\frac{D^2}{Dt^2}(\eta) - C_0^2\nabla^2\eta + f^2\eta = S(x, y, t),\tag{VII.6}$$

such that:

$$\frac{D}{Dt}(S(x, y, t)) = \frac{\partial S}{\partial t} + U\frac{\partial S}{\partial x} + V\frac{\partial S}{\partial y} = 0.\tag{VII.7}$$

We shall consider (VII.6) in its homogeneous form:

$$\frac{D^2}{Dt^2}(\eta) - C_0^2\nabla^2\eta + f^2\eta = 0.\tag{VII.8}$$

Applying the operator listed in (VII.3) twice yields:

$$\frac{D^2}{Dt^2} = \frac{\partial^2}{\partial t^2} + U^2\frac{\partial^2}{\partial x^2} + V^2\frac{\partial^2}{\partial y^2} + 2U\frac{\partial^2}{\partial x\partial t} + 2V\frac{\partial^2}{\partial y\partial t} + 2UV\frac{\partial^2}{\partial x\partial y}\tag{VII.9}$$



Substituting this into (VII.8) yields:

$$\boxed{\begin{aligned} & \frac{\partial^2 \eta}{\partial t^2} + (U^2 - C_0^2) \frac{\partial^2 \eta}{\partial x^2} + (V^2 - C_0^2) \frac{\partial^2 \eta}{\partial y^2} \\ & + 2U \frac{\partial^2 \eta}{\partial x \partial t} + 2V \frac{\partial^2 \eta}{\partial y \partial t} + 2UV \frac{\partial^2 \eta}{\partial x \partial y} + f^2 \eta = 0. \end{aligned}} \quad (\text{VII.10})$$

This is an expanded Klein-Gordon equivalent for the linearized shallow water equations with non-zero advection terms  $U$  and  $V$ . It applies to a single-layer model, but will later be extended to the  $N$ -layer stratified model.

## A. DISCRETIZING THE LINEARIZED SWE WITH CONSTANT NON-ZERO ADVECTION TERMS

The following central-difference approximations are used to discretize (VII.10):

$$\begin{aligned} \eta_{xx} &= \frac{\eta_{p+1,q}^n - 2\eta_{pq}^n + \eta_{p-1,q}^n}{\Delta x^2} + O(\Delta x^2) \\ \eta_{xy} &= \frac{\eta_{p+1,q+1}^n - \eta_{p+1,q-1}^n - \eta_{p-1,q+1}^n + \eta_{p-1,q-1}^n}{4\Delta x \Delta y} + O(\Delta x^2, \Delta y^2). \end{aligned} \quad (\text{VII.11})$$

Analogous forms are used for approximating  $\eta_{yy}$ ,  $\eta_{tt}$ ,  $\eta_{xt}$  and  $\eta_{yt}$ . Substituting these into (VII.10) yields:

$$\begin{aligned} & \frac{1}{\Delta t^2} (\eta_{pq}^{n+1} - 2\eta_{pq}^n + \eta_{pq}^{n-1}) + \frac{(U^2 - C_0^2)}{\Delta x^2} (\eta_{p+1,q}^n - 2\eta_{pq}^n + \eta_{p-1,q}^n) \\ & + \frac{(V^2 - C_0^2)}{\Delta y^2} (\eta_{p,q+1}^n - 2\eta_{pq}^n + \eta_{p,q-1}^n) \\ & + \frac{U}{2\Delta x \Delta t} (\eta_{p+1,q}^{n+1} - \eta_{p+1,q}^{n-1} - \eta_{p-1,q}^{n+1} + \eta_{p-1,q}^{n-1}) \\ & + \frac{V}{2\Delta y \Delta t} (\eta_{p,q+1}^{n+1} - \eta_{p,q+1}^{n-1} - \eta_{p,q-1}^{n+1} + \eta_{p,q-1}^{n-1}) \\ & + \frac{UV}{2\Delta x \Delta y} (\eta_{p+1,q+1}^n - \eta_{p+1,q-1}^n - \eta_{p-1,q+1}^n + \eta_{p-1,q-1}^n) + f^2 \eta_{pq}^n = 0. \end{aligned} \quad (\text{VII.12})$$

This is the discrete form of the linear shallow water equation with non-zero advection terms. Terms that contain an  $n + 1$  superscript are unknown  $\eta$  values which must be solved. Making the following substitutions:

$$A = \frac{1}{\Delta t^2}, \quad B = \frac{(U^2 - C_0^2)}{\Delta x^2}, \quad C = \frac{(V^2 - C_0^2)}{\Delta y^2} \quad (\text{VII.13})$$

$$D = \frac{U}{2\Delta x \Delta t}, \quad E = \frac{V}{2\Delta y \Delta t}, \quad F = \frac{UV}{2\Delta x \Delta y},$$

and moving known terms to the right side of (VII.12) yields:

$$A\eta_{p,q}^{n+1} + D\eta_{p+1,q}^{n+1} - D\eta_{p-1,q}^{n+1} + E\eta_{p,q+1}^{n+1} - E\eta_{p,q-1}^{n+1} =$$

$$(2A + 2B + 2C - f^2)\eta_{p,q}^n - A\eta_{p,q}^{n-1} - B(\eta_{p+1,q}^n + \eta_{p-1,q}^n) \quad (\text{VII.14})$$

$$- C(\eta_{p,q+1}^n + \eta_{p,q-1}^n) + D(\eta_{p+1,q}^{n-1} - \eta_{p-1,q}^{n-1}) + E(\eta_{p,q+1}^{n-1} - \eta_{p,q-1}^{n-1})$$

$$- F(\eta_{p+1,q+1}^n - \eta_{p+1,q-1}^n - \eta_{p-1,q+1}^n + \eta_{p-1,q-1}^n).$$

Since there are five unknowns, (VII.14) must be solved implicitly. A system of  $N$  equations with  $N$  unknowns is set up where  $N$  is the total number of grid points. To make the indices compatible with those used in the discretized form of the Higdon NRBC (see Sections IV.C and IV.D) we replace  $n$  with  $n - 1$ . This yields:

$$A\eta_{p,q}^n + D\eta_{p+1,q}^n - D\eta_{p-1,q}^n + E\eta_{p,q+1}^n - E\eta_{p,q-1}^n =$$

$$(2A + 2B + 2C - f^2)\eta_{p,q}^{n-1} - A\eta_{p,q}^{n-2} - B(\eta_{p+1,q}^{n-1} + \eta_{p-1,q}^{n-1})$$

$$- C(\eta_{p,q+1}^{n-1} + \eta_{p,q-1}^{n-1}) + D(\eta_{p+1,q}^{n-2} - \eta_{p-1,q}^{n-2}) + E(\eta_{p,q+1}^{n-2} - \eta_{p,q-1}^{n-2})$$

$$- F(\eta_{p+1,q+1}^{n-1} - \eta_{p+1,q-1}^{n-1} - \eta_{p-1,q+1}^{n-1} + \eta_{p-1,q-1}^{n-1}).$$

(VII.15)

The Higdon NRBC (III.4) is now applied to the boundaries of the problem. The unknowns in the discretized form of Higdon NRBC (IV.19) are those terms whose

operator  $P_m$  does not contain a time shift  $S_t^-$ . For example, consider the discretized form of a Higdon NRBC with order  $J = 2$  on the eastern boundary (IV.18):

$$\begin{aligned} & [a_1 a_2 + a_1 d_2 S_t^- + a_1 e_2 S_x^- + d_1 a_2 S_t^- + d_1 d_2 S_t^{-2} \\ & + d_1 e_2 S_t^- S_x^- + e_1 a_2 S_x^- + e_1 d_2 S_t^- S_x^- + e_1 e_2 S_x^{-2}] \eta_{E,q}^n = 0. \end{aligned} \quad (\text{VII.16})$$

Shifting the known quantities, e.g. all terms with time shift operators, to the right side of (VII.16) yields:

$$\begin{aligned} & [a_1 a_2 + a_1 e_2 S_x^- + e_1 a_2 S_x^- + e_1 e_2 S_x^{-2}] \eta_{E,q}^n = \\ & - [a_1 d_2 S_t^- + d_1 a_2 S_t^- + d_1 d_2 S_t^{-2} + d_1 e_2 S_t^- S_x^- + e_1 d_2 S_t^- S_x^-] \eta_{E,q}^n, \end{aligned} \quad (\text{VII.17})$$

or in alternate form:

$$\begin{aligned} & a_1 a_2 \eta_{E,q}^n + (a_1 e_2 + e_1 a_2) \eta_{E-1,q}^n + e_1 e_2 \eta_{E-2,q}^n = \\ & - (a_1 d_2 + d_1 a_2) \eta_{E,q}^{n-1} - (d_1 e_2 + e_1 d_2) \eta_{E-1,q}^{n-1} - d_1 d_2 \eta_{E,q}^{n-2}. \end{aligned} \quad (\text{VII.18})$$

In general, the number of unknowns in a  $J^{\text{th}}$ -order Higdon NRBC using first-order difference approximations is  $J + 1$ . The number of unknowns in a  $J^{\text{th}}$ -order Higdon NRBC using second-order difference approximations is  $2J + 1$ . Equation (VII.15) together with an analogous form of (VII.18), adjusted for the Higdon order  $J$ , is used to set up the system of equations that will be solved to “time-step” the system.

## B. NUMERICAL EXAMPLE: TWO-DIMENSIONAL SINGLE-LAYER SCHEME WITH HIGDON NRBC’S ON FOUR SIDES WITH NON-ZERO ADVECTION

In this example, the truncated domain  $\Omega$  as described in Section VI.D with Higdon NRBC’s on four sides is used. As before, the extended domain  $\mathcal{D}$  is an infinite plane represented by a  $15 \times 15$  square with a  $60 \times 60$  mesh.  $\Omega$  is located in the center of  $\mathcal{D}$  at  $5 \leq x, y \leq 10$ . Higdon boundaries are also imposed on  $\mathcal{D}$  for computational purposes. Spurious reflection from these boundaries should not significantly pollute

$\Omega$ . On both domains  $\Delta x = \Delta y = .25$  and  $\Delta t = .0125$ . A gravitation parameter of  $g = 10$ , dispersion parameter of  $f = .5$ , and a single layer of thickness  $\Theta = .1$  with density  $\rho = 1$  is used. Advection constants of  $U = .5$  and  $V = -.25$  are utilized.

Physical disturbances in  $\Omega$  are initiated via two separate events. Event 1 is given by:

$$S^{t=.025} = \begin{cases} .0001 * rand(-.5, .5) & \text{if } 1.5 \leq x, y \leq 3.5, \\ 0 & \text{otherwise} \end{cases} \quad (\text{VII.19})$$

where  $S^{t=.025}(x, y)$  represents a disturbance initiated at  $t = .025$  and  $rand(-.5, .5)$  is a random number on the interval  $[-.5, .5]$ . Event 2 is given by:

$$S^{t=5} = \begin{cases} .000015 * rand(-.25, .75) & \text{if } 1.5 \leq x \leq 2.25 \text{ \& } 1.5 \leq y \leq 3.5, \\ 0 & \text{otherwise.} \end{cases} \quad (\text{VII.20})$$

where  $S^{t=5}(x, y)$  represents a disturbance initiated at  $t = 5$  and  $rand(-.25, .75)$  is a random number on the interval  $[-.25, .75]$ . Note that these events are analogous to the events described in Section VI.D. The random seed was preserved so that the same values would be generated for each event. A buffer of at least 5 zero-valued grid points was maintained between the NRBC and each event for stability purposes. The events are shifted 5 units in the positive  $x$ - and  $y$ -directions on  $\mathcal{D}$  in order to properly place them in the domain's center.

Before running an example, consideration was given to the selection of  $C_j$ 's. Several experiments were conducted with results reported in Figure 49. Initially, a Higdon NRBC with order  $J = 5$  and  $C_j = \{C_0, C_0, C_0, C_0, C_0\}$  where  $C_0 = \sqrt{g\Theta} = 1$  was considered. This was compared to a case where the  $C_j$ 's are corrected for advection. The predominate speed of the gravity wave is  $C_0$ . This is affected somewhat the dispersion and wave height. However, with the inclusion of advection, the predominate wave speed with respect to each boundary is affected more significantly. Therefore the  $C_j$ 's on each boundary are adjusted. These adjustments were made as follows:

$$\begin{aligned} C_j^{east} &= C_j + U, & C_j^{west} &= C_j - U, \\ C_j^{north} &= C_j + V, & C_j^{south} &= C_j - V. \end{aligned} \quad (\text{VII.21})$$

For this example, the adjusted  $C_j$ 's are:

$$\begin{aligned} C_j^{\text{east}} &= \{1.5, 1.5, 1.5, 1.5, 1.5\}, & C_j^{\text{north}} &= \{.75, .75, .75, .75, .75\}, \\ C_j^{\text{west}} &= \{.5, .5, .5, .5, .5\}, & C_j^{\text{south}} &= \{1.25, 1.25, 1.25, 1.25, 1.25\}. \end{aligned}$$

The results of both runs show a significant decrease in  $\|e(t)\|_\infty$  to about  $10^{-3}$  at  $t = 10$ . This error, however, can be reduced further.

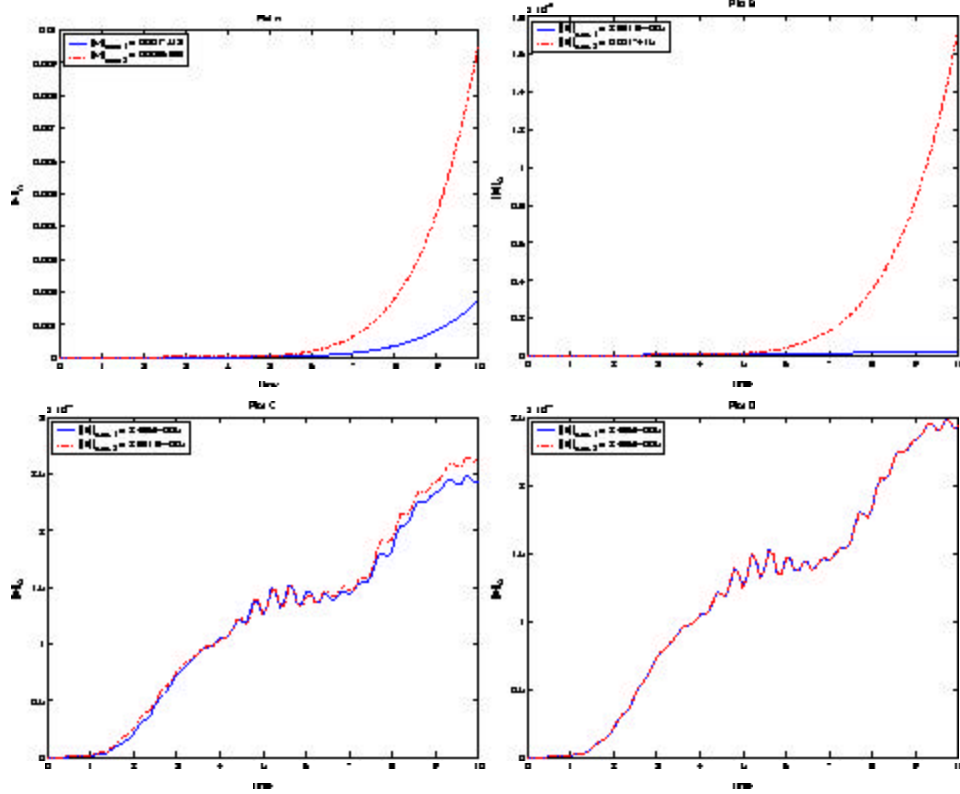


Figure 49. Plot A:  $J = 5$  with  $C_j = \{1, 1, 1, 1, 1\}$  adjusted for advection compared to  $J = 5$  with  $C_j = \{1, 1, 1, 1, 1\}$  unadjusted for advection. Plot B:  $J = 3$  with  $C_j = \{1, 1, 1\}$  compared to  $J = 5$  with  $C_j = \{1, 1, 1, 1, 1\}$ , both cases adjusted for advection. Plot C:  $J = 3$  with  $C_j = \{.8, .9, 1\}$  compared to  $J = 3$  with  $C_j = \{1, 1, 1\}$ , both cases adjusted for advection. Plot D: Corner check for  $J = 3$  with  $C_j = \{.8, .9, 1\}$  adjusted for advection

Recall from Section VI.C that a buffer of  $J$  zero-valued grid points was necessary to achieve stability for a  $J^{\text{th}}$ -order Higdon NRBC. When advection is incorporated into the problem, this buffer zone moves horizontally toward at least one of the

boundaries. Therefore the buffer is compressed with respect to the boundary toward which it is moving. In order to maintain stability we must either increase the size of the buffer zone, or reduce the order  $J$ . In plot B (top right) of Figure 49 a 5<sup>th</sup>-order Higdon NRBC is compared to a 3<sup>rd</sup>-order Higdon NRBC. In both cases the  $C_j$ 's are adjusted for advection. In this example,  $\|e(t)\|_\Omega$  is reduced by an order of magnitude to about  $10^{-4}$ .

One further adjustment is possible to reduce  $\|e(t)\|_\Omega$ . Geometric dispersion is another factor in the boundaries response to an impinging wave. A wave striking normal to the boundary will generally have a wave speed that is approximately  $C_0$ . In all other cases, the wave speed is less than  $C_0$ . An example was set up for  $J = 3$  in which  $C_j = \{.8, .9, 1\}$  with the reduced values taking into account the geometric dispersion. Adjusted for advection, the  $C_j$ 's used for the problem are:

$$\begin{aligned} C_j^{east} &= \{1.3, 1.4, 1.5\}, & C_j^{north} &= \{.55, .65, .75\}, \\ C_j^{west} &= \{.3, .4, .5\}, & C_j^{south} &= \{1.05, 1.15, 1.25\}. \end{aligned} \tag{VII.22}$$

In Plot C (bottom left) of Figure 49 an additional reduction in  $\|e(t)\|_\Omega$  is evident. Further analysis is necessary to determine how to best adjust  $C_j$  values for geometric dispersion.

The question of the corner points of  $\Omega$  is again salient in the advection case, because the values for  $C_j$  on each boundary are now different. Recall that there are two ways to approximate the boundary values when numerically solving the problem. Both approaches are tested here. In the first run the  $x$ -boundaries were computed first (including the corner points) and the  $y$ -boundaries computed next (excluding the corner points). In a second experiment the procedure was reversed and corner points were included in the  $y$ -boundaries. Plot D (bottom right) of Figure 49 reveals that the solutions are identical. Hence, as concluded earlier, no special handling at the corner points is necessary.

With these results in mind, Higdon NRBC's of order  $J = 3$  with  $C_j = \{.8, .9, 1\}$  are used. With  $U = .5$  and  $V = -.25$ , the adjusted  $C_j$ 's are those listed in (VII.22).

A trial is run for 10 time units. At  $t = 1$  (Figure 50), event 1 has been propagating outward in  $\Omega$  for approximately 1 time unit. The effect of advection is apparent as the propagation of the gravity wave is tending toward the southeast (i.e. in the  $\langle .5, -.25 \rangle$  direction). The leading edge of the wave has passed through the  $\Gamma_E$ , but the error measurement is still very small. At  $t = 2$  (Figure 51), event 1 has crossed  $\Gamma_S$  and  $\Gamma_E$ . Later, at  $t = 3$  (Figure 52), event 1 has crossed  $\Gamma_N$  and  $\Gamma_W$ . At  $t = 5$  (Figure 53), most of event 1 has left  $\Omega$ . We note some spurious activity on the western boundary.

At  $t = 6$  (Figure 54), the waves generated by event 2 are approaching  $\Gamma_E$  and  $\Gamma_W$ . Event 1 has passed through all four boundaries relatively unperturbed. The plot of  $\mathcal{D}$  reveals that the wave front continues to tend toward the southern and eastern portion of the extended domain.

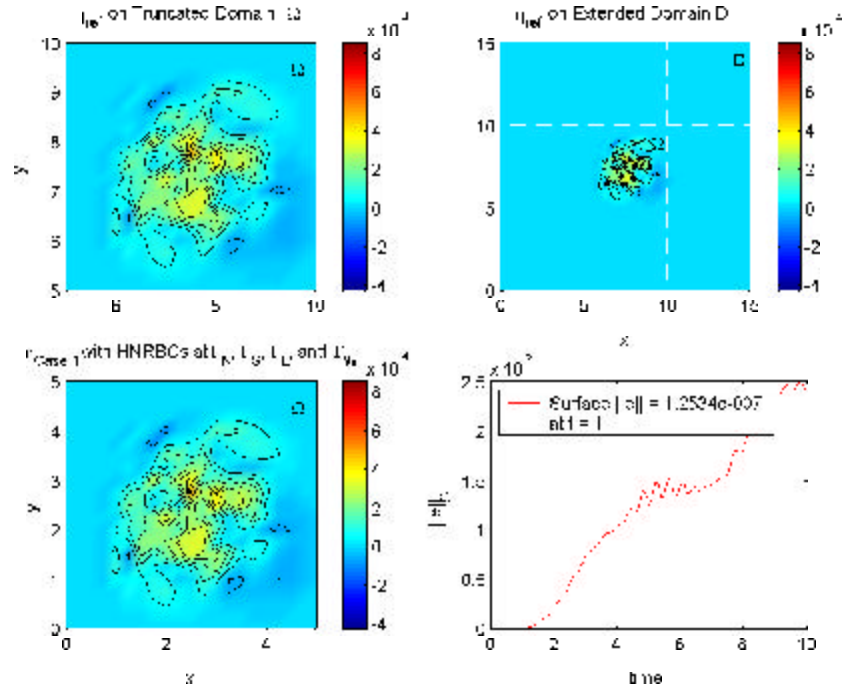


Figure 50. HNRBC-2DR-4S-1L-U.5-Vm.25-T01: Event 1 Initiated.

At  $t = 10$  (Figure 55), the second event has passed through the boundary. The wave propagation pattern continues to “drift” in the direction of advection as revealed

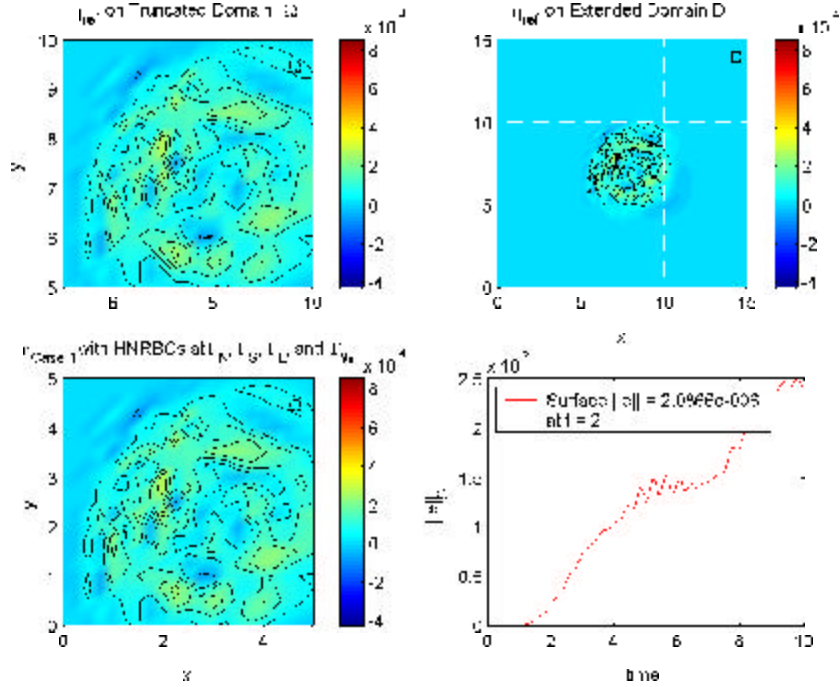


Figure 51. HNRBC-2DR-4S-1L-U.5-Vm.25-T02: Event 1 Crosses  $\Gamma_S$  and  $\Gamma_E$ .

by the upper-right plot of  $\mathcal{D}$ . Close inspection of the contours reveal spreading where the gravity wave is traveling in the direction of advection and compression where the gravity wave is traveling against the direction of advection. In the latter case, this indicates a steeper wave front. Since the gravity wave is omni-directional, this effect varies throughout the plot. In  $\Omega$  the noise of spurious reflection is now visible.

This experiment was repeated for two other sets of values for  $U$  and  $V$ . In the first variation (Figure 56) the magnitude of the advection constants were lowered to  $U = .4$  and  $V = -.15$ . As expected, there is a decreased tendency toward the southeast. Also notable is a reduction in the error measurement. In the second variation (Figure 57), the magnitude of the advection constants was increased to  $U = .6$  and  $V = -.35$ . The tendency to the southeast, as well as the error measurement, has increased. These results indicate that the model is behaving as expected with regards to the rate and direction of advection. However, as the magnitude of the advection constants is increased, the measured error will also increase. In the current



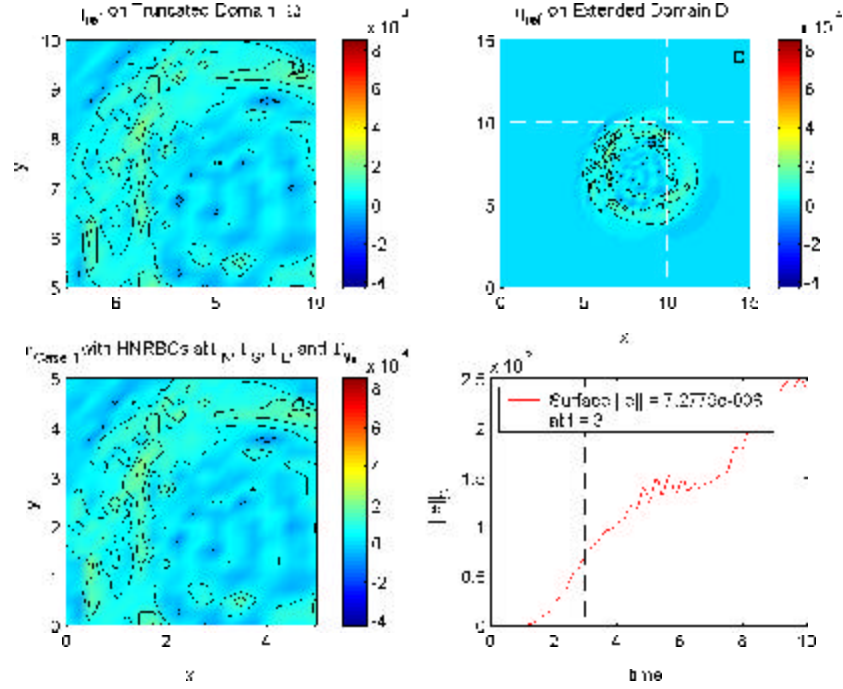


Figure 52. HNRBC-2DR-4S-1L-U.5-Vm.25-T03: Event 1 Crosses  $\Gamma_N$  and  $\Gamma_W$ .

example, the magnitude of the advection is 4 to 7 times greater than the magnitude of the depth. In a real world problem, where the open ocean is the medium of propagation, advection constants are expected to be significantly smaller.

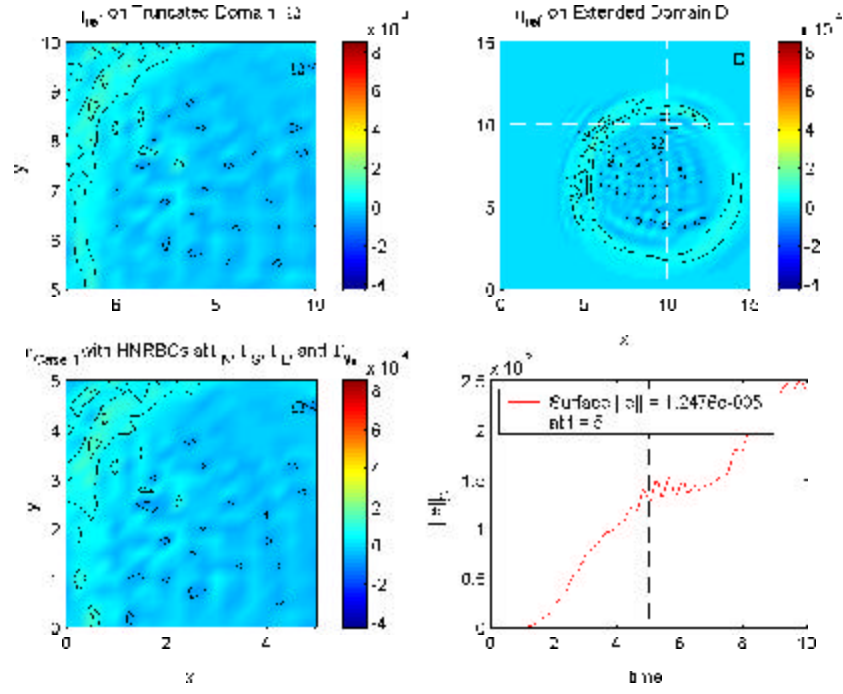


Figure 53. HNRBC-2DR-4S-1L-U.5-Vm.25-T05: Event 1 Leaves  $\Omega$  with Visible Spurious Reflection at  $\Gamma_W$ .

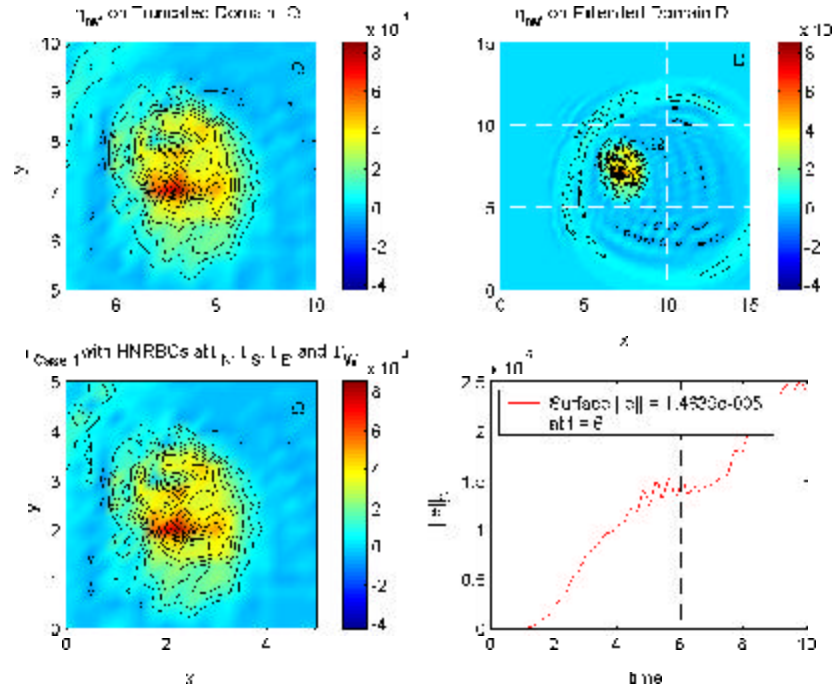


Figure 54. HNRBC-2DR-4S-1L-U.5-Vm.25-T06: Event 2 Initiated.

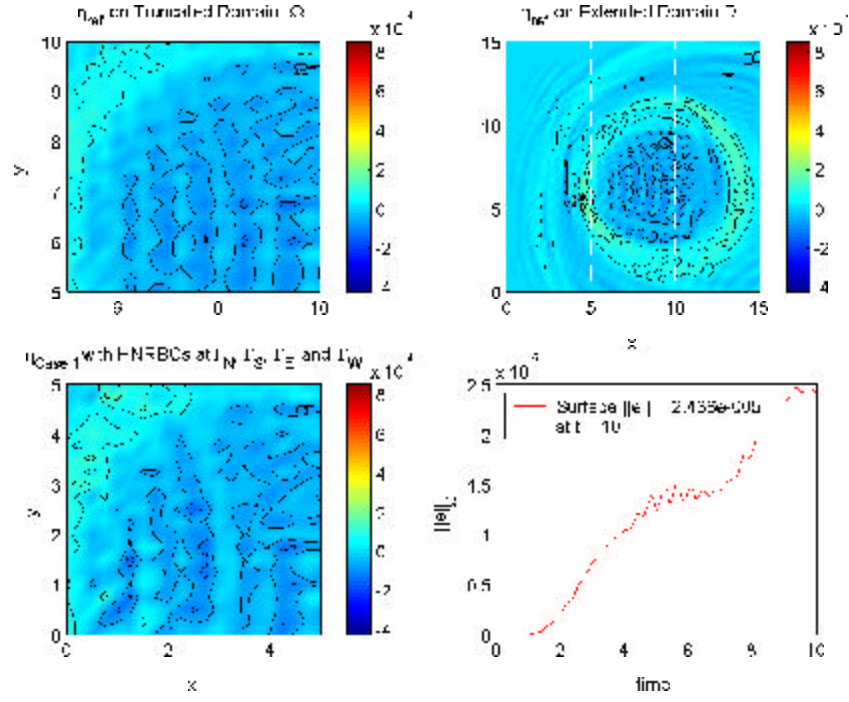


Figure 55. HNRBC-2DR-4S-1L-U.5-Vm.25-T10: The Noise of Spurious Reflection Evident at the Bottom Left Plot.

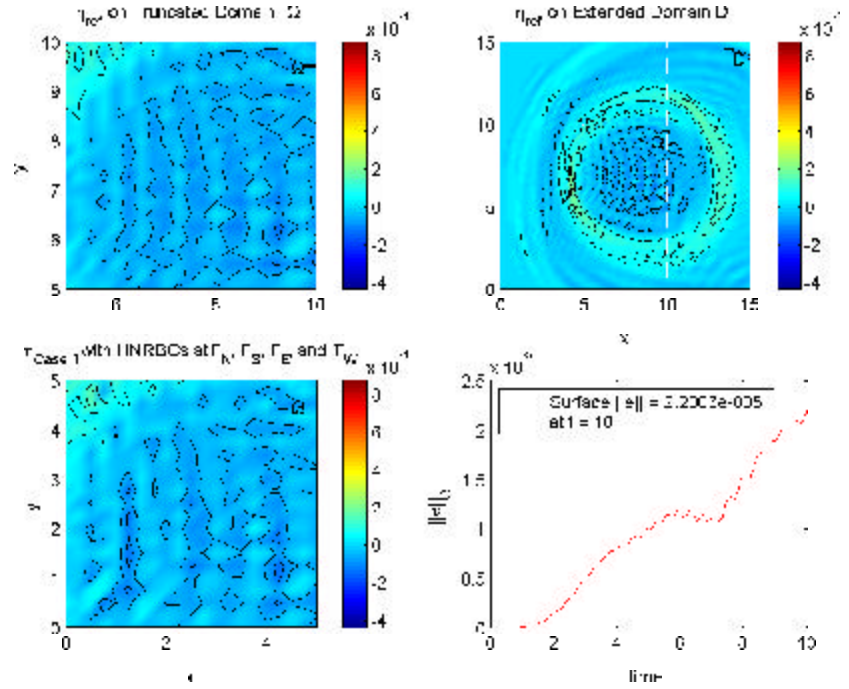


Figure 56. HNRBC-2DR-4S-1L-U.4-Vm.15-T10: End of Run

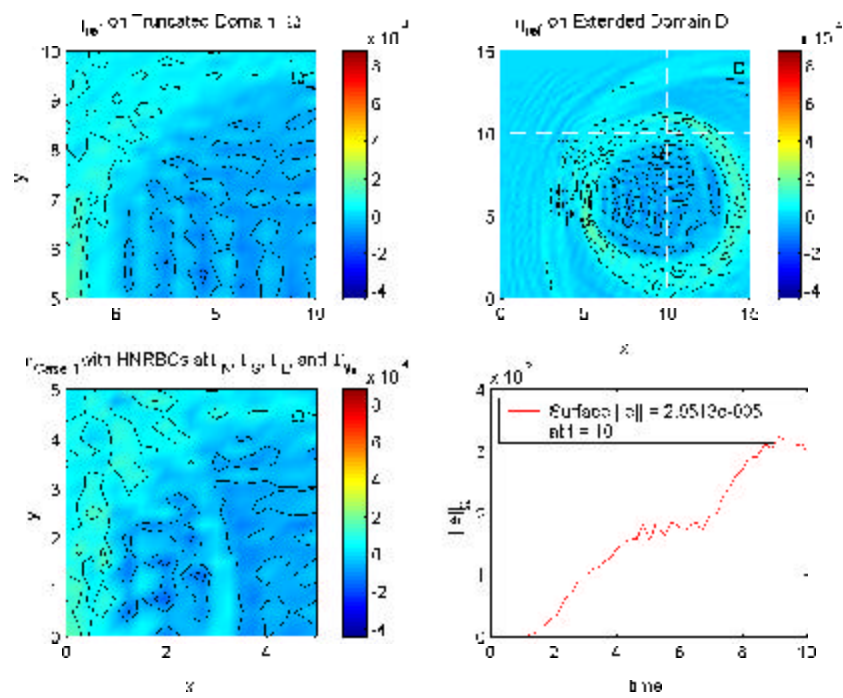


Figure 57. HNRBC-2D-4S-1L-U.6-Vm.35-T10: End of Run

### C. LINEARIZED SWE WITH CONSTANT NON-ZERO ADVECTION TERMS EXTENDED TO THE $N$ -LAYER MODEL

Recall the linearized form of the shallow water equation with non-zero advection terms for a  $N$ -layer stratified model (V.10):

$$\frac{\partial u_i^*}{\partial t} + U_i \frac{\partial u_i^*}{\partial x} + V_i \frac{\partial u_i^*}{\partial y} - f(V_i + v_i^*) = -g \left( \sum_{j=1}^{i-1} \frac{\rho_j}{\rho_i} \frac{\partial \eta_j}{\partial x} + \sum_{j=i}^N \frac{\partial \eta_j}{\partial x} \right),$$

$$\frac{\partial v_i^*}{\partial t} + U_i \frac{\partial v_i^*}{\partial x} + V_i \frac{\partial v_i^*}{\partial y} + f(U_i + u_i^*) = -g \left( \sum_{j=1}^{i-1} \frac{\rho_j}{\rho_i} \frac{\partial \eta_j}{\partial y} + \sum_{j=i}^N \frac{\partial \eta_j}{\partial y} \right),$$

$$\frac{\partial \eta_i}{\partial t} + U_i \frac{\partial \eta_i}{\partial x} + V_i \frac{\partial \eta_i}{\partial y} + \Theta_i \left( \frac{\partial u_i^*}{\partial x} + \frac{\partial v_i^*}{\partial y} \right) = 0,$$

where  $U_i$  and  $V_i$  are the  $x$ - and  $y$ -components of advection in the  $i^{\text{th}}$ -layer. The same techniques as those described in Section II.B.3 are used to generate a single equation for  $\eta_i$ , the perturbation of the  $i^{\text{th}}$ -layer. As an intermediate step a result that is analogous to (V.19) and (VII.6) is generated:

$$\left[ \frac{D^2}{Dt^2} \right]_i (\eta_i) - g \Theta_i \nabla^2 \left( \sum_{j=1}^{i-1} \frac{\rho_j}{\rho_i} \eta_j + \sum_{j=i}^N \eta_j \right) + f^2 \eta_i = S_i(x, y, t), \quad (\text{VII.23})$$

where  $S_i(x, y, t)$  is the source function for the  $i^{\text{th}}$ -layer of an  $N$ -layer model. The operator  $\left[ \frac{D}{Dt} \right]_i$  is defined as:

$$\frac{\partial}{\partial t} + U_i \frac{\partial}{\partial x} + V_i \frac{\partial}{\partial y}. \quad (\text{VII.24})$$

$S_i(x, y, t)$  must satisfy:

$$\left[ \frac{D}{Dt} \right]_i (S_i(x, y, t)) = \frac{\partial S_i}{\partial t} + U_i \frac{\partial S_i}{\partial x} + V_i \frac{\partial S_i}{\partial y} = 0. \quad (\text{VII.25})$$

Considering the homogeneous form for (VII.23) and expanding yields:

$$\begin{aligned}
& \frac{\partial^2 \eta_i}{\partial t^2} + U_i^2 \frac{\partial^2 \eta_i}{\partial x^2} - C_{0i}^2 \frac{\partial^2}{\partial x^2} \left( \sum_{j=1}^{i-1} \frac{\rho_j}{\rho_i} \eta_j + \sum_{j=i}^N \eta_j \right) \\
& + V_i^2 \frac{\partial^2 \eta_i}{\partial y^2} - C_{0i}^2 \frac{\partial^2}{\partial y^2} \left( \sum_{j=1}^{i-1} \frac{\rho_j}{\rho_i} \eta_j + \sum_{j=i}^N \eta_j \right) \\
& + 2U_i \frac{\partial^2 \eta_i}{\partial x \partial t} + 2V_i \frac{\partial^2 \eta_i}{\partial y \partial t} + 2U_i V_i \frac{\partial^2 \eta_i}{\partial x \partial y} + f^2 \eta_i = 0.
\end{aligned} \tag{VII.26}$$

This is the linearized shallow water equation for an  $N$ -layer model with non-zero advection terms.

## D. DISCRETIZING THE LINEARIZED SWE $N$ -LAYER STRATIFIED MODEL WITH CONSTANT NON-ZERO ADVECTION TERMS

As before, using the central-difference approximations in (VII.11) to discretize (VII.26) yields:

$$\begin{aligned}
& \frac{1}{\Delta t^2}(\eta_{i,pq}^{n+1} - 2\eta_{i,pq}^n + \eta_{i,pq}^{n-1}) + f^2\eta_{i,pq}^n \\
& + \frac{U_i^2}{\Delta x^2}(\eta_{i,p+1,q}^n - 2\eta_{i,pq}^n + \eta_{i,p-1,q}^n) + \frac{V_i^2}{\Delta y^2}(\eta_{i,p,q+1}^n - 2\eta_{i,pq}^n + \eta_{i,p,q-1}^n) \\
& + \frac{U_i}{2\Delta x\Delta t}(\eta_{i,p+1,q}^{n+1} - \eta_{i,p+1,q}^{n-1} - \eta_{i,p-1,q}^{n+1} + \eta_{i,p-1,q}^{n-1}) \\
& + \frac{V_i}{2\Delta y\Delta t}(\eta_{i,p,q+1}^{n+1} - \eta_{i,p,q+1}^{n-1} - \eta_{i,p,q-1}^{n+1} + \eta_{i,p,q-1}^{n-1}) \\
& + \frac{U_i V_i}{2\Delta x\Delta y}(\eta_{i,p+1,q+1}^n - \eta_{i,p+1,q-1}^n - \eta_{i,p-1,q+1}^n + \eta_{i,p-1,q-1}^n) \\
& - \left(\frac{C_{0i}}{\Delta x}\right)^2 \left[ \sum_{j=1}^{i-1} \frac{\rho_j}{\rho_i} (\eta_{j,p+1,q}^n - 2\eta_{j,pq}^n + \eta_{j,p-1,q}^n) \right] \\
& - \left(\frac{C_{0i}}{\Delta x}\right)^2 \left[ \sum_{j=i}^N (\eta_{j,p+1,q}^n - 2\eta_{j,pq}^n + \eta_{j,p-1,q}^n) \right] \\
& - \left(\frac{C_{0i}}{\Delta y}\right)^2 \left[ \sum_{j=1}^{i-1} \frac{\rho_j}{\rho_i} (\eta_{j,p,q+1}^n - 2\eta_{j,pq}^n + \eta_{j,p,q-1}^n) \right] \\
& - \left(\frac{C_{0i}}{\Delta y}\right)^2 \left[ \sum_{j=i}^N (\eta_{j,p,q+1}^n - 2\eta_{j,pq}^n + \eta_{j,p,q-1}^n) \right] = 0.
\end{aligned} \tag{VII.27}$$

This is the discretized form of the  $N$ -layer linearized shallow water equation with constant, non-zero advection for the  $i^{\text{th}}$ -layer. All terms that contain the  $n+1$  superscript are unknown values of  $\eta_i$  which must be solved. Making the following

substitutions:

$$A = \frac{1}{\Delta t^2}, \quad B_i = \left( \frac{U_i}{\Delta x} \right)^2, \quad C_i = \left( \frac{V_i}{\Delta y} \right)^2, \quad D_i = \frac{U_i}{2\Delta x \Delta t},$$
(VII.28)

$$E_i = \frac{V_i}{2\Delta y \Delta t}, \quad F_i = \frac{U_i V_i}{2\Delta x \Delta y}, \quad G_i = \left( \frac{C_{0i}}{\Delta x} \right)^2, \quad H_i = \left( \frac{C_{0i}}{\Delta y} \right)^2,$$

moving known terms to the right side of (VII.27), and shifting the time index yields:

$$\begin{aligned} & A\eta_{i,pq}^n + D_i\eta_{i,p+1,q}^n - D_i\eta_{i,p-1,q}^n + E_i\eta_{i,p,q+1}^n - E_i\eta_{i,p,q-1}^n = \\ & (2A + 2B_i + 2C_i - f^2)\eta_{i,pq}^{n-1} - A\eta_{i,pq}^{n-2} \\ & - B_i \left( \eta_{i,p+1,q}^{n-1} + \eta_{i,p-1,q}^{n-1} \right) - C_i \left( \eta_{i,p,q+1}^{n-1} + \eta_{i,p,q-1}^{n-1} \right) \\ & + D_i \left( \eta_{i,p+1,q}^{n-2} - \eta_{i,p-1,q}^{n-2} \right) + E_i \left( \eta_{i,p,q+1}^{n-2} - \eta_{i,p,q-1}^{n-2} \right) \\ & - F_i \left( \eta_{i,p+1,q+1}^{n-1} - \eta_{i,p+1,q-1}^{n-1} - \eta_{i,p-1,q+1}^{n-1} + \eta_{i,p-1,q-1}^{n-1} \right) \\ & + G_i \left[ \sum_{j=1}^{i-1} \frac{\rho_j}{\rho_i} \left( \eta_{j,p+1,q}^{n-1} - 2\eta_{j,pq}^{n-1} + \eta_{j,p-1,q}^{n-1} \right) \right] \\ & + G_i \left[ \sum_{j=i}^N \left( \eta_{j,p+1,q}^{n-1} - 2\eta_{j,pq}^{n-1} + \eta_{j,p-1,q}^{n-1} \right) \right] \\ & + H_i \left[ \sum_{j=1}^{i-1} \frac{\rho_j}{\rho_i} \left( \eta_{j,p,q+1}^{n-1} - 2\eta_{j,pq}^{n-1} + \eta_{j,p,q-1}^{n-1} \right) \right] \\ & + H_i \left[ \sum_{j=i}^N \left( \eta_{j,p,q+1}^{n-1} - 2\eta_{j,pq}^{n-1} + \eta_{j,p,q-1}^{n-1} \right) \right]. \end{aligned}$$
(VII.29)

As in the single-layer advection case, (VII.29) must be solved implicitly for each layer  $L_i$ . The system of equations is completed on the boundaries using the discretized



Higdon boundary equations as discussed in section VII.B.

## E. NUMERICAL EXAMPLE: A TWO-LAYER SCHEME INCORPORATING ADVECTION

In this example the domains  $\Omega$  and  $\mathcal{D}$  as described in Section VII.B with identical positioning of the Higdon NRBC's are utilized. The following problem parameters are used:

$$\begin{aligned}\Delta x = \Delta y &= .25, & \Delta t &= .1, \\ g &= 10, & f &= .5, \\ \Theta_i &= \{.03, .07\}, & \rho_i &= \{1, 1.05\}, \\ U_i &= \{.025, .025\}, & V_i &= \{-.025, -.025\}, \\ J &= 5, & C_j &= \{.6, .7, .8, .9, 1\}.\end{aligned}$$

Correcting the  $C_j$ 's for advection yields:

$$\begin{aligned}C_j^{east} &= \{.625, .725, .825, .925, 1.025\}, & C_j^{north} &= \{.575, .675, .775, .875, .975\}, \\ C_j^{west} &= \{.575, .675, .775, .875, .975\}, & C_j^{south} &= \{.625, .725, .825, .925, 1.025\}.\end{aligned}$$

A single physical disturbance is initiated in  $\Omega$  and is given by:

$$S_{L_1}^{t=.1} = \begin{cases} .000001 * rand(-.5, .5) & \text{if } 2 \leq x, y \leq 3, \\ 0 & \text{otherwise} \end{cases}, \quad (\text{VII.30})$$

where  $S_{L_1}^{t=.1}(x, y)$  represents a disturbance initiated in  $L_1$  at  $t = .1$  and  $rand(-.5, .5)$  is a random number on the interval  $[-.5, .5]$ . The example is run for five time steps.

At  $t = 1$  (Figure 58), the disturbance has been underway for approximately one second. Minimal spurious reflection occurs at the boundaries. In the lower-right plot two additional measurements are noted. The first, "Max Ref Surf" is  $|\eta|_{max}$  measured over the entire run. The next, "Max  $||e||$  Ratio" is given by:

$$\text{Max } ||e|| \text{ Ratio} = \frac{||e||_{max}}{|\eta|_{max}}. \quad (\text{VII.31})$$

Since both are maximums extracted from the data generated over the entire run, they will not change with time. Both are used in the next section to compare Higdon boundary effectiveness.

At  $t = 5$  (Figure 59), most of the wave action has left  $\Omega$ . The residual action in the truncated domains are, for the most part, similar. There is, however, some visible difference near the boundaries resultant from spurious reflection. The lower-right plot reports:

$$\text{Max } ||e||\text{Ratio} = 1.08\%.$$

That is to say, the maximum error norm  $||e||$  at  $t = 5$  was 1.08% of the  $|\eta|_{\max}$ . As we shall see in the next section, this is a favorable measurement for the Higdon NRBC.

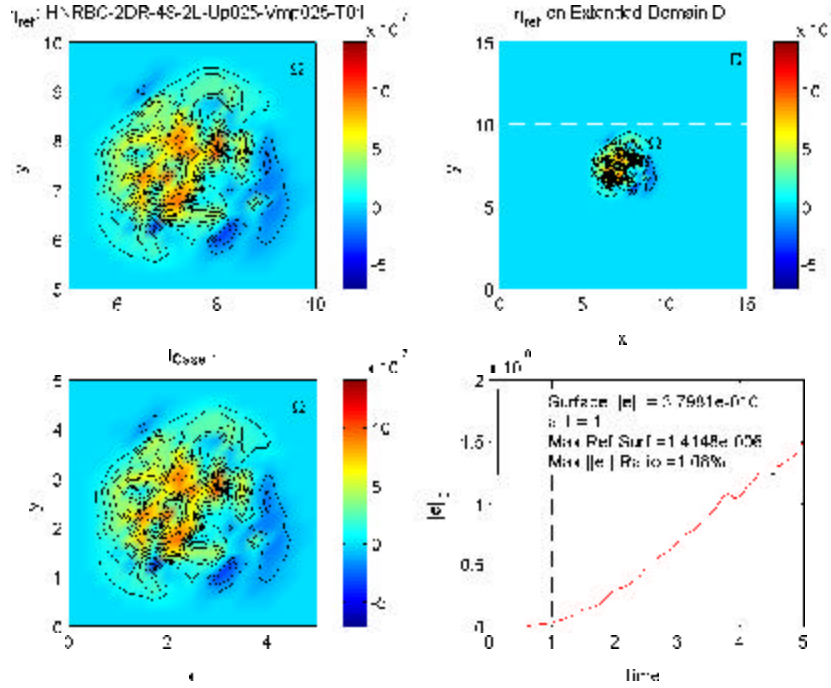


Figure 58. HNRBC-2DR-4S-2L-Up025-Vmp025-T01: Disturbance Initiated.

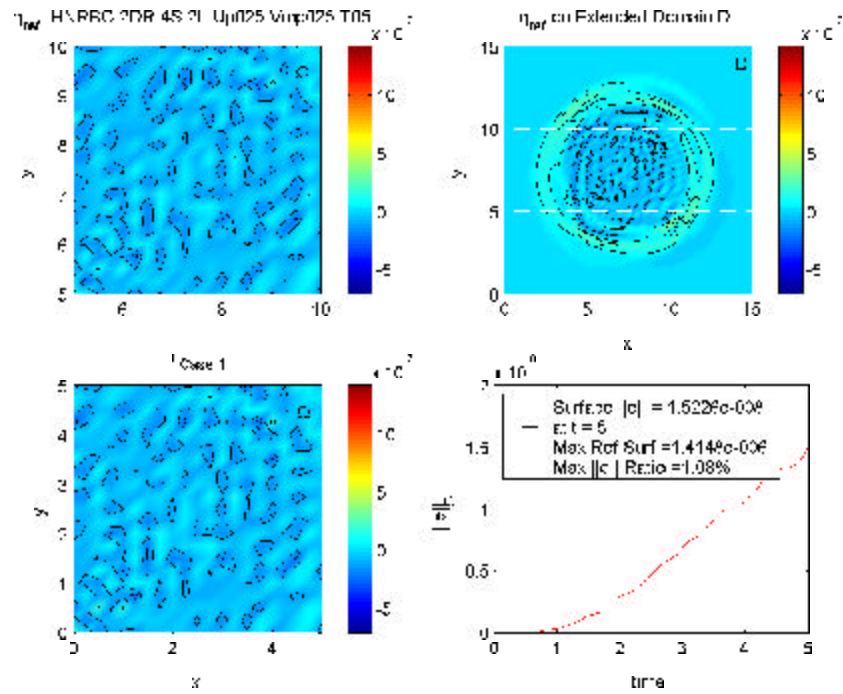


Figure 59. HNRBC-2DR-4S-2L-Up025-Vmp025-T05: End of Run, Some Noise at Boundaries of Bottom Left Plot.

## F. VARYING PARAMETERS FOR THE TWO-LAYER SCHEME WITH ADVECTION

Thus far in this dissertation, the truncated domain  $\Omega$  has been numerically compared to its infinite analog, the extended domain  $\mathcal{D}$ . Unfortunately, most of the computational assets are invested in generating a solution for this “pseudo-infinite” domain. In the four-sided Higdon NRBC’s, the extended domain  $\mathcal{D}$  contained nine times as many grid points as  $\Omega$ . Addition of advection considerations required employment of implicit methods. In these cases, computer storage became a key factor. For example,  $\mathcal{D}$  for a four-sided problem with  $\Delta x \Delta y = .25$  required a  $61^2 \times 61^2$  matrix to generate a solution whereas  $\Omega$  required a much smaller matrix of dimensions  $21^2 \times 21^2$ . Obviously sparse matrix procedures would alleviate this requirement, but the point illustrates that maintaining an extended domain becomes unwieldily if the domain of interest is enlarged or the grid is refined.

In the following subsections, parameters of a two-layer advection problem are varied and the resulting measurement of “Max  $\|e\|$  Ratio” (VII.31) is compared. From these comparisons, conclusions are listed that predict parameter limits that destabilize the Higdon NRBC. Knowledge of this behavior will allow us to drop extended domain comparisons and focus attention on the domain of interest.

In all trials, the domain  $\Omega$  is a  $5 \times 5$  square. The grid is varied as specified in each set of trials. The following event is used to initiate action in all trials:

$$S_{L_i}^{t=\Delta t} = \begin{cases} .000001 * rand(-.5, .5) & \text{if } 2 \leq x, y \leq 3, \\ 0 & \text{otherwise} \end{cases}, \quad (\text{VII.32})$$

where  $S_{L_i}^{t=\Delta t}$  is an event generated in the  $i^{\text{th}}$ -layer at  $t = \Delta t$  (i.e. the first time increment). Each trial is run for 5 time units and all  $C_j$ ’s are adjusted for advection.

## 1. Varying $C_j$ 's, $\Delta x$ , and $\Delta y$

In this set of trials the Higdon coefficients  $C_j$  were varied. The following parameters were fixed:

$$\begin{aligned} H_i &= \{.03, .07\}, & \rho_i &= \{1., 1.05\}, \\ U_i &= \{.025, .025\}, & V_i &= \{-.025, -.025\}, \\ \Delta t &= .1 & \Delta x = \Delta y &= .5 \end{aligned} \tag{VII.33}$$

The value for  $|\eta|_{max}$  was determined to be  $1.92 \times 10^{-6}$  and was unaffected by the choice of  $C_j$ 's. Results for  $\Delta x = \Delta y = .5$  are posted in Table IV and were compared using  $\frac{\|e\|_{max}}{|\eta|_{max}}$ , a measure described in Section VII.E. This set of numerical trials was

Table IV. Varying  $C_j$ -s with  $\Delta x = \Delta y = .5$

$C_j$	$\frac{\ e\ _{max}}{ \eta _{max}}$	$C_j$	$\frac{\ e\ _{max}}{ \eta _{max}}$
$\{.1, .6, 1\}$	3.47%	$\{0, .5, 1\}$	3.83%
$\{.1, .5, 1\}$	3.53%	$\{.7, .8, .9\}$	3.97%
$\{.6, .8, 1\}$	3.57%	$\{.8, .9, 1\}$	4.13%
$\{.1, .75, 1\}$	3.58%	$\{1 \ 1 \ 1\}$	4.21%
$\{.025, .6, .975\}$	3.58%	$\{1, 1\}$	4.23%
$\{.4, .7, 1\}$	3.61%	$\{.1, .1, 1\}$	5.99%
$\{.1, .5, .9\}$	3.63%	$\{1, 1, 1, 1\}$	92.2%
$\{.5, .5, .5\}$	3.76%		

repeated for  $\Delta x = \Delta y = .25$ . In this case  $|\eta|_{max}$  was determined to be  $1.41 \times 10^{-6}$ , a change that reflects the nature of the random event (VII.32) that was used to generate the disturbance. The results of these trials are reported in Table V. Several conclusions are drawn from these:

- Refining the grid results in a more efficient boundary conditions (e.g. less spurious reflections).
- Higher order Higdon NRBC's tended to generate more effective boundary conditions.
- A buffer zone as discussed in Section VI.B and VII.B must be considered. This limits the Higdon order  $J$  that can be used. For  $\Delta x = \Delta y = .5$ , the trial

Table V. Varying  $C_j$ -s with  $\Delta x = \Delta y = .25$

$C_j$	$\frac{\ e\ _{max}}{\eta _{max}}$	$C_j$	$\frac{\ e\ _{max}}{\eta _{max}}$
$\{.6,.7,.8,.9,1\}$	1.08%	$\{.1,.75,1\}$	2.14%
$\{.9,.925,.95,.975,1\}$	1.13%	$\{.5,.5,.5\}$	2.15%
$\{1,1,1,1,1\}$	1.16%	$\{.1,.6,1\}$	2.24%
$\{.1,.5,.6,.7,1\}$	1.19%	$\{.1,.5,1\}$	2.37%
$\{.7,.8,.9,1\}$	1.21%	$\{.1,.5,.9\}$	2.37%
$\{1,1,1,1\}$	1.24%	$\{1,1\}$	2.37%
$\{.8,.9,1\}$	1.57%	$\{.025,.6,.975\}$	2.43%
$\{1,1,1\}$	1.58%	$\{0,.5,1\}$	2.64%
$\{.7,.8,.9\}$	1.60%	$\{.1,.1,1\}$	3.71%
$\{.6,.8,1\}$	1.63%	$\{1,1,1,1,1,1\}$	393%
$\{.4,.7,1\}$	1.77%		

became unstable for  $J = 4$ . For  $\Delta x = \Delta y = .25$ , instability occurred at  $J = 6$ . In the latter case, higher order Higdon NRBC's could be used increasing the effectiveness of the boundary condition. Auxiliary variables (see [Ref. 26]) will alleviate this problem.

- Distributing the  $C_j$ 's on the interval  $[.5, 1]$  seemed to reduce spurious reflection, but how to distribute these values best could not be determined. In any event, it appeared that at least one of the values should be equal to the gravity wave speed  $C_0$ , which in this case was 1.
- As  $\frac{\|e\|_{max}}{\eta|_{max}}$  approached 5%, spurious reflections became visible. Values of 3% produced acceptable results. Obviously, less is better.

## 2. Varying $U$ and $V$

In this set of trials  $U$  and  $V$  are varied, however, their respective values are kept the same in each layer. The following parameters are fixed:

$$\begin{aligned}
 H_i &= \{.03, .07\}, \quad \rho_i = \{1., 1.05\}, \\
 \Delta t &= .1, \quad \Delta x = \Delta y = .5, \\
 J &= 3, \quad C_j = \{.8, .9, 1\}.
 \end{aligned} \tag{VII.34}$$

Results are posted in Table VI. These trials were repeated for  $\Delta x = \Delta y = .25$  with results reported in Table VII. Another set of trials were conducted for  $C_j = \{.1, .6, 1\}$

Table VI. Varying  $U$  and  $V$  with  $\Delta x = \Delta y = .5$  ( $U, V$  Equal in each Layer)

$U$	$V$	$ \eta _{max}$	$\frac{\ e\ _{max}}{ \eta _{max}}$
$\{.0001,.0001\}$	$\{-.0001,-.0001\}$	$1.92 \times 10^{-6}$	4.13%
$\{.01,.01\}$	$\{-.01,-.01\}$	$1.92 \times 10^{-6}$	4.13%
$\{.025,.025\}$	$\{-.025,-.025\}$	$1.92 \times 10^{-6}$	4.13%
$\{.03,.03\}$	$\{-.03,-.03\}$	$1.92 \times 10^{-6}$	4.14%
$\{.035,.035\}$	$\{-.035,-.035\}$	$1.92 \times 10^{-6}$	4.17%
$\{.04,.04\}$	$\{-.04,-.04\}$	$1.92 \times 10^{-6}$	4.20%
$\{.05,.05\}$	$\{-.05,-.05\}$	$1.92 \times 10^{-6}$	4.31%
$\{.1,.1\}$	$\{-.1,-.1\}$	$1.93 \times 10^{-6}$	7.01%
$\{.25,.25\}$	$\{-.25,-.25\}$	$2.32 \times 10^{-3}$	95.5%

Table VII. Varying  $U$  and  $V$  with  $\Delta x = \Delta y = .25$  ( $U, V$  Equal in each Layer)

$U$	$V$	$ \eta _{max}$	$\frac{\ e\ _{max}}{ \eta _{max}}$
$\{.0001,.0001\}$	$\{-.0001,-.0001\}$	$1.42 \times 10^{-6}$	2.28%
$\{.01,.01\}$	$\{-.01,-.01\}$	$1.42 \times 10^{-6}$	2.24%
$\{.1,.1\}$	$\{-.1,-.1\}$	$1.40 \times 10^{-6}$	3.98%
$\{.25,.25\}$	$\{-.25,-.25\}$	$1.07 \times 10^{-3}$	58.5%

with  $\Delta x = \Delta y = .25$ . All other parameters were unchanged. Again  $U$  and  $V$  was varied, but this time the advection coefficients were allowed to differ between the layers. Table VIII reports the results when the disturbance is initiated in  $L_1$ , while Table IX reports results when the disturbance is initiated in  $L_2$ . From these results, it can be concluded:

- The problem became unstable when  $U, V$  became large. A good rule of thumb is to keep  $U, V \ll d$ , the total depth of the medium. This is a physical constraint in an ocean environment that assumes that the magnitude of advection will be much less than the magnitude of depth.
- Refining the grid improved performance.
- The instability of the problem intensifies when  $U, V$  differs between layers. Such problems should be avoided, when advective differences between layers are small.

Table VIII. Varying  $U$  and  $V$  with  $\Delta x = \Delta y = .25$  for Event Initiated in  $L_1$  ( $U, V$  not Necessarily Equal in each Layer)

$U$	$V$	$ \eta _{max}$	$\frac{\ e\ _{max}}{ \eta _{max}}$
$\{.02, .02\}$	$\{-.02, -.02\}$	$1.92 \times 10^{-6}$	3.50%
$\{0, 0\}$	$\{-.02, -.02\}$	$1.92 \times 10^{-6}$	3.51%
$\{.02, .02\}$	$\{0, 0\}$	$1.92 \times 10^{-6}$	3.60%
$\{0, 0\}$	$\{0, 0\}$	$1.92 \times 10^{-6}$	3.92%
$\{.01, 0\}$	$\{-.01, 0\}$	$1.92 \times 10^{-6}$	7.26%
$\{0, .02\}$	$\{0, -.02\}$	$1.92 \times 10^{-6}$	12.6%
$\{.01, -.01\}$	$\{-.01, .01\}$	$1.94 \times 10^{-6}$	12.8%
$\{.02, 0\}$	$\{-.02, 0\}$	$1.92 \times 10^{-6}$	13.1%
$\{.02, -.02\}$	$\{-.02, .02\}$	$1.99 \times 10^{-6}$	25.5%

### 3. Varying Layer Thicknesses in a 2-Layer Problem

In this set of trials, the layer thicknesses are varied. The following parameters were fixed:

$$\begin{aligned}
 \rho_i &= \{1., 1.05\}, \\
 \Delta t &= .1 & \Delta x = \Delta y &= .5 \\
 J &= 3 & C_j &= \{.8, .9, 1\} \\
 U &= \{.025, .025\}, & V &= \{-.025, -.025\}.
 \end{aligned} \tag{VII.35}$$

Table IX. Varying  $U$  and  $V$  with  $\Delta x = \Delta y = .25$  for Event Initiated in  $L_2$  ( $U, V$  not Necessarily Equal in each Layer)

$U$	$V$	$ \eta _{max}$	$\frac{\ e\ _{max}}{ \eta _{max}}$
$\{0, 0\}$	$\{-.02, -.02\}$	$1.92 \times 10^{-6}$	3.61%
$\{.01, -.01\}$	$\{-.01, .01\}$	$1.94 \times 10^{-6}$	3.63%
$\{0, .02\}$	$\{0, -.02\}$	$1.92 \times 10^{-6}$	3.71%
$\{.02, .02\}$	$\{-.02, -.02\}$	$1.92 \times 10^{-6}$	3.74%
$\{0, 0\}$	$\{0, 0\}$	$1.92 \times 10^{-6}$	4.38%
$\{.02, -.02\}$	$\{-.02, .02\}$	$1.99 \times 10^{-6}$	6.31%
$\{.02, .02\}$	$\{0, 0\}$	$1.92 \times 10^{-6}$	6.32%
$\{.01, 0\}$	$\{-.01, 0\}$	$1.92 \times 10^{-6}$	6.85%
$\{.02, 0\}$	$\{-.02, 0\}$	$1.92 \times 10^{-6}$	11.3%



Results for a disturbance initiated in  $L_1$  and  $L_2$  are posted in Table X. It is readily

Table X. Varying Layer Thickness in a 2-Layer Problem with an  $L_1$  Initiated Event (left) and  $L_2$  Initiated Event (right)

$\Omega_i$	$ \eta _{max}$	$\frac{\ e\ _{max}}{ \eta _{max}}$	$ \eta _{max}$	$\frac{\ e\ _{max}}{ \eta _{max}}$
$\{.1, 0\}$	$1.89 \times 10^{-6}$	3.57%	$1.89 \times 10^{-6}$	3.57%
$\{.1, 9\}$	$1.99 \times 10^{-6}$	3.67%	$1.89 \times 10^{-6}$	3.57%
$\{.2, 8\}$	$1.99 \times 10^{-6}$	3.51%	$1.89 \times 10^{-6}$	3.58%
$\{.3, 7\}$	$1.92 \times 10^{-6}$	3.47%	$1.89 \times 10^{-6}$	3.58%
$\{.4, 6\}$	$1.92 \times 10^{-6}$	3.45%	$1.89 \times 10^{-6}$	3.58%
$\{.5, 5\}$	$1.91 \times 10^{-6}$	3.46%	$1.89 \times 10^{-6}$	3.58%
$\{.6, 4\}$	$1.91 \times 10^{-6}$	3.48%	$1.89 \times 10^{-6}$	3.58%
$\{.7, 3\}$	$1.90 \times 10^{-6}$	3.51%	$1.89 \times 10^{-6}$	3.58%
$\{.8, 2\}$	$1.90 \times 10^{-6}$	3.53%	$1.89 \times 10^{-6}$	3.57%
$\{.9, 1\}$	$1.89 \times 10^{-6}$	3.56%	$1.89 \times 10^{-6}$	3.57%

concluded that:

- Varying layer thicknesses does not alter the effectiveness of the Higdon NRBC. This conclusion is independent of the layer in which the disturbance was initiated.

#### 4. Varying Density Distribution in a 2-Layer Problem

In this set of trials, the density distributions are varied. The following parameters were fixed:

$$\begin{aligned}
 \Omega_i &= \{.03, .07\}, \\
 \Delta t &= .1 & \Delta x = \Delta y &= .5 \\
 J &= 3 & C_j &= \{.8, .9, 1\} \\
 U &= \{.025, .025\}, & V &= \{-.025, -.025\}.
 \end{aligned} \tag{VII.36}$$

Results for a disturbance initiated in  $L_1$  and  $L_2$  are posted in Table XI. From these trials it is concluded that:

- Density changes do, to some extent alter the behavior of the Higdon HNRBC, but in general, they remain effective as long as the density increases monotonically with each increasing layer.

Table XI. Varying Layer Thickness in a 2-Layer Problem with a  $L_1$  Initiated Event (left) and  $L_2$  Initiated Event (right)

$\rho_i$	$ \eta _{max}$	$\frac{\ e\ _{max}}{ \eta _{max}}$	$ \eta _{max}$	$\frac{\ e\ _{max}}{ \eta _{max}}$
$\{1,1\}$	$1.89 \times 10^{-6}$	3.58%	$1.89 \times 10^{-6}$	3.58%
$\{1,1.05\}$	$1.92 \times 10^{-6}$	3.47%	$1.89 \times 10^{-6}$	3.58%
$\{1,1.10\}$	$1.99 \times 10^{-6}$	3.20%	$1.88 \times 10^{-6}$	3.60%
$\{1,1.15\}$	$2.03 \times 10^{-6}$	2.02%	$1.88 \times 10^{-6}$	3.60%
$\{1,1.20\}$	$2.05 \times 10^{-6}$	2.98%	$1.88 \times 10^{-6}$	3.57%
$\{1,1.25\}$	$2.05 \times 10^{-6}$	3.02%	$1.91 \times 10^{-6}$	3.47%
$\{1,1.50\}$	$2.18 \times 10^{-6}$	3.11%	$2.10 \times 10^{-6}$	3.20%
$\{1.05,1\}$	$1.85 \times 10^{-6}$	4.35%	$1.89 \times 10^{-6}$	3.92%
$\{1.10,1\}$	$1.92 \times 10^{-6}$	8.84%	$1.93 \times 10^{-6}$	3.92%
$\{1.25,1\}$	$2.10 \times 10^{-5}$	8.69%	$1.09 \times 10^{-5}$	6.94%

## 5. Varying $\Delta t$ in a 2-Layer Problem

In this set of trials  $\Delta t$  is varied. The following parameters were fixed:

$$\begin{aligned}
 \Omega_i &= \{.03, .07\}, \quad \rho_i = \{1, 1.05\} \\
 \Delta x &= \Delta y = .5, \\
 J &= 3, \quad C_j = \{.8, .9, 1\}, \\
 U &= \{0, 0\}, \quad V = \{0, 0\}.
 \end{aligned}
 \tag{VII.37}$$

Results are posted in Table XII. In general, decreasing  $\Delta t$  does not change the

Table XII. Varying  $\Delta t$  in a 2-Layer Problem with a  $L_1$  Initiated Event

$\Delta t$	$ \eta _{max}$	$\frac{\ e\ _{max}}{ \eta _{max}}$
.1	$1.92 \times 10^{-6}$	4.13%
.05	$3.82 \times 10^{-6}$	3.18%
.01	$1.91 \times 10^{-5}$	3.25%
.005	$3.82 \times 10^{-5}$	3.23%
.002	$9.57 \times 10^{-5}$	3.23%

effectiveness of the Higdon NRBC. However it appears that  $|\eta|_{max}$  is inversely proportional to  $\Delta t$ . The probable reason for this behavior is that the introduction of

the event produces a discontinuity in  $\eta$  with regards to  $t$ . A smaller  $\Delta t$  results in a more pronounced discontinuity. It takes several numerical time-steps to sort out the discontinuity. The result is a  $|\eta|_{max}$  that is greater than the maximum amplitude of the event induced on  $\Omega$ .

## G. THE “HIGDON MATRIX”

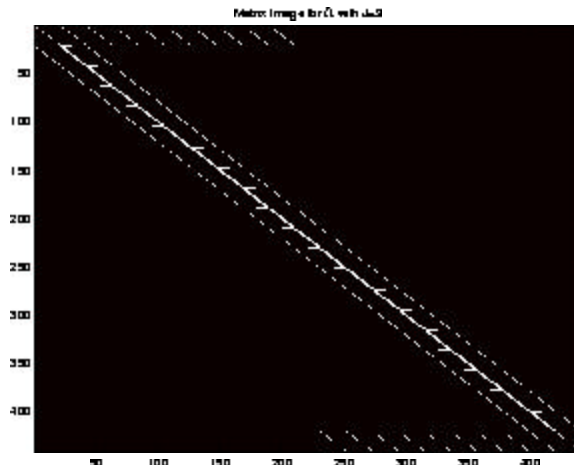


Figure 60. Higdon Matrix Image for  $\Omega$  ( $20 \times 20$ ) with Higdon NRBC's with Order  $J = 9$  Applied to Four Sides

As mentioned in Section VII.A, when non-zero advection terms are incorporated into the shallow water model the problem must be solved implicitly, and a  $N_x^2 \times N_y^2$  matrix with a bandwidth of  $2N_x$  is generated. An image of this matrix is presented in Figure 60 where zero elements are black and non-zero elements are white. Here the truncated domain  $\Omega$  is approximated using  $21 \times 21$  grid and Higdon NRBC's of order  $J = 9$  are applied to all four sides. On the top and the bottom of the image we see 10 light diagonal lines. These lines represent the discretization for the  $y$ -boundaries  $\Gamma_N$  (top) and  $\Gamma_S$  (bottom). The heavier line along the diagonal is three points thick and is flanked to the left and right by two thinner lines. These result from the discretization of the interior points. Finally, the periodic “short-spike” pointing to the left and right were generated by the Higdon NRBC's on  $\Gamma_E$  and  $\Gamma_W$ .

respectively. Note that there are only 19 each of these short horizontal lines. This indicates that the corner points were included in the  $y$ -boundaries, otherwise 21 ( $N_x$ ) of such pairs would be visible.

It is evident from the image, that the Higdon matrix required for non-zero advection problem is sparse. The number of non-zero points generated by the domain interior is:

$$5(N_x - 2)(N_y - 2), \quad (\text{VII.38})$$

and the number of non-zero points generated by the four Higdon NRBC's is:

$$(2N_x + 2N_y - 4)(J + 1). \quad (\text{VII.39})$$

Therefore the fraction of non-zero elements in the matrix is:

$$\frac{5(N_x - 2)(N_y - 2) + (2N_x + 2N_y - 4)(J + 1)}{N_x^2 N_y^2}. \quad (\text{VII.40})$$

In the case of our example where  $N_x = N_y = 21$  and  $J = 9$ , only 1.34% of the matrix is populated with non-zero values. In the  $N$ -layer model,  $N$  of such matrices might be produced severely taxing computer memory. Increasing domain size and a refining grid would further exacerbate the problem. Clearly sparse matrix procedures are in order and should be investigated to stream line the non-zero advection scheme and produce a faster algorithm.

## VIII. CONCLUSION AND RECOMMENDATIONS FOR FURTHER RESEARCH

From the preceding investigation we conclude that a very large domain with dispersive wave action governed by linear SWE's can be effectively restricted using Higdon NRBC's. This boundary condition will also work for versions of the linear SWE that include the effects of stratification and advection. However, as the SWE model becomes more complex, careful consideration must be given to values assigned to problem parameters to ensure the stability of the scheme.

There are many aspects of the problem addressed in this dissertation that should be investigated further. With regards to the SWE and the geophysical environment, further model development should include:

- Discretization of the non-linear SWE.
- Incorporation of a non-constant Coriolis parameter.
- Inclusion of a bottom topography that varies with  $x$  and  $y$ .
- Consideration of terms resulting from the Earth's curvature (i.e. domains with horizontal dimensions greater than 1000 km).

With regards to computational techniques, one should consider using sparse matrix algorithms for models requiring implicit solution techniques. Finally, with respect to the Higdon NRBC, the following areas of research are recommended:

- Development of schemes that use auxiliary variables to eliminate non-zero buffer zones. This is done outside this dissertation.
- Development of schemes to optimize selection of Higdon coefficients.
- Development of methods to update Higdon coefficients dynamically/adaptively.
- Extension of the rectangular domain to three dimensions.
- Development of Higdon NRBCs for cylindrical and spherical coordinates.

- Creation of two-way Higdon NRBC's to incorporate data from the immediate vicinity of the truncated domain.

These extensions to the current research are potentially of great value to oceanographers and meteorologists alike and may further promote the use of Higdon NRBC's in weather prediction models.

## LIST OF REFERENCES

- [1] D. Givoli, "Numerical Methods for Problems in Infinite Domains," Elsevier, Amsterdam, 1992.
- [2] S. V. Tsynkov, "Numerical Solution of Problems on Unbounded Domains, a Review," *Appl. Numer. Math.*, **27**, 465–532, 1998.
- [3] D. Givoli, "Exact Representation on Artificial Interfaces and Application in Mechanics," *App. Mech. Rev.*, **52**, 333–349, 1999.
- [4] T. Hagstrom, "Radiation Boundary Conditions for the Numerical Simulation of Waves," *Acta Numerica*, **8**, 47–106, 1999.
- [5] B. Engquist and A. Majda, "Radiation Boundary Conditions for Acoustic and Elastic Calculations," *Comm. Pure Appl. Math*, **32**, 313–357, 1979.
- [6] A. Bayliss and E. Turkel, "Radiation Boundary Conditions for Wave-Like Equations," *Comm. Pure Appl. Math*, **33**, 707–725, 1980.
- [7] J. B. Keller and D. Givoli, "Exact Non-Reflecting Boundary Conditions," *J. Comput. Phys.*, **82**, 261–279, 1989.
- [8] D. Givoli and J. B. Keller, "Non-Reflecting Boundary Condition for Elastic Waves," *Wave Motion*, **12**, 261–279, 1990.
- [9] J. P. Berenger, "A Perfectly Matched Layer for the Absorption of Electromagnetic Waves," *J. Comp. Phys.*, **114**, 185–200, 1994.
- [10] F. Collino, "High Order Absorbing Boundary Conditions for Wave Propagation Models. Straight Line Boundary and Corner Cases," *Proc. 2nd Int. Conf. on Mathematical & Numerical Aspects of Wave Propagation*, R. Kleinman et al., Eds., SIAM, Delaware, 161–171, (1993).
- [11] M. J. Grote and J. B. Keller, "Nonreflecting Boundary Conditions for Time Dependent Scattering," *J. Comput. Phys.*, **127**, 52–65, 1996.
- [12] M. J. Grote and J. B. Keller, "Exact Nonreflecting Boundary Conditions for Elastic Waves," *SIAM J. Appl. Math.*, **60**, 803–819, 2000.
- [13] I. L. Sofronov, "Conditions for Complete Transparency on the Sphere for the Three-Dimensional Wave Equation," *Russian Acad. Sci. Dokl. Math.*, **46**, 397–401, 1993.

- [14] T. Hagstrom and S. I. Hariharan, "A Formulation of Asymptotic and Exact Boundary Condition Using Local Operators," *Appl. Numer. Math.*, **27**, 403–416, 1998.
- [15] M. N. Guddati and J. L. Tassoulas, "Continued-Fraction Absorbing Boundary Conditions for the Wave Equation," *J. Comput. Phys.*, **8**, 139–156, 2000.
- [16] D. Givoli, "High-Order Non-Reflecting Boundary Condition Without High-Order Derivatives," *J. Comput. Phys.*, **170**, 849–870, 2001.
- [17] R. L. Higdon, "Absorbing Boundary Conditions for Difference Approximations to the Multi-Dimensional Wave Equation," *Math. Comput.*, **47**, 437–459, 1986.
- [18] R. L. Higdon, "Numerical Absorbing Boundary Conditions for the Wave Equation," *Math. Comput.*, **49**, 65–90, 1987.
- [19] R. L. Higdon, "Radiation Boundary Condition for Elastic Wave Propagation," *SIAM J. Numer. Anal.*, **27**, 831–870, 1990.
- [20] R. L. Higdon, "Absorbing Boundary Conditions for Elastic Waves," *Geophysics*, **56**, 231–241, 1991.
- [21] R. L. Higdon, "Radiation Boundary Conditions for Dispersive Waves," *SIAM J. Numer. Anal.*, **31**, 64–100, 1994.
- [22] D. Givoli and B. Neta, "High-Order Higdon Non-Reflecting Boundary Conditions for the Shallow Water Equations," *NPS-MA-02-001*, Technical Report, Naval Postgraduate School, Monterey, CA, 2002.
- [23] D. Givoli and B. Neta, "High-Order Non-Reflecting Boundary Conditions for Dispersive Waves," *Wave Motion*, **37**, 257–271, 2003.
- [24] D. Givoli and B. Neta, "High-Order Non-Reflecting Boundary Scheme for Time-Dependent Waves," *J. Comp. Phys.*, **186**, 24–46, 2003.
- [25] J. Pedlosky, *Geophysical Fluid Dynamics*, Springer, New York, 1987.
- [26] D. Givoli, B. Neta, and I. Patlasheko "Finite Element Solution of Exterior Time-Dependent Wave Problems with High-Order Boundary Treatment," *International Journal Numerical Methods in Engineering*, accepted for publication.
- [27] R.H. Sebersky, A.J. Acosta, and E.G. Hauptman, *Fluid Flow: A First Course in Fluid Mechanics*, Macmillan Publishing Co., Inc., New York, 1971.
- [28] B. Cushman-Roisin, *Introduction to Geophysical Fluid Dynamics*, Prentice Hall, Englewood Cliffs, New Jersey, 1994.



- [29] J. Proudman, *Dynamical Oceanography*, Methuen, London, and John Wiley, New York, 1953.
- [30] C. G. Rossby, "Relation Between Variations in the Intensity of the Zonal Circulation of the Atmosphere and the Displacements of the Semi-Permanent Centers of Action," *J. Marine Res.*, **2**, 38-55, 1939.
- [31] H. Stommel, "The Westward Intensification of Wind-Driven Ocean Currents," *Trans. Amer. Geoph. Union.*, **29**, 202-206, 1948.
- [32] B. P. Sommeijer, P. J. van der Houwen, and B. Neta, "Symmetric Linear Multistep Methods for Second Order Differential Equations with Periodic Solutions," *Applied Numerical Mathematics*, **2**, 69-77, 1986.
- [33] G. J. Haltiner and R. T. Williams, *Numerical Prediction and Dynamic Meteorology*, Second Edition, John Wiley & Sons, Inc., New York, 1980.
- [34] V. S. Ryaben'kii and S. V. Tsynkov, "Artificial Boundary Conditions for the Numerical Solution of External Viscous Flow Problems," *SIAM J. Numer. Anal.*, **32**, 1355-1389, 1995.
- [35] S. V. Tsynkov, E. Turkel, S. Abarbanel, "Extracting Flow Computation Using Global Boundary Conditions," *AIAA J.*, **34**, 700-706, 1996.

THIS PAGE INTENTIONALLY LEFT BLANK

## INITIAL DISTRIBUTION LIST

1. Defense Technical Information Center  
Fort Belvoir, Virginia

2. Dudley Knox Library  
Naval Postgraduate School  
Monterey, California

3. Beny Neta  
Naval Postgraduate School  
Monterey, California

4. Dan Givoli  
Technion  
Haifa, Israel

5. Arthur Schoenstadt  
Naval Postgraduate School  
Monterey, California

6. Robert Haney  
Naval Postgraduate School  
Monterey, California

7. Clyde Scandrett, Chairman  
Naval Postgraduate School  
Monterey, California

8. CDR Vincent van Joolen  
United States Naval Academy  
Annapolis, Maryland

9. Dr Mark Meyerson  
United States Naval Academy  
Annapolis, Maryland

10. CDR Raymond Putt  
United States Naval Academy  
Annapolis, MD
11. LTC Archie Wilmer  
United States Military Academy  
West Point, New York